Prepared for submission to JHEP

Are in-medium quark-gluon showers strongly coupled? Results in the large-$N_{\rm f}$ limit

Peter Arnold,[a] **Omar Elgedawy,**[b,c,a] **Shahin Iqbal**[d,e]

[a] *Department of Physics, University of Virginia, P.O. Box 400714, Charlottesville, VA 22904, U.S.A.*

[b] *Key Laboratory of Atomic and Subatomic Structure and Quantum Control (MOE), Guangdong Basic Research Center of Excellence for Structure and Fundamental Interactions of Matter, Institute of Quantum Matter, South China Normal University, Guangzhou 510006, China*

[c] *Guangdong-Hong Kong Joint Laboratory of Quantum Matter, Guangdong Provincial Key Laboratory of Nuclear Science, Southern Nuclear Science Computing Center, South China Normal University, Guangzhou 510006, China*

[d] *National Centre for Physics, Quaid-i-Azam University Campus, Islamabad, 45320 Pakistan*

[e] *Theoretical Physics Department, CERN, CH-1211 Geneva 23, Switzerland*

E-mail: parnold@virginia.edu, oae2ft@virginia.edu, smi6nd@virginia.edu

Abstract: Inside a medium, showers originating from a very high energy particle develop via medium-induced splitting processes such as bremsstrahlung and pair production. During shower development, two consecutive splittings sometimes overlap quantum mechanically, so that they cannot be treated independently. Some of these effects can be absorbed into an effective value of a medium parameter known as $\hat{q}$. Previous calculations (with certain simplifying assumptions) have found that, after adjusting the value of $\hat{q}$, the leftover effect of overlapping splittings is quite small for purely gluonic large-$N_{\rm c}$ showers but is very much larger for large-$N_{\rm f}$ QED showers, at comparable values of $N\alpha$. Here, by investigating the same problem for QCD *with quarks* in the large-$N_{\rm f}$ limit of many quark flavors, we make a first study of whether the small effect in purely gluonic showers (i) was merely an accident or (ii) is more broadly characteristic of such overlap effects in QCD. We also offer a qualitative explanation for the large size of the effect in QED vs. QCD.

Contents

1 Introduction and Preview of Results

1.1 Introduction

When passing through matter, high energy particles lose energy by showering, via the splitting processes of hard bremsstrahlung and pair production. At very high energy, the quantum mechanical duration of each splitting process, known as the formation time, exceeds the mean free time for collisions with the medium, leading to a significant reduction in the splitting rate known as the Landau-Pomeranchuk-Migdal (LPM) effect. The LPM effect was originally worked out for QED in the 1950's [1–3][1] and then later generalized to QCD in the 1990s by Baier, Dokshitzer, Mueller, Peigne, and Schiff [5–7] and by Zakharov [8, 9] (BDMPS-Z).

Modeling of the development of high-energy in-medium showers typically treats each splitting as an independent dice roll, with probabilities set by calculations of single-splitting rates that take into account the LPM effect. The question then arises whether consecutive splittings in a shower can really be treated as probabilistically independent, or whether there is any significant chance that the formation times of splittings could overlap so that there are significant quantum interference effects entangling one splitting with the next. A number of years ago, several authors showed [10–12], in a leading-log calculation, that the effects of overlapping formation times in QCD showers could become large when one of the two overlapping splittings is parametrically softer than the other. They also showed that those large leading logarithms could be absorbed into a redefinition of the medium parameter $\hat{q}$, which parametrizes the effectiveness with which the medium deflects high-energy particles. A refined question arose: How large are overlapping formation time effects that *cannot* be absorbed into a redefinition of $\hat{q}$?

We previously investigated this question in refs. [13, 14] using the following thought experiment. We focused on purely gluonic showers (i.e. pure Yang-Mills theory) in the large-N_c limit. Consider such a shower initiated by a high-energy gluon moving in the z direction, starting at z=0. Imagine for simplicity that the medium is static, homogeneous, and arbitrarily large. Let $\epsilon(z)$ be the distribution in z of the energy that the shower deposits in the medium, statistically averaged over many such showers. Define the energy stopping length $\ell_{\rm stop}$ to be the first moment of that distribution, $\ell_{\rm stop} \equiv \langle z \rangle_\epsilon \equiv E_0^{-1} \int dz\, z\, \epsilon(z)$, where E_0 is the energy of the initial gluon. Let σ be the width of the distribution $\epsilon(z)$. Ignoring overlap effects, both $\ell_{\rm stop}$ and σ scale with $\hat{q}$, coupling constant, and the energy E_0 of the initial electron as

$$\sigma \sim \ell_{\rm stop} \sim \frac{1}{\alpha_s} \sqrt{\frac{E_0}{\hat{q}}}. \tag{1.1}$$

Naively, the value of $\hat{q}$ then cancels in the ratio $\sigma/\ell_{\rm stop}$. Any effect that can be absorbed into $\hat{q}$ would not affect the value of $\sigma/\ell_{\rm stop}$, and so that ratio could be used to test how large are overlapping formation time effects that cannot be absorbed into $\hat{q}$. (Refs. [13, 14] explain

[1] The papers of Landau and Pomeranchuk [1, 2] are also available in English translation [4].

how the situation is a little more subtle than that, but we will be able to mostly ignore those subtleties in this paper.)

To leading order in α_s, refs. [13, 14] found that the *relative* size of overlap effects were extremely small, of order $O(1\%) \times N_c \alpha_s$. That was a surprising result because earlier work [15] had made a similar calculation for large-N_f QED and found that the corresponding overlap effects were of order $O(100\%) \times N_f \alpha$. (We'll present more precise numbers shortly.)

Those results raise the question of *why* the QED and QCD results are so very different for comparable values of $N\alpha$! One possibility is that the small QCD result might merely arise from an accidental cancellation peculiar to the special case of purely gluonic large-N_c showers. In this paper, we check the robustness of the small QCD result by adding quarks to our QCD showers. For a first look, we can tremendously simplify the calculation by adding many flavors of quark. We will take the large-N_f limit (where N_f is the number of quark flavors) in addition to the large-N_c limit. Specially, we study the case $N_f \gg N_c \gg 1$. The advantage of this limit is that we will be able to adapt existing formulas for large-N_f QED overlap rates [16], and their effect on QED showers [15, 17], to large-N_f QCD.

We will also present a qualitative explanation of why the size of overlap effects is so different for QCD vs. QED at comparable values of $N\alpha$. Ultimately, the reason traces back to the fact that colored high-energy gluons interact much more directly with a QCD medium than high-energy neutral photons interact with a QED medium, and that consequently pair production ($\gamma \to e\bar{e}$) can have a large qualitative effect in a QED shower when it overlaps with the earlier LPM-suppressed splitting ($e \to e\gamma$) that created the photon in the first place.

1.2 Preview of Results

Table 1 previews results for the overlap correction to $\sigma/\ell_{\text{stop}}$ in various situations, contrasting large-N QCD results with large-N QED results. The first two lines show results for the corrections to $\sigma/\ell_{\text{stop}}$ for the energy deposition distribution $\epsilon(z)$ for showers initiated by either a gauge boson (gluon vs. photon) or fermion (quark vs. electron).

The third row of the table shows similar results for the deposition of the flavor of the initial fermion in a fermion-initiated shower. For both large-N_f QCD and large-N_f QED, one may follow the progress of the initial fermion through a fermion-initiated shower, and the "initial flavor" distribution is the distribution of where the initial fermion stops and thermalizes with the medium.[2] For large-N_f QED, the distribution of initial-flavor deposition is the same as the distribution of charge deposition, for slightly non-trivial reasons that we review later. For large-N_f QCD, it is not.

The comparisons in table 1 (ignoring the very last line of the table) make clear that the earlier small result for $\hat{q}$-insensitive overlap effects of a purely gluonic shower is not a peculiar accident of purely gluonic showers. Adding many flavors of quarks does not qualitatively

[2] Without a large-N_f approximation (more specifically $N_f \gg N_c$ in the case of QCD), identifying which fermion is the heir to the original parent fermion becomes ambiguous due to interferences in overlapping splittings. See the discussion of figs. 11a and b in ref. [15]. Be warned that the brief discussion of "large-N_c" QCD in ref. [15] implicitly assumes that $N_f \ll N_c$ and does not address the case $N_f \gtrsim N_c \gg 1$.

deposition distribution	initiating particle	overlap correction to $\sigma/\ell_{\rm stop}$		
		$N_{\rm f}$=0, large-$N_{\rm c}$ QCD	$N_{\rm f} \gg N_{\rm c} \gg 1$ QCD	large-$N_{\rm f}$ QED
energy	g/γ	$1.0\% \times N_{\rm c}\alpha_{\rm s}$	$-0.4\% \times N_{\rm f}\alpha_{\rm s}$	$99\% \times N_{\rm f}\alpha$
energy	q/e		$-0.5\% \times N_{\rm f}\alpha_{\rm s}$	$113\% \times N_{\rm f}\alpha$
initial flavor	q/e		$1.1\% \times N_{\rm f}\alpha_{\rm s}$	$-85\% \times N_{\rm f}\alpha$
fermion number	q/e		IR-unsafe	$-85\% \times N_{\rm f}\alpha$

Table 1. The relative size of overlap corrections to the ratio $\sigma/\ell_{\rm stop}$ of width to stopping distance. Different columns compare (i) purely gluonic ($N_{\rm f}$=0) large-$N_{\rm c}$ QCD showers [13, 14] to (ii) large-$N_{\rm f}$ ($N_{\rm f}\gg N_{\rm c}\gg 1$) QCD showers (this paper) to (iii) large-$N_{\rm f}$ QED showers [17]. Different rows show results for the deposition distributions of different types of conserved quantities and for showers initiated by different types of particles (gauge bosons vs. fermions). Results in this table are given for the renormalization scale choice $\mu \propto (\hat{q}E)^{1/4}$. The purely gluonic ($N_{\rm f}$=0) result also requires a choice of infrared factorization energy scale $\Lambda_{\rm fac}$, which here is $\Lambda_{\rm fac} = E/4$. (The scale choices in that case are slightly different from what refs. [13, 14] highlighted as their "preferred" choices. The result quoted here instead matches that for σ_S in table 4 of ref. [14])

change the small size of the QCD overlap effects, at least not in the large-$N_{\rm f}$ limit we have studied. Later in this paper, we will check that overlap corrections to $\hat{q}$-insensitive ratios involving higher moments of the deposition are also small.

The last row of table 1 is presented as a warning that not every deposition distribution of a conserved quantity is infrared (IR) safe. Infrared behavior becomes an issue for the deposition of fermion number (or electric charge) from a quark-initiated shower. As discussed later, this distribution is affected by very low energy quark-antiquark pairs produced and asymmetrically deposited very early in the evolution of the shower.

For the purpose of this introduction, we have not displayed more precision for the entries in table 1 because the exact values are sensitive to choices one makes for the renormalization scale and, in the gluonic case ($N_{\rm f}$=0), also to an infrared factorization scale that must be introduced [13, 14]. The dependence of our results on these scale choices is small and does not affect the qualitative conclusion that overlap corrections which cannot be absorbed into $\hat{q}$ are very small in QCD, at least for the QCD limits and various infrared-safe quantities that we have examined.

Though our numerical results indicate that the tiny sizes of $\hat{q}$-insensitive overlap effects for QCD were not merely an accidental cancellation peculiar to the case of purely gluonic ($N_{\rm f}$=0) showers, the numbers by themselves do not explain *why* the effect is much larger in QED than QCD for comparable values of $N\alpha$. Our later qualitative explanation will lead to a physically-motivated analytic approximation for the QED result that explains most of the difference. The steps of that explanation will rely on rough, qualitative arguments whose credibility will be enhanced by their agreement with features of our numerical calculations. For that reason, we have chosen to organize this paper to first present all the details behind our full, quantitative

calculations, and we will wait until the very end to present our qualitative explanation of the difference between QED and QCD. But readers interested mainly in qualitative takeaways may wish to skip directly to section 8.

1.3 Outline

In the next section, we first lay out our assumptions and approximations. We then review the relevant BDMPS-Z in-medium splitting rates for independent splittings and then discuss the rates needed to account for overlapping formation time effects to first order in $N_{\rm f}\alpha_{\rm s}$. In section 3, we explain how to get formulas for those overlap effect rates in $N_{\rm f}\gg N_{\rm c}\gg 1$ QCD by adapting previous calculations of such rates in large-$N_{\rm f}$ QED. (The final QCD formulas are summarized in appendix A.) Following earlier works, section 4 selectively integrates and repackages all of the relevant rates into net rates for a splitting or pair of overlapping splittings to produce one daughter of energy xE from a parent of energy E. Numerical results are given for those net rates $[d\Gamma/dx]^{\rm net}$, which are then fit to relatively simple analytic forms for subsequent use in calculations of in-medium shower development. Section 5 reviews the formalism for calculating the overlap corrections to $\sigma/\ell_{\rm stop}$ presented in table 1. The formalism also provides results for similar ratios involving higher moments of energy or initial-flavor deposition distributions. Section 6 explains why table 1 lists the size of overlap corrections to $\sigma/\ell_{\rm stop}$ as "IR-unsafe" for the case of large-$N_{\rm f}$ QCD fermion number deposition.

Table 1 shows that the size of overlap effects that cannot be absorbed into $\hat{q}$ are very small for QCD and so can be safely ignored. But that will not be so useful if the amount that must be absorbed varies between different types of measurement. Section 7 offers a modest first test of whether the size of "corrections that must be absorbed into $\hat{q}$" are the same for different types of measurements.[3]

As mentioned previously, section 8 offers a qualitative explanation of why the size of overlap effects presented in table 1 are so much larger for QED than for QCD for comparable values of $N\alpha$. Section 9 offers a brief conclusion.

2 Building blocks: splitting rates

In the large-$N_{\rm f}$ limit (specifically $N_{\rm f}\gg N_{\rm c}$), QCD showers are made up of $q\to qg$ and $g\to q\bar{q}$ splitting processes, as depicted in fig. 1. The effect of purely-gluonic splitting $g\to gg$ is suppressed. In this limit, the types of relevant splitting processes are similar to those for QED showers ($e\to e\gamma$ and $\gamma\to e\bar{e}$), which will allow us to adapt previous large-$N_{\rm f}$ QED calculations of overlapping splitting rates [16].

[3] The universality of *soft* radiative corrections to $\hat{q}$ has already been established at leading-log order (LLO) by refs. [10–12, 18] and, for large $N_{\rm c}$, at NLLO by ref. [19]. However, ratios like $\sigma/\ell_{\rm stop}$ also ignore significant *hard* corrections that affect the numerator and denominator the same way, and it is also only in taking the ratio that one reduces extreme sensitivity to the choice of factorization scale for absorbing the soft radiative corrections into $\hat{q}$ [14]. We do not know *a priori* if these canceling hard corrections can be absorbed into $\hat{q}$ in a process-independent way, which is why we need to check.

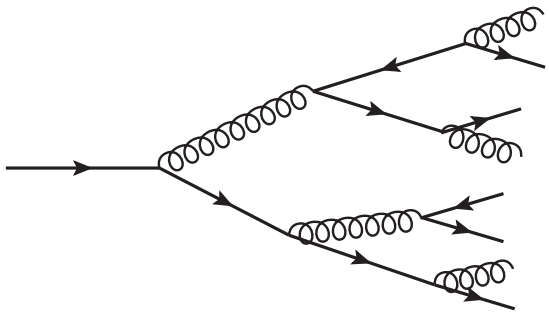

Figure 1. Depiction of an (in-medium) high-energy shower in large-N_f QCD. The interactions with the QCD medium are not explicitly shown. The transverse spread of the shower will be very small but has been exaggerated here for the sake of the drawing.

2.1 Assumptions

In this paper, we make the same simplifying assumptions previously made for similar analysis of purely gluonic (N_f=0) showers in refs. [13, 14] and for large-N_f QED showers in refs. [15, 17]. In brief summary, we assume a static, homogeneous medium that is large enough to contain (i) formation times in the case of splitting rate calculations and (ii) the entire development of the shower for calculation of overlap effects on shower characteristics like $\sigma/\ell_{\rm stop}$. We ignore vacuum and medium-induced masses of all high-energy particles. We take the multiple-scattering ($\hat{q}$) approximation for transverse momentum transfers from the medium. We approximate the bare value $\hat{q}_{(0)}$ of $\hat{q}$ as constant.[4] We assume that the particle initiating the shower can be approximated as on-shell. In the case of QCD, we take the large-N_c approximation $N_c \gg 1$ because it simplifies color dynamics during overlapping formation times [20]. We only calculate $p_\perp$-integrated rates[5] and so only look at $p_\perp$-insensitive observables for our thought experiments, such as the deposition distributions $\rho(z)$ and $\epsilon(z)$, for which we do not keep track of the (parametrically small) spread of the deposition in directions transverse to z.

2.2 Leading-order rates and notation for group factors

We refer to single-splitting rates that *ignore* the possibility of overlapping splittings as *leading-order* (LO) rates, which are the rates originally investigated by LPM and BDMPS-Z. For us, leading order means leading order in the number of high-energy splitting vertices and includes the effects of an arbitrary number of interactions with the medium. Adopting Zakharov's picture [8, 9], we think of rates like $q\to qg$ and $g\to q\bar{q}$ as time-ordered interference diagrams, such as fig. 2, which combine the amplitude for splitting (blue) with the conjugate amplitude

[4] In this context, the "bare" $\hat{q}_{(0)}$ represents the contribution from scattering of the high-energy particle with the medium *without* any high-energy splitting.

[5] Especially for overlapping formation times, rates that are integrated over final $p_\perp$'s are enormously simpler to calculate than rates that are not. See the discussion in section 4.4 of ref. [20] and appendix F of ref. [21].

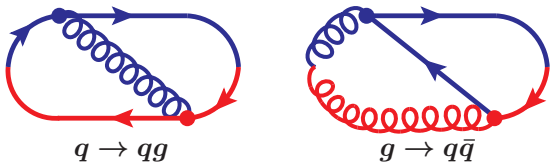

Figure 2. Time-ordered interference diagrams contributing to the rates of $q \to qg$ and $g \to q\bar{q}$. Time runs from left to right. In both cases, all lines implicitly interact with the medium. Only one of the two time orderings that contribute to each process are shown above, but both orderings can be included by taking $2\,\mathrm{Re}[\cdots]$.

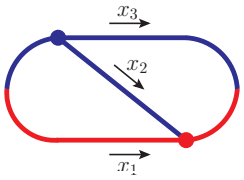

Figure 3. A generic abstraction of LO splitting diagrams such as fig. 2, here showing our labeling of the longitudinal momentum fractions x_i of the high-energy particles in the amplitude and conjugate amplitude. Following the conventions of ref. [20], we take the x's in the conjugate amplitude to be negative (in the forward time direction shown in the diagram), so that longitudinal momentum is conserved at the vertices of this interference diagram.

(red). See refs. [20, 22] for more discussion of our graphical conventions and implementation of Zakharov's approach.

In order to prepare for later discussion, and for comparisons of QCD vs. QED, we briefly consider a more general (but still high-energy) situation. Generically represent each diagram of fig. 2 by fig. 3. In Zakharov's approach, the evolution of the high-energy particles between the two vertices in fig. 2 is simplified to a problem in 3-particle two-dimensional quantum mechanics in the transverse plane, where the three particles consist of (i) the two (blue) particles in the amplitude plus (ii) the single (red) particle in the conjugate amplitude, with a corresponding 3-particle Hamiltonian

$$\frac{\boldsymbol{p}_{1\perp}^2}{2x_1E} + \frac{\boldsymbol{p}_{2\perp}^2}{2x_2E} + \frac{\boldsymbol{p}_{3\perp}^2}{2x_3E} + V_3(\boldsymbol{b}_1, \boldsymbol{b}_2, \boldsymbol{b}_3), \tag{2.1}$$

where the kinetic terms originate from the high-energy expansion $E_p = \sqrt{p_z^2 + \boldsymbol{p}_\perp^2} \simeq p_z + \boldsymbol{p}_\perp^2/(2p_z)$ for each particle. In (2.1), E is the energy of the parent, and (x_1, x_2, x_3) are the momentum fractions of the three particles as oriented in the direction shown in the diagram of fig. 3. For the diagram of fig. 2, for example, they would be $(x_1, x_2, x_3) = (-1, x_g, 1-x_g)$, where x_g is momentum fraction of the gluon.[6] The 3-particle "potential energy" V_3 in (2.1)

[6]The negative sign for x_1 and so the negative value of the first term in (2.1) arises because particle "1" here

represents the effect of correlations arising from medium averaging the effects of the high-energy particles' interactions with the medium. In the $\hat{q}$ approximation, it is given by[7]

$$V_3(\boldsymbol{b}_1,\boldsymbol{b}_2,\boldsymbol{b}_3) = -\frac{i}{8}\Big[(\hat{q}_1+\hat{q}_2-\hat{q}_3)(\boldsymbol{b}_2-\boldsymbol{b}_1)^2 + (\hat{q}_2+\hat{q}_3-\hat{q}_1)(\boldsymbol{b}_3-\boldsymbol{b}_2)^2 + (\hat{q}_3+\hat{q}_1-\hat{q}_2)(\boldsymbol{b}_1-\boldsymbol{b}_3)^2\Big] \quad (2.2)$$

in terms of the transverse positions $(\boldsymbol{b}_1,\boldsymbol{b}_2,\boldsymbol{b}_3)$ of the three particles. Here, $\hat{q}_i$ is the value of $\hat{q}$ associated with the type of particle i. Three-dimensional rotation invariance may be used to reduce the two-dimensional 3-particle problem described by (2.1) to an effective 1-particle problem in terms of a single transverse position variable[8]

$$\boldsymbol{B} \equiv \frac{\boldsymbol{b}_1-\boldsymbol{b}_2}{x_1+x_2} = \frac{\boldsymbol{b}_2-\boldsymbol{b}_3}{x_2+x_3} = \frac{\boldsymbol{b}_3-\boldsymbol{b}_1}{x_3+x_1}\,. \quad (2.3)$$

In the $\hat{q}$ approximation of (2.2), the effective 1-particle system is described by the Hamiltonian[9]

$$\mathcal{H} = \frac{\boldsymbol{P}_\perp^2}{2M} + \tfrac{1}{2}M\,\Omega_0^2\,\boldsymbol{B}^2 \quad (2.4a)$$

with

$$M \equiv -x_1x_2x_3E, \qquad \Omega_0^2 \equiv -\frac{i}{2E}\left(\frac{\hat{q}_1}{x_1}+\frac{\hat{q}_2}{x_2}+\frac{\hat{q}_3}{x_3}\right). \quad (2.4b)$$

Generically, the corresponding LPM/BDMPS-Z single splitting rate (in $\hat{q}$ approximation) turns out to be

$$\left[\frac{d\Gamma}{dx}\right]^{\rm LO} = \frac{\alpha}{\pi}\,P_{\rm DGLAP}(x)\;{\rm Re}(i\Omega_0), \quad (2.5)$$

where $P_{\rm DGLAP}$ is the corresponding unregulated Dokshitzer-Gribov-Lipatov-Alterelli-Parisi (DGLAP) vacuum splitting function.

represents the initial quark in the *conjugate* amplitude.

[7] For a general argument for the form (2.2), see for example the argument in appendix A of ref. [20] for eq. (2.21), or the review of earlier arguments in section III.A of ref. [23]. Note that V_3 does not physically represent a potential energy; it merely plays that mathematical role in the Hamiltonian (2.1). In particular, the V_3 of (2.2) is imaginary-valued. The effective Hamiltonian (2.1) need not be Hermitian because a medium-average of unitary time evolution is not itself unitary.

[8] An equivalent reduction was used by Zakharov [8, 9]. For a discussion in the language used here, see section 3 of ref. [20]. The equalities in (2.3) depend on the fact that $x_1+x_2+x_3 = 0$ and the constraint $x_1\boldsymbol{b}_1 + x_2\boldsymbol{b}_2 + x_3\boldsymbol{b}_3 = 0$. See, for example, section 3.1 of ref. [20] for one way of understanding the last constraint.

[9] See specifically eqs. (2.27) and (2.33) of ref. [20].

For the splitting processes $q \to qg$ and $g \to q\bar{q}$, (2.4b) and (2.5) give[10]

$$\left[\frac{d\Gamma}{dx_q}\right]^{\rm LO}_{q\to qg} = \frac{\alpha_{\rm s}}{2\pi} P_{q\to q}(x_q) \sqrt{\frac{1}{E}\left|\frac{\hat{q}_{\rm F}}{x_q} + \frac{\hat{q}_{\rm A}}{1-x_q} - \hat{q}_{\rm F}\right|}, \tag{2.6a}$$

$$\left[\frac{d\Gamma}{dx_q}\right]^{\rm LO}_{g\to q\bar{q}} = \frac{N_{\rm f}\alpha_{\rm s}}{2\pi} P_{g\to q}(x_q) \sqrt{\frac{1}{E}\left|\frac{\hat{q}_{\rm F}}{x_q} + \frac{\hat{q}_{\rm F}}{1-x_q} - \hat{q}_{\rm A}\right|}, \tag{2.6b}$$

where $\hat{q}_{\rm F}$ and $\hat{q}_{\rm A}$ are respectively the values of $\hat{q}$ for quarks (fundamental color representation) and gluons (adjoint color representation), and

$$P_{q\to q}(x) = C_{\rm F}\frac{1+x^2}{1-x}, \qquad P_{g\to q}(x) = t_{\rm F}[x^2 + (1-x)^2]. \tag{2.7}$$

C_R and t_R are the quadratic Casimir and trace normalization defined in terms of the color generators T^a_R of representations R by

$$T^a_R T^a_R = C_R \mathbb{1}, \qquad {\rm tr}(T^a_R T^b_R) = t_R \delta^{ab}. \tag{2.8}$$

In the large-$N_{\rm c}$ limit, which we take to simplify the calculation of overlap effects, $\hat{q}_{\rm A} = 2\hat{q}_{\rm F}$, which is an example of Casimir scaling of $\hat{q}$ since $C_{\rm A} = 2C_{\rm F}$ in that same limit. At the moment, however, we are only discussing leading-order splitting rates (no overlaps yet), and so we may be a little more general but will still assume Casimir scaling of $\hat{q}$. (Casimir scaling is automatic in the limit of weakly-coupled quark gluon plasmas. Beyond weak coupling, ref. [25] suggests that Casimir scaling is, more generally, a necessary consistency condition for any $\hat{q}$ approximation, but there are caveats.[11]) With Casimir scaling, (2.6) may be written solely in terms of $\hat{q}_{\rm F}$ as

$$\left[\frac{d\Gamma}{dx_q}\right]^{\rm LO}_{q\to qg} = \frac{\alpha_{\rm s}}{2\pi} P_{q\to q}(x_q) \sqrt{\frac{\hat{q}_{\rm F}}{E}\left|\frac{1}{x_q} + \frac{C_{\rm A}}{C_{\rm F}(1-x_q)} - 1\right|}, \tag{2.9a}$$

$$\left[\frac{d\Gamma}{dx_q}\right]^{\rm LO}_{g\to q\bar{q}} = \frac{N_{\rm f}\alpha_{\rm s}}{2\pi} P_{g\to q}(x_q) \sqrt{\frac{\hat{q}_{\rm F}}{E}\left|\frac{1}{x_q} + \frac{1}{1-x_q} - \frac{C_{\rm A}}{C_{\rm F}}\right|}. \tag{2.9b}$$

[10] The absolute values signs in (2.6) are unnecessary for $0 < x_q < 1$. They have been included here for an obscure reason, which is to avoid any possible confusion about the applicability of formulas if considering the front-end transformations used to relate some diagrams for overlapping splitting effects, as described in refs. [16] and [24]. Those transformations can replace x_q by a negative value.

[11] See in particular section 3.3 of ref. [25]. The argument there was specific to the SU(N) generalizations of SU(3) color representations $R = \mathbf{8}$, $\mathbf{10}$, and $\mathbf{27}$. We presume that similar arguments could be constructed for other color representations, but (as far as we know) this has not yet been done. Ref. [25] implicitly assumed that the $\hat{q}_i$ were constant, and so the argument is restricted to what in this paper we have called our bare $\hat{q}_{(0)}$ (which we have taken to be constant). Additionally, the argument assumed that there is no difference between the values of $\hat{q}$ for (i) an amplitude (blue) line correlated with a conjugate amplitude (red) line and (ii) an amplitude (blue) line correlated with another amplitude (blue) line. Once one includes radiative corrections, it is known [19] that these are no longer exactly equivalent.

There is a factor of N_f in the pair production rate (2.9b) because the produced pair can have any flavor.

For QCD, the group constants are

$$C_A = N_c, \qquad C_F = \tfrac{N_c^2-1}{2N_c}, \qquad t_F = \tfrac{1}{2} \qquad \text{(QCD)}, \tag{2.10}$$

but, for the results obtained in this paper, we use the large-N_c limit

$$C_A = N_c, \qquad C_F = \tfrac{N_c}{2}, \qquad t_F = \tfrac{1}{2} \qquad (N_c \gg 1 \text{ QCD}), \tag{2.11}$$

and so $C_A/C_F = 2$ in (2.9). One may also recover the leading-order rates for QED by using

$$C_A = 0, \qquad C_F = 1, \qquad t_F = 1 \qquad \text{(QED)} \tag{2.12}$$

and replacing α_s by α, but the difference between large-N_f QCD and QED formulas for *overlap* calculations will be slightly more involved (see section 3).

2.3 NLO Diagrams

For $N_f \gg N_c \gg 1$ QCD, the relevant diagrams and many details of the calculation of overlap effects will closely parallel the discussion of large-N_f QED in refs. [15–17]. For a start, fig. 4 depicts a section of a shower and the parametric size of typical distance scales for the case of democratic splittings. Democratic means that neither daughter of a splitting is soft compared to its parent. (We'll later have reason in section 8 to instead discuss the case where one of the gluons is soft.) For democratic splittings, formation times are of order[12]

$$t_{\text{form}} \sim \sqrt{\frac{E}{\hat{q}}} \qquad \text{(democratic splittings)} \tag{2.13}$$

and are all of the same order for the first few (the most important) splittings in the shower. When the LPM effect is relevant (high energies and so formation times large compared to mean-free times), the probability of democratic bremsstrahlung $q \to qg$ is parametrically of order $C_F\alpha_s$ per formation time, and so the typical distance between successive bremsstrahlungs is of order the formation time divided by $C_F\alpha_s$, as depicted in the figure (except that there we've used the fact that $C_F \sim N_c$). In contrast, pair production (2.9b) is enhanced by a factor of N_f and so is much more rapid than bremsstrahlung in the large-N_f limit. In detail, the probability of pair production is of order $N_f t_F \alpha_s \sim N_f \alpha_s$ per formation time. In this paper, we take the large-N_f limit of QCD to mean

$$N_f \gg N_c \gg 1. \tag{2.14}$$

We then have a parametric hierarchy of scales in fig. 4, and the possibility of (i) two bremsstrahlungs overlapping each other is suppressed (by a factor of $N_c/N_f \ll 1$) compared to

[12] In terms of formulas, the parametric scale of the formation time is the scale of $1/|\Omega_0|$ from (2.4b), here specialized to democratic splittings.

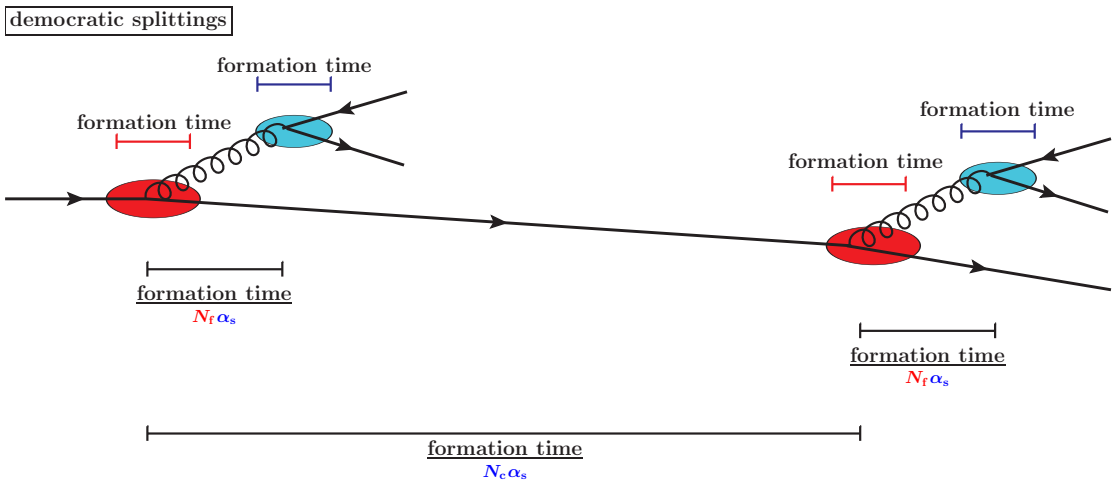

Figure 4. Parametric summary of the relative size of typical formation lengths and distances between *democratic* splitting for large-N_f QCD when $N_c\alpha_s \ll N_f\alpha_s \ll 1$. Large-$N_f$ QED looks the same [16] for democratic splittings, with α_s replaced by α, and N_c replaced by 1.

the possibility that (ii) a bremsstrahlung overlaps a following pair production. In computing overlap effects, we therefore only need to compute the latter case in the limit (2.14) [at least as far as real (i.e. non-virtual) double splitting is concerned].

We also assume that

$$N_f\alpha_s(\mu) \ll 1, \tag{2.15}$$

where $\alpha_s(\mu)$ is the value of α_s appropriate to high-energy splitting vertices, meaning that the renormalization scale μ has been chosen to be of order the typical transverse momenta of the daughters of typical splittings, which is $\mu \sim (\hat{q}E)^{1/4}$ for democratic splittings.[13] There is then a double hierarchy of scales

$$\text{formation time} \ll \frac{\text{formation time}}{N_f\alpha_s} \ll \frac{\text{formation time}}{N_c\alpha_s} \tag{2.16}$$

in fig. 4.

With that preparation, fig. 5 shows some examples of interference diagrams contributing to overlapping $q \to qg \to qq\bar{q}$. We refer to overlap corrections as next-to-leading-order (NLO) effects because these diagrams are suppressed by $O\big(N_f\alpha_s(\mu)\big)$ compared to leading-order ones. At the same order, there are also virtual corrections to single splitting, some examples of which are shown in fig. 6. The full set of NLO diagrams for large-N_f QED may be found in ref. [16] (also reproduced in our fig. 18 here in appendix A). Replacing photon lines with gluon lines gives the full set for $N_f \gg N_c \gg 1$ QCD.

[13] See, for instance, the discussion in refs. [13, 14].

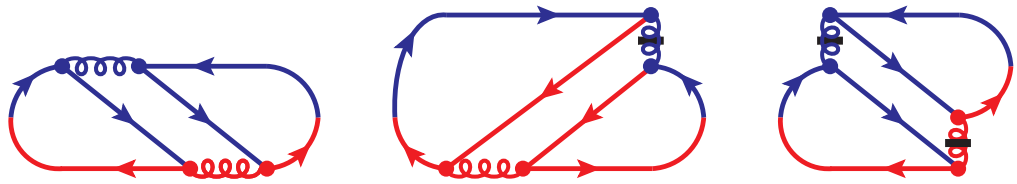

Figure 5. A few examples of lightcone-time ordered interference diagrams for $q \to qq\bar{q}$ in $N_f \gg N_c \gg 1$ QCD. Here, the gluons are transverse polarized unless they are crossed by a black bar. The bar-crossed gluon lines indicate the exchange of a longitudinally-polarized gluon in light-cone gauge, which is instantaneous in lightcone time.

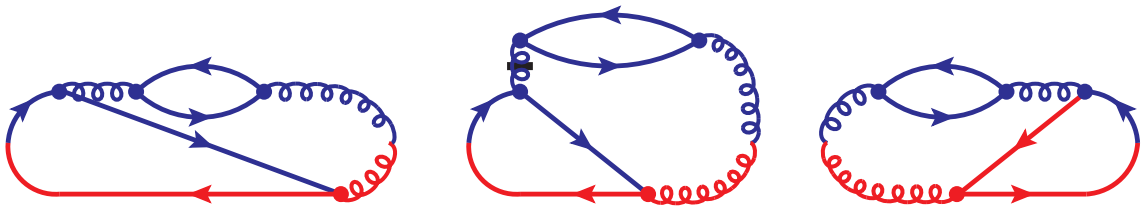

Figure 6. A few examples of lightcone-time-ordered interference diagrams for the virtual correction to single splitting $q \to qg$ or $g \to q\bar{q}$ in $N_f \gg N_c \gg 1$ QCD.

2.4 Notation for Rates

The original motivation of taking the large-N_f limit was simply to reduce the number of interference diagrams that had to be calculated. However, following ref. [17], the large-N_f limit also somewhat simplifies the analysis of shower development by distinguishing all the daughters of bremsstrahlung overlapping with pair production, labeled as in fig. 7. The two daughter quarks are distinguishable particles in the large-N_f limit because the probability that the flavor of the pair-produced quark is the same as that of the initial quark scales like $1/N_f$. When convenient, we will emphasize this distinguishability by using the symbol Q for pair-produced quarks and so refer to overlapping bremsstrahlung followed by pair production as

$$q \to qg \to q\mathrm{Q}\bar{\mathrm{Q}}. \tag{2.17}$$

We will also often refer to leading-order pair production as $g \to \mathrm{Q}\bar{\mathrm{Q}}$ and the corresponding one-loop virtual correction (such as the last diagram of fig. 6) as the interference of

$$g \to \mathrm{Q}'\bar{\mathrm{Q}}' \to g \to \mathrm{Q}\bar{\mathrm{Q}} \tag{2.18}$$

with leading-order $g \to \mathrm{Q}\bar{\mathrm{Q}}$.

With this notation, the initial building blocks that we need (closely following the treatment

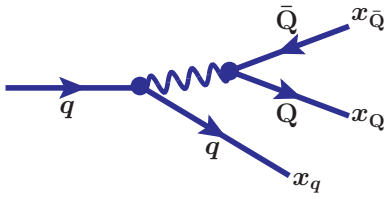

Figure 7. Our notation (2.17) for distinguishing pair-produced quarks from the original quark in $q \to qg \to qq\bar{q}$ in the large-$N_{\rm f}$ limit. The x's are the energy fractions of the original electron, and $x_{\bar{\mathrm{Q}}} = 1 - x_q - x_{\mathrm{Q}}$.

[17] of large-$N_{\rm f}$ QED) will be referred to as

$$\text{1}\to\text{2 rates:} \qquad \left[\frac{d\Gamma}{dx_q}\right]_{q\to qg} = \left[\frac{d\Gamma}{dx_q}\right]^{\rm LO}_{q\to qg} + \left[\Delta\frac{d\Gamma}{dx_q}\right]^{\rm NLO}_{q\to qg}, \tag{2.19a}$$

$$\left[\frac{d\Gamma}{dx_{\mathrm{Q}}}\right]_{g\to \mathrm{Q}\bar{\mathrm{Q}}} = \left[\frac{d\Gamma}{dx_{\mathrm{Q}}}\right]^{\rm LO}_{g\to \mathrm{Q}\bar{\mathrm{Q}}} + \left[\Delta\frac{d\Gamma}{dx_{\mathrm{Q}}}\right]^{\rm NLO}_{g\to \mathrm{Q}\bar{\mathrm{Q}}}, \tag{2.19b}$$

$$\text{effective 1}\to\text{3 rate:} \qquad \left[\Delta\frac{d\Gamma}{dx_q\,dx_{\mathrm{Q}}}\right]_{q\to q\mathrm{Q}\bar{\mathrm{Q}}}. \tag{2.19c}$$

The 1→3 rate (2.19c) represents the overlap *correction* to treating real double splitting (2.17) as two, consecutive, independent LO splittings.[14] The NLO pieces of (2.19a) and (2.19b) represent virtual corrections to the leading-order rates. In terms of the above building blocks, overlap effects of two consecutive splittings can be accounted for by *classical* probability analysis of a shower developing via 1→2 and 1→3 splittings described by (2.19).

3 Converting large-$N_{\rm f}$ QED rates to $N_{\rm f}\gg N_{\rm c}\gg 1$ QCD rates

We now discuss how large-$N_{\rm f}$ QCD formulas for evaluating the building blocks (2.19) may be obtained by adapting known large-$N_{\rm f}$ QED results [16]. There are two adaptations to make.

- We need to include overall SU($N_{\rm c}$) color factors associated with high-energy splitting vertices in NLO contributions like figs. 5 and 6.
- In section 2.2, we reviewed the 3-body "potential" $V_3(\boldsymbol{b}_1, \boldsymbol{b}_2, \boldsymbol{b}_3)$ representing medium-averaged correlations between particle interactions in the analysis of leading-order LPM/BDMPS-Z rates. NLO corrections involve times when corresponding 4-body potentials are needed, such as the middle shaded area of fig. 8. We need to change the 4-body $\bar{e}e\bar{e}e$ potential appropriate for large-$N_{\rm f}$ QED [16] to a 4-body $\bar{q}q\bar{q}q$ potential for $N_{\rm f}\gg N_{\rm c}\gg 1$ QCD.

[14] See the discussion in section 1.1 of ref. [21].

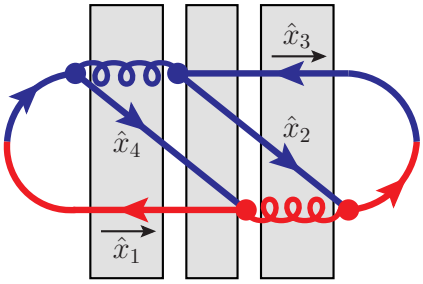

Figure 8. The first time-ordered interference diagram of fig. 5, here showing how we label various energy fractions as $(\hat{x}_1, \hat{x}_2, \hat{x}_3, \hat{x}_4) = (-1, x_{\bar{\mathrm{Q}}}, x_{\mathrm{Q}}, x_q)$ following the convention of ref. [16] inherited from the conventions of refs. [20, 21]. The medium-averaged evolution in the leftmost and rightmost shaded areas are described by 3-body quantum mechanics with non-Hermitian Hamiltonians, similar to the discussion of leading-order rates in section 2.2. The middle shaded area corresponds to a 4-body quantum mechanics problem.

We will discuss the differences more thoroughly below. In addition to identifying the isolated differences below, we provide a complete summary in appendix A of the formulas for the basic rates (2.19), in a form that covers both large-N_{f} QCD and large-N_{f} QED.

3.1 Overall group factors

3.1.1 Basics

The reason that we have taken the large-N_{c} limit in this and previous work on overlap effects in QCD is because the large-N_{c} limit removes the need to keep track of the evolution of the color state of the high-energy particles during 4-body evolution.[15] Because of this simplification, the overall color factors of diagrams decouple from the evolution of color in the medium, and one can read them off by briefly pretending that interference diagrams such as fig. 8 were vacuum diagrams. Summing over final-state colors and averaging over initial-state ones, the overall color factors for fig. 8 are then

$$\frac{\mathrm{tr}(T_{\mathrm{F}}^a T_{\mathrm{F}}^b)\,\mathrm{tr}(T_{\mathrm{F}}^a T_{\mathrm{F}}^b)}{d_{\mathrm{F}}} = \frac{t_{\mathrm{F}}^2 d_{\mathrm{A}}}{d_{\mathrm{F}}} = t_{\mathrm{F}} C_{\mathrm{F}} \qquad [\text{NLO } q \to qg \text{ or } q\mathrm{Q}\bar{\mathrm{Q}}], \tag{3.1}$$

where d_R is the dimension of color representation R and where the last equality follows from the (general-N_{c}) relation that

$$t_{\mathrm{F}} d_{\mathrm{A}} = \mathrm{tr}(T_{\mathrm{F}}^a T_{\mathrm{F}}^a) = C_{\mathrm{F}} d_{\mathrm{F}}. \tag{3.2}$$

Nothing about (3.1) depends on time ordering or whether gluons are transverse or longitudinally polarized, and so the same factor applies to all our $N_{\mathrm{f}} \gg N_{\mathrm{c}} \gg 1$ quark-initiated NLO

[15] In the context of the formalism used for our overlap calculations, this use of the large-N_{c} approximation goes back to ref. [20]. In the same context, discussion of how to go beyond the large-N_{c} limit may be found in refs. [25, 26]. The same issue arises in the somewhat different problem of calculating $p_\perp$ dependence for *leading-order* splitting rates. See for example, refs. [27–29] and the more recent ref. [30].

diagrams. For $N_f \gg N_c \gg 1$ gluon-initiated NLO diagrams, such as the last diagram of fig. 6, the only difference is that we average over d_A initial colors instead of d_F initial colors, leading to an overall factor

$$\frac{\mathrm{tr}(T_F^a T_F^b)\,\mathrm{tr}(T_F^a T_F^b)}{d_A} = t_F^2 \qquad [\text{NLO } g \to Q\bar{Q}]. \tag{3.3}$$

For future reference, note that in both cases (3.1) and (3.3), the *ratio* of NLO rates to LO rates (2.9)[16] will have an overall factor of $t_F \alpha_s$ in $N_f \gg N_c \gg 1$ QCD formulas in place of the factor of α in large-N_f QED formulas.

Later, we will present numerical results in units of the overall color factors described above just for the sake of eliminating this rather simple difference between large-N_f QED and $N_f \gg N_c \gg 1$ QCD when comparing numbers. Then the only difference between the numbers will come from the difference in how the high-energy particles interact with the medium, captured by section 3.2 below.

3.1.2 Implication for certain relations among diagrams

Ref. [16] reduced the work of calculating all interference diagrams for large-N_f QED by showing how some diagrams were related to each other through what were called front-end and back-end transformations. Diagrammatically, a front-end transformation corresponds to taking the earliest-time vertex in an interference diagram and sliding it around the front of the diagram so that it moves from the amplitude to the conjugate amplitude or vice versa. Fig. 9 shows an example which converts a diagram contributing to real double splitting $e \to e\gamma \to e\mathrm{E}\bar{\mathrm{E}}$ into a diagram contributing to NLO single splitting $\gamma \to \mathrm{E}\bar{\mathrm{E}}$. Ref. [16] found that there was a relation among the corresponding contributions to rates,[17]

$$\left[\frac{d\Gamma}{dx_E}\right]_{(o^*)} = -N_f \int_0^1 dx_e \left\{ \left[\frac{d\Gamma}{dx_e\, dx_E}\right]_{(a)} \text{with } (x_e, x_E, E) \to \left(\frac{-x_e}{1-x_e}\,,\, \frac{x_E}{1-x_e}\,,\, (1-x_e)E\right) \right\}. \tag{3.4}$$

In the case of QCD, we have to modify this formula to account for the fact that the rate for $q \to qg \to q\mathrm{Q}\bar{\mathrm{Q}}$ is averaged over the $d_F = N_c$ colors of the initial quark, whereas the rate for $g \to \mathrm{Q}\bar{\mathrm{Q}}$ should be averaged over the d_A colors of the initial gluon. So the front-end relation in this case needs a corresponding factor of d_F/d_A on the right-hand side:

$$\left[\frac{d\Gamma}{dx_Q}\right]_{(o^*)} = \\ -\frac{d_F}{d_A} N_f \int_0^1 dx_q \left\{ \left[\frac{d\Gamma}{dx_q\, dx_Q}\right]_{(a)} \text{with } (x_q, x_Q, E) \to \left(\frac{-x_q}{1-x_q}\,,\, \frac{x_Q}{1-x_q}\,,\, (1-x_q)E\right) \right\}. \tag{3.5}$$

Note that (3.2) means that the new factor may alternatively be written as

$$\frac{d_F}{d_A} = \frac{t_F}{C_F}\,, \tag{3.6}$$

[16] The overall color factors for the LO rates are the C_F or t_F in (2.7).

[17] Taking $2\,\mathrm{Re}[\cdots]$ of our eq. (3.4) here corresponds to the first case covered by eq. (4.3) of ref. [16]. Our x_E here is called y_e there.

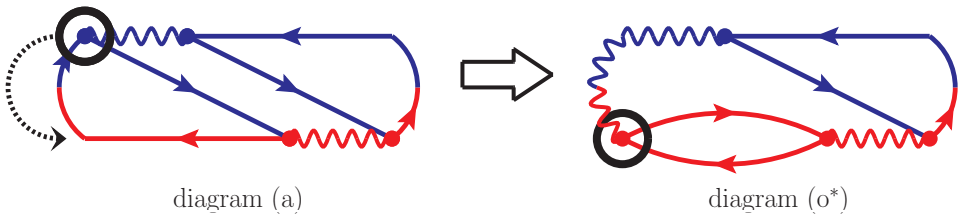

Figure 9. Graphical example of a "front-end" transformation taken from fig. 25 of ref. [16]. The diagram names (a) and (o) correspond to those of ref. [16] and fig. 18 except that (o*) here means the complex conjugate of diagram (o) there.

which (as it must be) is just the ratio of the previously-discussed overall color factor for NLO $g \to \mathrm{Q}\bar{\mathrm{Q}}$ (3.3) to that for $q \to q\mathrm{Q}\bar{\mathrm{Q}}$ (3.1).

3.2 Potentials

In order to understand how to write down the 4-body "potential" $V_4(\boldsymbol{b}_1, \boldsymbol{b}_2, \boldsymbol{b}_3, \boldsymbol{b}_4)$ appropriate to medium-averaged evolution in the middle shaded area of fig. 8, we need to understand what correlations are allowed between high-energy particles in the large-N_c limit. The general diagrammatic rules for large-N_c QCD are that (i) Feynman diagrams should be planar and (ii) fermion lines should define an oriented boundary to the planar region in which the gluon lines are drawn [31]. A corresponding version of fig. 8 is depicted by the thick colored lines in fig. 10. Unlike the previous figure, fig. 10 also explicitly shows a few simple examples of medium-averaged correlations between interactions of the high-energy particles with the medium. Those examples of correlations are represented by the thin black gluon lines. We've used 2-point correlations as an example that's easy to draw, but higher-point correlations are possible too, since we do not assume that the medium is itself weakly-coupled. In this graph, the two fermion loops define holes cut out of the plane.

Correlations should be effectively instantaneous compared to the scale of the diagram because high-energy formation times are large compared to the correlation length of the medium, and this hierarchy is what makes possible the treatment of each shaded area of fig. 8 as a type of non-relativistic quantum mechanics problem. But the planar drawing of the correlators in fig. 10 obscures the approximately instantaneous nature of the correlations. Following refs. [20, 21],[18] a better way to visualize a large-N_c planar diagram when time ordering is important is to draw the diagram on a cylinder instead of on a plane, with time ordered along the length of the cylinder. Any Feynman diagram that can be drawn in the plane without crossing lines can also be drawn on the surface of a cylinder without crossing lines, and vice versa, but the cylinder allows us to simultaneously visualize the time-ordering. Fig. 11 shows a version of fig. 10 drawn on a time-ordered cylinder. Here, we also find it useful to use 't Hooft double line notation for the high-energy gluon lines. In the large-N_c limit all correlations generated

[18] See in particular section 4.3 of ref. [20] and section 2.2.1 of ref. [21].

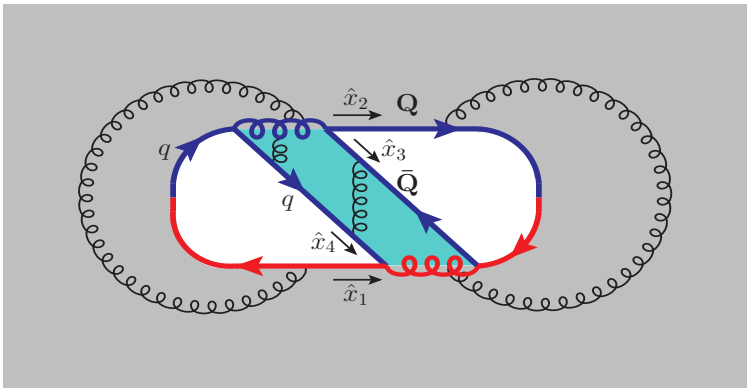

Figure 10. A large-N_c planar drawing of (i) fig. 8 supplemented by (ii) a few simple examples of (2-point) medium-averaged correlations of high-energy particle interactions with the medium (represented by thin black gluon lines). The shaded region (both colors) is the section of the plane where large-N_c gluon lines are drawn, with the quark loops defining the region's boundary. Note that we had to interchange where the Q and $\bar{\mathrm{Q}}$ lines of fig. 8 are drawn in order that the region have a consistently oriented boundary.

by the medium must lie completely within one of the two shaded areas shown (which is the same shading as fig. 10 but is unrelated to the shading of fig. 8).

Using this large-N_c picture, we now revisit 3-body evolution and implement 4-body evolution.

3.2.1 Initial 3-body time evolution

Consider first the initial region of 3-body time evolution in fig. 11. We will refer to the thick lines as fundamental (F) or anti-fundamental ($\bar{\mathrm{F}}$) color lines depending on how they are oriented in the diagram relative to the forward time direction. In the large-N_c limit, correlations (whether 2-point or higher) between interactions of the high-energy particles are only allowed (i) across the gray region between the red $\bar{\mathrm{F}}$ line ($\hat{x}_1$) and the blue F-line component of the gluon, or (ii) across the cyan region between the daughter-quark blue F line ($x_q{=}\hat{x}_4$) and the blue $\bar{\mathrm{F}}$-line component of the gluon. The corresponding potential should therefore decomposes into the sum of 2-body F$\bar{\mathrm{F}}$ potentials for (i) and (ii):[19]

$$V_{3,\mathrm{i}}(\boldsymbol{b}_1,\boldsymbol{b}_g,\boldsymbol{b}_q) = V_{\mathrm{F}\bar{\mathrm{F}}}(\boldsymbol{b}_g{-}\boldsymbol{b}_1) + V_{\mathrm{F}\bar{\mathrm{F}}}(\boldsymbol{b}_q{-}\boldsymbol{b}_g) = -\frac{i\hat{q}_{\mathrm{F}}}{4}(\boldsymbol{b}_g{-}\boldsymbol{b}_1)^2 - \frac{i\hat{q}_{\mathrm{F}}}{4}(\boldsymbol{b}_g{-}\boldsymbol{b}_q)^2. \tag{3.7}$$

This is the same as the more general 3-particle potential (2.2) with particles $(1,2,3)$ there referring to $(1,g,q)$ here and using the large-N_c relation $\hat{q}_{\mathrm{A}} = 2\hat{q}_{\mathrm{F}}$. As reviewed earlier, the 3-body quantum mechanics problem can be reduced to an effective 1-body problem. The mass

[19] The factor of $\frac{1}{4}$ in $V_{\mathrm{F}\bar{\mathrm{F}}}(\Delta b) = -\frac{i\hat{q}_{\mathrm{F}}}{4}(\Delta b)^2$ is the same factor of 4 that relates the diffusion constant κ in the $\boldsymbol{p}_\perp$ diffusion equation $\partial_t\rho(\boldsymbol{p}_\perp,t) = \kappa\nabla^2_{\boldsymbol{p}_\perp}\rho(\boldsymbol{p}_\perp,t)$ to the original definition of $\hat{q}$ in terms of the time dependence of the second moment of the diffusion equation's solution, $\langle \boldsymbol{p}_\perp^2\rangle = \hat{q}t$. See, for example, section 2.2 of ref. [7].

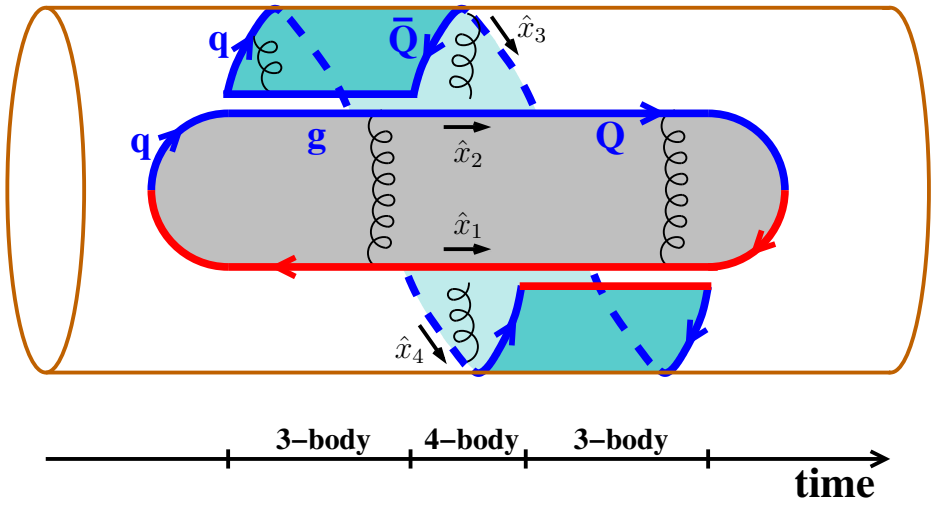

Figure 11. A re-drawing of fig. 10 on a time-ordered cylinder. The dashed lines indicate lines that are wrapping around the back of the cylinder. All of the thick lines correspond to the fundamental (quark) color representation flowing in the direction of the arrows. The color of large-N_c gluons is represented by a pair of fundamental color lines flowing in opposite directions, which we have drawn explicitly for the high-energy gluons. (One may draw the correlations using double-line representation as well, but we didn't find that helpful for this discussion.) The thick lines all interact with the medium, and the correlations (black) arising from medium-averaging of those interactions must (in the large-N_c limit) each be routable entirely through one of the two disjoint shaded regions above, without crossing any other lines. The simple examples of correlations shown here correspond to those in fig. 10, and the third correlation (which is between particles 3 and 4) runs around the back of the cylinder, through the cyan region.

and frequency (2.4b) of the latter correspond here to

$$M_{\rm i} = x_q(1-x_q)E, \qquad \Omega_{\rm i} = \sqrt{-\frac{i\hat{q}_{\rm F}}{2E}\left(-1+\frac{1}{x_q}+\frac{2}{x_g}\right)} \qquad (N_{\rm c}\gg 1 \text{ QCD}). \tag{3.8}$$

The above formula for $\Omega_{\rm i}$ is an example of a low-level QCD modification that needs to be made to the large-$N_{\rm f}$ QED formulas of ref. [16] for overlap corrections. The convention of ref. [16] is to write final formulas in terms of the momentum fractions

$$(\hat{x}_1, \hat{x}_2, \hat{x}_3, \hat{x}_4) = (-1, x_{\rm Q}, x_{\bar{\rm Q}}, x_q) \tag{3.9}$$

of the four particles appearing in the 4-body evolution section of figures like figs. 8 and 11. So we rewrite (3.8) as

$$M_{\rm i} = \hat{x}_1\hat{x}_4(\hat{x}_1+\hat{x}_4)E, \qquad \Omega_{\rm i} = \sqrt{-\frac{i\hat{q}_{\rm F}}{2E}\left(\frac{1}{\hat{x}_1}+\frac{1}{\hat{x}_4}-\frac{2}{\hat{x}_1+\hat{x}_4}\right)} \qquad (N_{\rm c}\gg 1 \text{ QCD}). \tag{3.10}$$

3.2.2 4-body time evolution

Now turn to the region of 4-body time evolution in fig. 11. Here again the potential splits into a sum of two $\mathrm{F\bar{F}}$ potentials: one for correlations through the gray region of the red parent-quark line ($\hat{x}_1$) with Q and the other through the cyan region of q with $\bar{\mathrm{Q}}$. The large-N_c 4-body potential is then

$$V_4(\boldsymbol{b}_1, \boldsymbol{b}_\mathrm{Q}, \boldsymbol{b}_{\bar{\mathrm{Q}}}, \boldsymbol{b}_q) = V_{\mathrm{F}\bar{\mathrm{F}}}(\boldsymbol{b}_\mathrm{Q} - \boldsymbol{b}_1) + V_{\mathrm{F}\bar{\mathrm{F}}}(\boldsymbol{b}_q - \boldsymbol{b}_{\bar{\mathrm{Q}}}) = -\frac{i\hat{q}_\mathrm{F}}{4}(\boldsymbol{b}_\mathrm{Q} - \boldsymbol{b}_1)^2 - \frac{i\hat{q}_\mathrm{F}}{4}(\boldsymbol{b}_q - \boldsymbol{b}_{\bar{\mathrm{Q}}})^2 \tag{3.11}$$

or, using the particle numbering scheme of (3.9) throughout,

$$V_4(\boldsymbol{b}_1, \boldsymbol{b}_2, \boldsymbol{b}_3, \boldsymbol{b}_4) = -\frac{i\hat{q}_\mathrm{F}}{4}\left[(\boldsymbol{b}_2 - \boldsymbol{b}_1)^2 + (\boldsymbol{b}_4 - \boldsymbol{b}_3)^2\right]. \tag{3.12}$$

Ref. [20] discuss how 3-dimensional rotational symmetry can be used to generally reduce such 4-body problems to effective 2-body problems in terms of any two of the set of variables[20]

$$\boldsymbol{C}_{ij} \equiv \frac{\boldsymbol{b}_i - \boldsymbol{b}_j}{x_i + x_j}. \tag{3.13}$$

Focusing just on the potential for the moment, and using the fact that $x_1 + x_2 + x_3 + x_4 = 0$, the potential (3.12) may be written as

$$V_4 = -\frac{i\hat{q}_\mathrm{F}}{4}(x_3 + x_4)^2(C_{12}^2 + C_{34}^2). \tag{3.14}$$

The kinetic terms appropriate to this problem do not depend on the details of how the particles interact with the medium; they are the same as those for the pure gluon case [20] or the QED case [16]. In terms of the variables $(\boldsymbol{C}_{12}, \boldsymbol{C}_{34})$ and their conjugate momenta $(\boldsymbol{P}_{12}, \boldsymbol{P}_{34})$, the effective Hamiltonian is

$$\mathcal{H}_4 = \frac{P_{12}^2}{2x_1x_2(x_1+x_2)E} + \frac{P_{34}^2}{2x_3x_4(x_3+x_4)E} + V_4(\boldsymbol{C}_{12}, \boldsymbol{C}_{34}). \tag{3.15}$$

For our particular potential (3.14), the C_{12} and C_{34} degrees of freedom completely decouple. In order to draw on results for overlap corrections from previous work, it will be useful to adopt the same notation as ref. [20] and rewrite this harmonic oscillator problem as

$$\mathcal{H}_4 = \frac{1}{2}\begin{pmatrix}\boldsymbol{P}_{34}\\ \boldsymbol{P}_{12}\end{pmatrix}^\top \mathfrak{M}^{-1}\begin{pmatrix}\boldsymbol{P}_{34}\\ \boldsymbol{P}_{12}\end{pmatrix} + \frac{1}{2}\begin{pmatrix}\boldsymbol{C}_{34}\\ \boldsymbol{C}_{12}\end{pmatrix}^\top \mathfrak{K}\begin{pmatrix}\boldsymbol{C}_{34}\\ \boldsymbol{C}_{12}\end{pmatrix} \tag{3.16}$$

where

$$\mathfrak{M} = \begin{pmatrix} x_3x_4(x_3+x_4) & \\ & x_1x_2(x_1+x_2)\end{pmatrix} E = \begin{pmatrix} x_3x_4 & \\ & -x_1x_2\end{pmatrix}(x_3+x_4)E \tag{3.17}$$

[20] The normalization $(x_i + x_j)^{-1}$ in (3.13) is just a convenience that makes the $\boldsymbol{C}$'s natural generalizations of the variable $\boldsymbol{B}$ discussed earlier for 3-body evolution (2.3). Putting that convenience aside, we could have said more simply that the 4-body problem could be reduced to an effective 2-body problem in terms of any two of the variables $\boldsymbol{b}_i - \boldsymbol{b}_j$.

is the analog of a mass matrix and

$$\mathfrak{K} = -\frac{i\hat{q}_{\rm F}}{2}(x_3+x_4)^2 \begin{pmatrix} 1 & \\ & 1 \end{pmatrix} \tag{3.18}$$

is the analog of a spring constant matrix, taken here from (3.14). Because $\boldsymbol{C}_{34}$ and $\boldsymbol{C}_{12}$ decouple here, and the two transverse spatial directions decouple, the normal modes are simply

$$\begin{pmatrix} C^+_{34} \\ C^+_{12} \end{pmatrix} = \frac{1}{\sqrt{x_3x_4(x_3+x_4)E}} \begin{pmatrix} 1 \\ 0 \end{pmatrix} \qquad \text{and} \qquad \begin{pmatrix} C^-_{34} \\ C^-_{12} \end{pmatrix} = \frac{1}{\sqrt{x_1x_2(x_1+x_2)E}} \begin{pmatrix} 0 \\ 1 \end{pmatrix}, \tag{3.19}$$

for each transverse direction. Again following ref. [20] for compatibility, we have normalized our normal modes so that

$$\begin{pmatrix} \boldsymbol{C}^j_{34} \\ \boldsymbol{C}^j_{12} \end{pmatrix}^\top \mathfrak{M} \begin{pmatrix} \boldsymbol{C}^{j'}_{34} \\ \boldsymbol{C}^{j'}_{12} \end{pmatrix} = \delta^{jj'}. \tag{3.20}$$

The corresponding normal mode frequencies are

$$\Omega_+ = \sqrt{-\frac{i\hat{q}_{\rm F}}{2E}\left(\frac{1}{x_3}+\frac{1}{x_4}\right)}, \qquad \Omega_- = \sqrt{-\frac{i\hat{q}_{\rm F}}{2E}\left(\frac{1}{x_1}+\frac{1}{x_2}\right)}. \tag{3.21}$$

Earlier work such as [16, 20, 21], that we want to adapt to the case of large-$N_{\rm f}$ QCD, package all the normal modes into columns of a matrix. We will call the corresponding matrix

$$a_{34,12} \equiv \begin{pmatrix} C^+_{34} & C^-_{34} \\ C^+_{12} & C^-_{12} \end{pmatrix} = \begin{pmatrix} \frac{1}{\sqrt{x_3x_4(x_3+x_4)E}} & 0 \\ 0 & \frac{1}{\sqrt{x_1x_2(x_1+x_2)E}} \end{pmatrix}, \tag{3.22}$$

where here we use the subscript on $a_{34,12}$ to indicate that we have specified the normal modes in terms of the values of $(\boldsymbol{C}_{34}, \boldsymbol{C}_{12})$.

Though the choice of variables $(\boldsymbol{C}_{34}, \boldsymbol{C}_{12})$ diagonalized the Hamiltonian in this particular case, that is a quirk of large-$N_{\rm f}$ QCD. Previous work on diagrams analogous to fig. 8 for large-$N_{\rm f}$ QED [16] and purely gluonic splitting [21] instead used the basis $(\boldsymbol{C}_{41}, \boldsymbol{C}_{23})$, which is convenient because $\boldsymbol{C}_{23} = 0$ at the start of the 4-body evolution because of the vertex that brings particles 2 and 3 together there, and $\boldsymbol{C}_{41} = 0$ at the end of 4-body evolution because of the vertex that brings particles 4 and 1 together. The two sets of variables are related by[21]

$$\begin{pmatrix} C_{41} \\ C_{23} \end{pmatrix} = \mathcal{S} \begin{pmatrix} C_{34} \\ C_{12} \end{pmatrix}. \tag{3.23}$$

with transformation matrix

$$\mathcal{S} = \frac{1}{(x_1+x_4)} \begin{pmatrix} -x_3 & -x_2 \\ x_4 & x_1 \end{pmatrix}. \tag{3.24a}$$

[21] This relation comes from eq. (5.31) of ref. [20]. Similar to our earlier footnote 8, the relation may be derived using the fact that $x_1+x_2+x_3+x_4 = 0$ and the constraint $x_1\boldsymbol{b}_1 + x_2\boldsymbol{b}_2 + x_3\boldsymbol{b}_3 + x_4\boldsymbol{b}_4 = 0$.

For the new choice of variables, the matrix of normal modes, which we might call $a_{41,23}$ here but instead call a_y in earlier work [16, 20, 21], becomes

$$a_y \equiv a_{41,23} \equiv \begin{pmatrix} C_{41}^+ & C_{41}^- \\ C_{23}^+ & C_{23}^- \end{pmatrix} = \mathcal{S}\, a_{34,12}. \tag{3.24b}$$

Equations (3.21), (3.22), and (3.24) for $\Omega_\pm$ and a_y give the specific formulas needed to update the large-N_f 4-body QED evolution in ref. [16] to large-N_f QCD.

There is a related change to cover. In large-N_f QED, one of the 4-body evolution frequencies $\Omega_\pm$ vanished. Ref. [16] labeled that frequency Ω_-, and so $\Omega_- = 0$. In general, the 4-body frequencies appear in formulas for overlap effects in the combinations $\Omega_\pm \cot(\Omega_\pm\, \Delta t)$ and $\Omega_\pm \csc(\Omega_\pm\, \Delta t)$ (see, for instance, appendix A of ref. [24]). But in the large-N_f QED case [16], the Ω_- combinations were replaced by their $\Omega_-{=}0$ limits,

$$\Omega_- \cot(\Omega_-\, \Delta t) \longrightarrow \frac{1}{\Delta t} \qquad \text{and} \qquad \Omega_- \csc(\Omega_-\, \Delta t) \longrightarrow \frac{1}{\Delta t} \qquad \text{(large-}N_\mathrm{f}\text{ QED)}. \tag{3.25}$$

In large-N_f QCD, neither Ω_+ nor Ω_- vanish (3.21), and so we must undo the replacement (3.25) to convert large-N_f QED formulas to large-N_f QCD.

3.2.3 Final 3-body time evolution

The final region of 3-body evolution in fig. 11 is similar to the first region except that the particles involved are different. Eqs. (3.7) and (3.10) become

$$V_{3,\mathrm{f}}(\boldsymbol{b}_{\bar{\mathrm{Q}}}, \boldsymbol{b}_g, \boldsymbol{b}_\mathrm{Q}) = V_{\mathrm{F}\bar{\mathrm{F}}}(\boldsymbol{b}_g{-}\boldsymbol{b}_{\bar{\mathrm{Q}}}) + V_{\mathrm{F}\bar{\mathrm{F}}}(\boldsymbol{b}_\mathrm{Q}{-}\boldsymbol{b}_g) = -\frac{i\hat{q}_\mathrm{F}}{4}(\boldsymbol{b}_g{-}\boldsymbol{b}_{\bar{\mathrm{Q}}})^2 - \frac{i\hat{q}_\mathrm{F}}{4}(\boldsymbol{b}_g{-}\boldsymbol{b}_\mathrm{Q})^2, \tag{3.26}$$

where b_g now refers to the transverse position of the *conjugate*-amplitude (red) gluon in fig. 11, and[22]

$$M_\mathrm{f}^\mathrm{seq} = \hat{x}_2\hat{x}_3(\hat{x}_2{+}\hat{x}_3)E, \qquad \Omega_\mathrm{i}^\mathrm{seq} = \sqrt{-\frac{i\hat{q}_\mathrm{F}}{2E}\left(\frac{1}{\hat{x}_2} + \frac{1}{\hat{x}_3} - \frac{2}{\hat{x}_2+\hat{x}_3}\right)} \qquad (N_\mathrm{c}{\gg}1\text{ QCD}). \tag{3.27}$$

4 Net rates

4.1 Definition

Shower development can be conveniently packaged in terms of "net" rates for a splitting or pair of overlapping splittings to produce one daughter of energy xE (plus any other daughters) from a parent of energy E [13, 14, 17, 24]. Here, we exactly follow ref. [17] to define our net rates $[d\Gamma/dx]^\mathrm{net}_{\underline{i\to j}}$ for parents of type i producing a daughter of type j, where underlining of

[22] The superscript "seq" stands for "sequential diagrams," which was a necessary distinction to draw in early work [20, 21] on overlapping $g \to gg \to ggg$ where M for the final 3-body evolution was different for different classes of diagrams. We keep the superscript here for consistency of notation.

subscripts like $\underline{q \to q}$ indicates that we are using the large-N_f limit to distinguish the pair-produced quark (Q) from the other quark daughter (q) in overlapping splitting rates. The leading-order contributions are simply

$$\left[\frac{d\Gamma}{dx}\right]^{\mathrm{LO}}_{\underline{q\to q}} \equiv \left[\frac{d\Gamma}{dx_q}\right]^{\mathrm{LO}}_{q\to qg} \qquad \text{with } x_q = x, \tag{4.1a}$$

$$\left[\frac{d\Gamma}{dx}\right]^{\mathrm{LO}}_{\underline{q\to g}} \equiv \left[\frac{d\Gamma}{dx_q}\right]^{\mathrm{LO}}_{q\to qg} \qquad \text{with } x_q = 1-x, \tag{4.1b}$$

$$\left[\frac{d\Gamma}{dx}\right]^{\mathrm{LO}}_{\underline{g\to \mathrm{Q}}} \equiv \left[\frac{d\Gamma}{dx_\mathrm{Q}}\right]^{\mathrm{LO}}_{g\to \mathrm{Q}\bar{\mathrm{Q}}} \qquad \text{with } x_\mathrm{Q} = x, \tag{4.1c}$$

and the NLO contributions are

$$\left[\frac{d\Gamma}{dx}\right]^{\mathrm{NLO}}_{\underline{q\to q}} \equiv \left[\Delta\frac{d\Gamma}{dx_q}\right]^{\mathrm{NLO}}_{q\to qg} + \int_0^{1-x_q} dx_\mathrm{Q}\, \left[\Delta\frac{d\Gamma}{dx_q\, dx_\mathrm{Q}}\right]_{q\to q\mathrm{Q}\bar{\mathrm{Q}}} \qquad \text{with } x_q = x, \tag{4.2a}$$

$$\left[\frac{d\Gamma}{dx}\right]^{\mathrm{NLO}}_{\underline{q\to \mathrm{Q}}} \equiv \int_0^{1-x_\mathrm{Q}} dx_q\, \left[\Delta\frac{d\Gamma}{dx_q\, dx_\mathrm{Q}}\right]_{q\to q\mathrm{Q}\bar{\mathrm{Q}}} \qquad \text{with } x_\mathrm{Q} = x, \tag{4.2b}$$

$$\left[\frac{d\Gamma}{dx}\right]^{\mathrm{NLO}}_{\underline{q\to \bar{\mathrm{Q}}}} \equiv \int_0^{1-x_{\bar{\mathrm{Q}}}} dx_q\, \left(\left[\Delta\frac{d\Gamma}{dx_q\, dx_\mathrm{Q}}\right]_{q\to q\mathrm{Q}\bar{\mathrm{Q}}}\right)_{x_\mathrm{Q}=1-x_q-x_{\bar{\mathrm{Q}}}} \qquad \text{with } x_{\bar{\mathrm{Q}}} = x, \tag{4.2c}$$

$$\left[\frac{d\Gamma}{dx}\right]^{\mathrm{NLO}}_{\underline{q\to g}} \equiv \left[\Delta\frac{d\Gamma}{dx_q}\right]^{\mathrm{NLO}}_{q\to qg} \qquad \text{with } x_q = 1-x, \tag{4.2d}$$

$$\left[\frac{d\Gamma}{dx}\right]^{\mathrm{NLO}}_{\underline{g\to \mathrm{Q}}} \equiv \left[\Delta\frac{d\Gamma}{dx_\mathrm{Q}}\right]^{\mathrm{NLO}}_{g\to \mathrm{Q}\bar{\mathrm{Q}}} \qquad \text{with } x_\mathrm{Q} = x. \tag{4.2e}$$

4.2 Numerics and fits for net rates

4.2.1 Basic net rates

The NLO net rates are computed using (4.2) and the formulas of appendix A. Since the latter formulas are complicated, and the numerical integrals involved are computationally expensive, we then approximate the results for the net rates by reasonably accurate fits to relatively simple analytic functions of x. Those fit functions may then be used for numerically efficient calculations of shower development.

Following ref. [17], we find it easier to first transform the NLO net rates $[d\Gamma/dx]^{\mathrm{NLO}}_{\underline{i\to j}}$ into smoother functions $f_{\underline{i\to j}}(x)$ before fitting them. We find it easiest to factor out the power-law

behavior of the rates as $x\to 0$ and $x\to 1$ and also to remove some of the logarithmic dependence. Specifically, we define the $f_{\underline{i\to j}}(x)$ by

$$\left[\frac{d\Gamma}{dx}\right]^{\text{NLO}}_{\underline{i\to j}} = L_{\underline{i\to j}}(x,\mu) + f_{\underline{i\to j}}(x)\, R_{\underline{i\to j}}(x), \tag{4.3}$$

where

$$R_{\underline{q\to q}}(x_q) \equiv x_q^{-1/2}(1-x_q)^{-3/2}\,\frac{N_{\text{f}} t_{\text{F}} C_{\text{F}} \alpha_{\text{s}}^2}{2\pi}\sqrt{\frac{\hat{q}_{\text{F}}}{E}}\,, \tag{4.4a}$$

$$R_{\underline{q\to \text{Q}}}(x_{\text{Q}}) \equiv x_{\text{Q}}^{-3/2}(1-x_{\text{Q}})^{+1/2}\,\frac{N_{\text{f}} t_{\text{F}} C_{\text{F}} \alpha_{\text{s}}^2}{2\pi}\sqrt{\frac{\hat{q}_{\text{F}}}{E}}\,, \tag{4.4b}$$

$$R_{\underline{q\to \bar{\text{Q}}}}(x_{\bar{\text{Q}}}) \equiv R_{\underline{q\to \text{Q}}}(x_{\bar{\text{Q}}}), \tag{4.4c}$$

$$R_{\underline{q\to g}}(x_g) \equiv R_{\underline{q\to q}}(1-x_g), \tag{4.4d}$$

$$R_{\underline{g\to \text{Q}}}(x_{\text{Q}}) \equiv x_{\text{Q}}^{-1/2}(1-x_{\text{Q}})^{-1/2}\,\frac{N_{\text{f}}^2 t_{\text{F}}^2 \alpha_{\text{s}}^2}{2\pi}\sqrt{\frac{\hat{q}_{\text{F}}}{E}} \tag{4.4e}$$

and

$$L_{\underline{q\to q}}(x_q,\mu) \equiv -\frac{\beta_0\alpha_{\text{s}}}{2}\left[\frac{d\Gamma}{dx_q}\right]^{q\to qg}_{\text{LO}} \ln\left(\frac{\mu^2}{\sqrt{\frac{(1-x_q)\hat{q}_{\text{F}}E}{x_q}}}\right), \tag{4.5a}$$

$$L_{\underline{q\to \text{Q}}} \equiv L_{\underline{q\to \bar{\text{Q}}}} \equiv 0, \tag{4.5b}$$

$$L_{\underline{q\to g}}(x_g,\mu) \equiv L_{\underline{q\to q}}(1-x_g,\mu), \tag{4.5c}$$

$$L_{\underline{g\to \text{Q}}}(x_{\text{Q}},\mu) \equiv -\frac{\beta_0\alpha_{\text{s}}}{2}\left[\frac{d\Gamma}{dx_{\text{Q}}}\right]^{g\to \text{Q}\bar{\text{Q}}}_{\text{LO}} \ln\left(\frac{\mu^2}{\sqrt{\hat{q}_{\text{F}}E}}\right). \tag{4.5d}$$

Above, β_0 is the coefficient of the 1-loop renormalization group β function for α_{s} in the large-N_{f} limit,

$$\beta_0 = \frac{2 t_{\text{F}} N_{\text{f}}}{3\pi}\,. \tag{4.6}$$

With these definitions, table 2 and figure 12 present our numerical results for the functions $f_{\underline{i\to j}}(x)$, from which our original numerical results for NLO net rates can be recovered using (4.3).

In large-N_{f} QED, we found in ref. [17] that $f_{\underline{e\to \text{E}}}(x) = f_{\underline{e\to \bar{\text{E}}}}(x)$. Table 2 shows that in large-N_{f} QCD, there is instead a small difference between $f_{\underline{q\to \text{Q}}}(x)$ and $f_{\underline{q\to \bar{\text{Q}}}}(x)$. This difference, and its persistence in the limit of small x, turns out to be the source of the feature in the last row of table 1 that characteristics of the fermion-number deposition distribution are infrared unsafe for large-N_{f} QCD. But we save that discussion for later.

Our fits to the numerical data of table 2 are

$$\begin{aligned} f_{\underline{q\to q}}(x) = {} & 0.55622 - 1.17795\,x + 0.49222\,x^2 - 0.61229\,x^3 \\ & + 0.02989\,x^{1/2} + 0.02248\,x^{3/2} + 1.16702\,x^{5/2} \\ & - 0.00178\,(1-x)^{1/2} - 0.16099\,(1-x)^{3/2} - 0.57232\,(1-x)^{5/2}, \end{aligned} \tag{4.7a}$$

x	$f_{\underline{q\to q}}$	$f_{\underline{q\to \mathrm{Q}}}$	$f_{\underline{q\to \bar{\mathrm{Q}}}}$	$f_{\underline{q\to g}}$	$f_{\underline{g\to \mathrm{Q}}}$
0.0001	-0.1786	0.6710	0.6759	-0.6274	-0.0304
0.0005	-0.1777	0.6694	0.6743	-0.6272	-0.0272
0.001	-0.1773	0.6678	0.6727	-0.6269	-0.0249
0.005	-0.1744	0.6586	0.6637	-0.6241	-0.0151
0.01	-0.1711	0.6500	0.6552	-0.6206	-0.0082
0.025	-0.1620	0.6301	0.6356	-0.6103	0.0045
0.05	-0.1482	0.6044	0.6104	-0.5934	0.0171
0.075	-0.1351	0.5832	0.5895	-0.5770	0.0250
0.1	-0.1223	0.5647	0.5712	-0.5609	0.0308
0.15	-0.0975	0.5331	0.5396	-0.5301	0.0384
0.2	-0.0728	0.5065	0.5127	-0.5009	0.0430
0.25	-0.0478	0.4835	0.4891	-0.4732	0.0457
0.3	-0.0222	0.4633	0.4681	-0.4471	0.0473
0.35	0.0041	0.4457	0.4496	-0.4225	0.0482
0.4	0.0315	0.4305	0.4334	-0.3995	0.0487
0.45	0.0600	0.4178	0.4197	-0.3780	0.0490
0.5	0.0898	0.4078	0.4087	-0.3578	0.0490
0.55	0.1210	0.4007	0.4006	-0.3391	0.0490
0.6	0.1536	0.3969	0.3959	-0.3217	0.0487
0.65	0.1879	0.3967	0.3947	-0.3057	0.0482
0.7	0.2238	0.4005	0.3977	-0.2912	0.0473
0.75	0.2614	0.4087	0.4050	-0.2782	0.0457
0.8	0.3008	0.4217	0.4173	-0.2671	0.0430
0.85	0.3421	0.4399	0.4348	-0.2583	0.0384
0.9	0.3853	0.4638	0.4580	-0.2536	0.0308
0.925	0.4076	0.4780	0.4719	-0.2541	0.0250
0.95	0.4304	0.4937	0.4873	-0.2589	0.0171
0.975	0.4537	0.5110	0.5044	-0.2748	0.0045
0.99	0.4680	0.5223	0.5154	-0.3057	-0.0082
0.995	0.4728	0.5261	0.5193	-0.3338	-0.0151
0.999	0.4766	0.5293	0.5224	-0.4081	-0.0249
0.9995	0.4771	0.5296	0.5228	-0.4424	-0.0272
0.9999	0.4775	0.5299	0.5230	-0.5249	-0.0304

Table 2. Results for the functions $f_{\underline{i\to j}}(x)$ extracted from numerical computation of NLO net rates (4.2) using the explicit formulas of appendix A. Numerical results for the rates were translated into numerical results for $f_{\underline{i\to j}}$ using the definition (4.3) of the $f_{\underline{i\to j}}$.

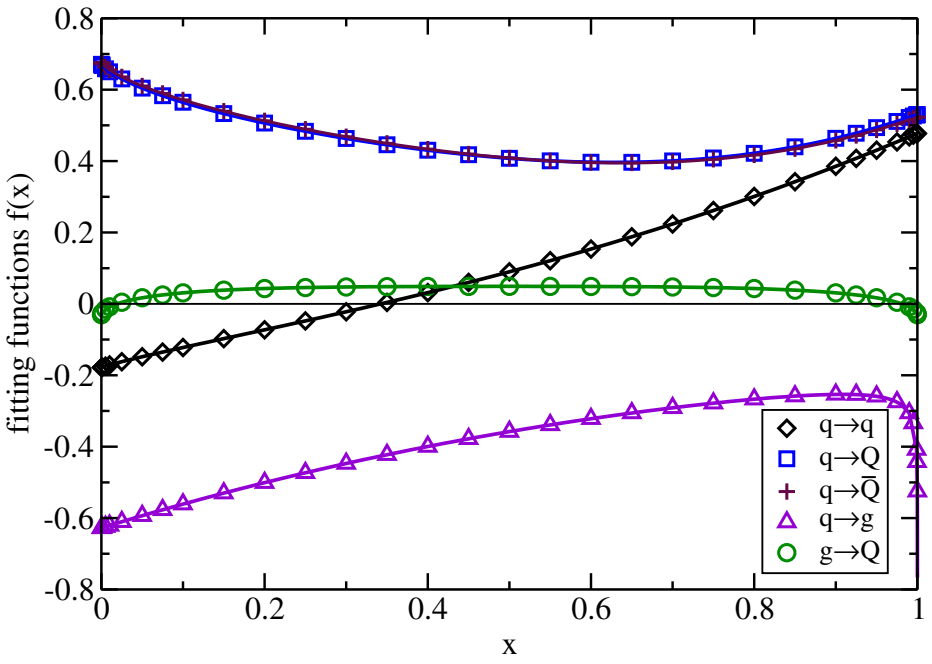

Figure 12. Plots of numerically-computed data points (table 2) and fits (4.7) for the functions $f_{\underline{i\to j}}(x)$ defined by (4.3). The $q\to$Q and $q\to\bar{\text{Q}}$ points are almost but (importantly) not quite on top of each other.

$$f_{\underline{q\to \text{Q}}}(x) = 0.99693 - 1.93966\,x - 1.67427\,x^2 + 0.73141\,x^3 \\ - 0.11846\,x^{1/2} + 2.41297\,x^{3/2} + 0.12113\,x^{5/2} \\ - 0.00132\,(1{-}x)^{1/2} - 0.14081\,(1{-}x)^{3/2} - 0.18232\,(1{-}x)^{5/2}, \quad (4.7b)$$

$$f_{\underline{q\to \bar{\text{Q}}}}(x) = 0.99862 - 1.91570\,x - 1.99018\,x^2 + 0.58225\,x^3 \\ - 0.11797\,x^{1/2} + 2.44638\,x^{3/2} + 0.51974\,x^{5/2} \\ - 0.00119\,(1{-}x)^{1/2} - 0.13183\,(1{-}x)^{3/2} - 0.18823\,(1{-}x)^{5/2}, \quad (4.7c)$$

$$f_{\underline{q\to g}}(x) = \tfrac{1}{6\pi}\ln(1{-}x) - 4.00177 + 8.58463\,x - 4.00386\,x^2 + 1.63579\,x^3 \\ - 0.00727\,x^{1/2} - 0.50996\,x^{3/2} - 1.73122\,x^{5/2} \\ - 0.24648\,(1{-}x)^{1/2} + 1.19122\,(1{-}x)^{3/2} + 2.42961\,(1{-}x)^{5/2}, \quad (4.7d)$$

$$f_{\underline{g\to \text{Q}}}(x) = -0.03304 + 0.26349\,\big(x(1{-}x)\big)^{1/2} - 0.11723\,x(1{-}x) \\ - 0.18078\,\big(x(1{-}x)\big)^{3/2} + 0.03594\,\big(x(1{-}x)\big)^{2}. \quad (4.7e)$$

The fits (4.7) match the original numerical data points of table 2 to better than 0.0003 absolute error.

The $\ln(1-x)$ term in $f_{\underline{q\to g}}(x)$ is the same as it was for large-N_f QED [17]. However, large-N_f QED had a $\ln(1-x)$ term in $f_{\underline{e\to e}}(x)$ and a $\ln x$ term in $f_{\underline{e\to \mathrm{E}}}(x) = f_{\underline{e\to \bar{\mathrm{E}}}}(x)$ that do not appear in large-N_f QCD. The logarithms or lack of them are discussed in appendix B and section 8.

4.2.2 Decomposition into real and virtual parts

Some readers may be interested in how the NLO net rate $[d\Gamma/dx]^{\mathrm{NLO}}_{\underline{q\to q}}$ splits into real and virtual processes. Following ref. [17], we split (4.2a) into the sum of (i) a real double splitting ($q \to qg \to q\mathrm{Q}\bar{\mathrm{Q}}$) piece,

$$\int_0^{1-x_q} dx_\mathrm{Q} \left[\Delta \frac{d\Gamma}{dx_q\, dx_\mathrm{Q}}\right]_{q\to q\mathrm{Q}\bar{\mathrm{Q}}} = f^{\mathrm{real}}_{q\to q}(x)\, R_{\underline{q\to q}}(x) \tag{4.8}$$

and (ii) the virtual correction to single splitting $q \to qg$,

$$\left[\Delta \frac{d\Gamma}{dx_q}\right]^{\mathrm{NLO}}_{q\to qg} = L_{\underline{q\to q}}(x,\mu) + f^{\mathrm{virt}}_{q\to q}(x)\, R_{\underline{q\to q}}(x). \tag{4.9}$$

Then

$$f_{\underline{q\to q}}(x) = f^{\mathrm{virt}}_{q\to q}(x) + f^{\mathrm{real}}_{q\to q}(x) \tag{4.10a}$$

with the pieces related to other $f_{\underline{i\to j}}$ by

$$f^{\mathrm{virt}}_{q\to q}(x) = f_{\underline{q\to g}}(1-x) \quad \text{and} \quad f^{\mathrm{real}}_{q\to q}(x) = f_{\underline{q\to q}}(x) - f_{\underline{q\to g}}(1-x). \tag{4.10b}$$

From (4.7a) and (4.7d), the corresponding fits are

$$\begin{aligned} f^{\mathrm{real}}_{q\to q}(x) = -\tfrac{1}{6\pi}\ln x &- 1.65857 + 4.30633\,x - 0.41129\,x^2 + 1.02350\,x^3 \\ &+ 0.27637\,x^{1/2} - 1.16874\,x^{3/2} - 1.26259\,x^{5/2} \\ &+ 0.00549\,(1-x)^{1/2} + 0.34897\,(1-x)^{3/2} + 1.15890\,(1-x)^{5/2}, \end{aligned} \tag{4.11a}$$

$$\begin{aligned} f^{\mathrm{virt}}_{q\to q}(x) = \tfrac{1}{6\pi}\ln x &+ 2.21479 - 5.48428\,x + 0.90351\,x^2 - 1.63579\,x^3 \\ &- 0.24648\,x^{1/2} + 1.19122\,x^{3/2} + 2.42961\,x^{5/2} \\ &- 0.00727\,(1-x)^{1/2} - 0.50996\,(1-x)^{3/2} - 1.73122\,(1-x)^{5/2}. \end{aligned} \tag{4.11b}$$

4.3 Choice of renormalization scale

For democratic splittings, the natural choice of renormalization scale is given parametrically by the typical scale of relative transverse momenta in a leading-order splitting process, which is $\mu \sim (\hat{q}E)^{1/4}$ [13, 14, 16] in the case of an infinite medium considered here. Following ref.

[17], our canonical choice of renormalization scale (and the one used to preview results in table 1) is therefore

$$\mu \propto (\hat{q}_{\rm F} E)^{1/4}, \tag{4.12}$$

where E is the energy of the parent to the splitting. Our results for $\hat{q}$-insensitive quantities like $\sigma/\ell_{\rm stop}$ turn out not to depend on the exact choice of the proportionality constant in (4.12), as long as it is truly a constant.

However, as discussed in ref. [17], it is less clear what the best choice of renormalization scale should be when one of the daughters is soft. One might consider the total transverse momentum kick during a typical formation time $t_{\rm form}$, which would be

$$\mu \sim \Delta p_\perp \sim \sqrt{\hat{q} t_{\rm form}}. \tag{4.13}$$

For leading-order splittings, the formation time scale is determined by the frequency scale (2.4b) as $t_{\rm form} \sim 1/|\Omega_0|$. In the particular case of QCD, that's parametrically equivalent to

$$t_{\rm form} \sim \min\left(\sqrt{\frac{xE}{\hat{q}_{\rm F}}}, \sqrt{\frac{(1-x)E}{\hat{q}_{\rm F}}}\right) \sim \sqrt{\frac{x(1-x)E}{\hat{q}_{\rm F}}} \tag{4.14}$$

for both $q \to qg$ and $g \to {\rm Q}\bar{\rm Q}$, where x is the momentum fraction of either daughter.[23] So (4.13) suggests the choice

$$\mu \propto \big(x(1-x)\hat{q}_{\rm F} E\big)^{1/4}. \tag{4.15}$$

A different plausible choice for an x-dependent renormalization scale would be to choose the typical invariant mass of the two daughters of the splitting, which is equivalent to $2|\vec{p}_{\rm COM}|^2$ where $\pm\vec{p}_{\rm COM}$ are the 3-momenta of the daughters in their center-of-momentum frame. Ref. [17] showed that that choice is parametrically

$$\mu^2 \sim |\vec{p}_{\rm COM}|^2 \sim \frac{E}{t_{\rm form}}. \tag{4.16}$$

For QCD, this suggests the choice

$$\mu \propto \left(\frac{\hat{q}_{\rm F} E}{x(1-x)}\right)^{1/4} \tag{4.17}$$

It's useful to use these alternatives to get an idea of how sensitive our results are to such choices. Table 3 expands on the $N_{\rm f} \gg N_{\rm c} \gg 1$ QCD results of table 1 to compare results for all three choices of μ introduced above. Because our canonical choice (4.12) of renormalization scale μ happens to be the geometric mean of the other two, and rates (4.3) are only logarithmically dependent on the explicit value of μ, the results listed for $\mu \propto [x(1-x)\hat{q}_{\rm F} E]^{1/4}$ and $\mu \propto [\hat{q}_{\rm F} E/x(1-x)]^{1/4}$ symmetrically bracket (within round-off error) the results for our canonical choice $\mu \propto (\hat{q}_{\rm F} E)^{1/4}$. Following ref. [17], we therefore need only show one of the two alternatives in the future in order to convey the sensitivity of our results to these choices of renormalization scale.

[23] Eq. (4.14) is also parametrically the formation time for $g \to gg$, but that's irrelevant for $N_{\rm f} \gg N_{\rm c}$.

	overlap correction to $\sigma/\ell_{\text{stop}}$		
	$\mu \propto \big(\hat{q}E/x(1-x)\big)^{1/4}$	$\mu \propto (\hat{q}E)^{1/4}$	$\mu \propto \big(x(1-x)\hat{q}E\big)^{1/4}$
energy, g	$-0.70\% \times N_{\text{f}}\alpha_{\text{s}}$	$-0.40\% \times N_{\text{f}}\alpha_{\text{s}}$	$-0.11\% \times N_{\text{f}}\alpha_{\text{s}}$
energy, q	$-1.03\% \times N_{\text{f}}\alpha_{\text{s}}$	$-0.53\% \times N_{\text{f}}\alpha_{\text{s}}$	$-0.03\% \times N_{\text{f}}\alpha_{\text{s}}$
initial flavor, q	$+0.72\% \times N_{\text{f}}\alpha_{\text{s}}$	$+1.05\% \times N_{\text{f}}\alpha_{\text{s}}$	$+1.38\% \times N_{\text{f}}\alpha_{\text{s}}$

Table 3. The $N_{\text{f}} \gg N_{\text{c}} \gg 1$ QCD column of table 1 but here expanded to show the dependence on different plausible choices of renormalization scale. We have included an extra significant digit in our results to make clear that the values in the first and third columns of numbers symmetrically bracket those in the second column (within round-off error).

Though the ambiguity of how best to choose the renormalization scale introduces a significant *relative* uncertainty in the exact percentage size of overlap effects, as shown in table 3, the percentages remain very small for any reasonable size of $N_{\text{f}}\alpha_{\text{s}}$, and so our qualitative conclusion that $\hat{q}$-insensitive overlap effects are small is unaffected.

5 Numerical results for moments of shape functions

5.1 Initial-flavor deposition

Consider a shower initiated by a high-energy quark with energy E_0. As explained in the sections 1.2 and 2.4, in the large-N_{f} limit we may unambiguously follow the fate of that initial quark through the shower and so construct a statistically-averaged distribution, call it $\rho(z)$, for where that particular quark is eventually deposited in the medium. In the language of conserved quantities, this is equivalent to studying initial-flavor deposition since the chance that a pair-produced quark has the same flavor as the initial quark vanishes in the large-N_{f} limit. So we may view $\rho(z)$ as the deposition distribution of the particular quark flavor of the quark that initiated the shower.

In large-N_{f} QED, following the heir of the original electron also gave the charge deposition distribution. That's because the net rates $[d\Gamma/dx]_{\underline{e\to \text{E}}}$ and $[d\Gamma/dx]_{\underline{e\to \bar{\text{E}}}}$ happen to be equal in large-N_{f} QED, and so the E and $\bar{\text{E}}$ in overlapping $e \to e\gamma \to e\text{E}\bar{\text{E}}$ are produced with the same distribution of energy and so subsequently deposit charge in the exact same way (statistically) except for sign. Their contributions to total charge deposition therefore exactly cancel. Only the original electron, tracked by $[d\Gamma/dx]_{\underline{e\to e}}$, contributed to charge deposition. The situation in large-N_{f} QCD is different because $[d\Gamma/dx]_{\underline{q\to \text{Q}}}$ and $[d\Gamma/dx]_{\underline{q\to \bar{\text{Q}}}}$ are *not* equal.

For initial-flavor deposition, however, we need follow *only* the heir of the initial quark through the shower for large-N_{f} QCD as well as large-N_{f} QED, and so we only need the rate $[d\Gamma/dx]_{\underline{q\to q}}$. We can then carry over the formalism that was used for large-N_{f} QED charge deposition in refs. [15, 17]. A simple recursion relation was found for moments of the charge distribution, which we simply quote here after translating electrons and charge to quarks and

z^n	$\langle z^n\rangle_\rho^{\rm LO}$	$\delta\langle z^n\rangle_\rho$	
		$\mu=(\hat{q}_{\rm F}E)^{1/4}$	$\mu=\big(x(1-x)\hat{q}_{\rm F}E\big)^{1/4}$
	in units of ℓ_0^n		
$\langle z\rangle$	2.0402	-0.04523 $t_{\rm F}N_{\rm f}\alpha_{\rm s}$	-0.3665 $t_{\rm F}N_{\rm f}\alpha_{\rm s}$
$\langle z^2\rangle$	4.9333	-0.1864 $t_{\rm F}N_{\rm f}\alpha_{\rm s}$	-1.7299 $t_{\rm F}N_{\rm f}\alpha_{\rm s}$
$\langle z^3\rangle$	13.377	-0.6591 $t_{\rm F}N_{\rm f}\alpha_{\rm s}$	-6.9428 $t_{\rm F}N_{\rm f}\alpha_{\rm s}$
$\langle z^4\rangle$	39.559	-2.2706 $t_{\rm F}N_{\rm f}\alpha_{\rm s}$	-27.153 $t_{\rm F}N_{\rm f}\alpha_{\rm s}$

Table 4. Expansions (5.3) of moments $\langle z^n\rangle_\rho$ of the initial-flavor deposition distribution $\rho(z)$ for renormalization scale choices (4.12) and (4.15). The unit ℓ_0 is defined by (5.4), and $t_{\rm F}=\frac{1}{2}$ as in (2.11).

initial flavor:

$$\langle z^n\rangle_\rho = \frac{n\langle z^{n-1}\rangle_\rho}{\mathrm{Avg}_{\underline{q\to q}}[1-x^{n/2}]}\,, \tag{5.1a}$$

where

$$\mathrm{Avg}_{i\to j}[g(x)] \equiv \int_0^1 dx\,\left[\frac{d\Gamma}{dx}(E_0,x)\right]_{i\to j}^{\rm net} g(x). \tag{5.1b}$$

We then expand the relevant net rate as

$$\left[\frac{d\Gamma}{dx}(E_0,x)\right]_{\underline{q\to q}}^{\rm net} = \left[\frac{d\Gamma}{dx}(E_0,x)\right]_{\underline{q\to q}}^{\rm LO} + \left[\frac{d\Gamma}{dx}(E_0,x)\right]_{\underline{q\to q}}^{\rm NLO}, \tag{5.2}$$

similarly expand moments of the initial deposition distribution that we want to calculate as

$$\langle z^n\rangle_\rho \simeq \langle z^n\rangle_\rho^{\rm LO} + \delta\langle z^n\rangle_\rho\,, \tag{5.3}$$

and then expand the recursion relation (5.1a) into recursion relations for $\langle z^n\rangle_\rho^{\rm LO}$ and its NLO correction $\delta\langle z^n\rangle_\rho$. Details may be found in ref. [17].[24]

Computing leading-order moments and their NLO corrections due to overlapping formation times then simply involves using the recursion relation, using the LO rate (2.9a) and its NLO correction from (4.3) and (4.7a), and numerically calculating some integrals. Our results for $N_{\rm f}\gg N_{\rm c}\gg 1$ QCD are given in table 4 in units of ℓ_0^n where

$$\ell_0 \equiv \frac{1}{C_{\rm F}\alpha_{\rm s}}\sqrt{\frac{E_0}{\hat{q}_{\rm F}}}\,. \tag{5.4}$$

However, our interest is in $\hat{q}$-insensitive quantities like $\sigma/\ell_{\rm stop}$. Following refs. [13, 14, 17], we can more generally consider what we call the shape $S_\rho(Z)$ of the initial-flavor deposition

[24] See in particular section 5.3 of ref. [17].

quantity Q	$Q_\rho^{\rm LO}$	δQ_ρ	$\chi\alpha_{\rm s}$	δQ_ρ	$\chi\alpha_{\rm s}$
		$\mu \propto (\hat{q}E)^{1/4}$		$\mu \propto \big(x(1-x)\hat{q}E\big)^{1/4}$	
$\langle Z\rangle$	1				
$\langle Z^2\rangle^{1/2}$	1.0887	$0.0036\,t_{\rm F}N_{\rm f}\alpha_{\rm s}$	$0.0033\,t_{\rm F}N_{\rm f}\alpha_{\rm s}$	$0.0047\,t_{\rm F}N_{\rm f}\alpha_{\rm s}$	$0.0043\,t_{\rm F}N_{\rm f}\alpha_{\rm s}$
$\langle Z^3\rangle^{1/3}$	1.1636	$0.0067\,t_{\rm F}N_{\rm f}\alpha_{\rm s}$	$0.0057\,t_{\rm F}N_{\rm f}\alpha_{\rm s}$	$0.0077\,t_{\rm F}N_{\rm f}\alpha_{\rm s}$	$0.0066\,t_{\rm F}N_{\rm f}\alpha_{\rm s}$
$\langle Z^4\rangle^{1/4}$	1.2293	$0.0096\,t_{\rm F}N_{\rm f}\alpha_{\rm s}$	$0.0078\,t_{\rm F}N_{\rm f}\alpha_{\rm s}$	$0.0099\,t_{\rm F}N_{\rm f}\alpha_{\rm s}$	$0.0080\,t_{\rm F}N_{\rm f}\alpha_{\rm s}$
$\mu_{2,S}^{1/2}{=}k_{2,\rm S}^{1/2}{=}\sigma_S$	0.4304	$0.0090\,t_{\rm F}N_{\rm f}\alpha_{\rm s}$	$0.0210\,t_{\rm F}N_{\rm f}\alpha_{\rm s}$	$0.0119\,t_{\rm F}N_{\rm f}\alpha_{\rm s}$	$0.0276\,t_{\rm F}N_{\rm f}\alpha_{\rm s}$
$\mu_{3,S}^{1/3}{=}k_{3,\rm S}^{1/3}$	0.2691	$0.0177\,t_{\rm F}N_{\rm f}\alpha_{\rm s}$	$0.0658\,t_{\rm F}N_{\rm f}\alpha_{\rm s}$	$0.0032\,t_{\rm F}N_{\rm f}\alpha_{\rm s}$	$0.0118\,t_{\rm F}N_{\rm f}\alpha_{\rm s}$
$\mu_{4,S}^{1/4}$	0.5536	$0.0139\,t_{\rm F}N_{\rm f}\alpha_{\rm s}$	$0.0251\,t_{\rm F}N_{\rm f}\alpha_{\rm s}$	$0.0138\,t_{\rm F}N_{\rm f}\alpha_{\rm s}$	$0.0250\,t_{\rm F}N_{\rm f}\alpha_{\rm s}$
$(-k_{4,S})^{1/4}$	0.3086	$-0.0066\,t_{\rm F}N_{\rm f}\alpha_{\rm s}$	$-0.0214\,t_{\rm F}N_{\rm f}\alpha_{\rm s}$	$0.0169\,t_{\rm F}N_{\rm f}\alpha_{\rm s}$	$0.0547\,t_{\rm F}N_{\rm f}\alpha_{\rm s}$

Table 5. Expansions involving moments $\langle Z^n\rangle$, reduced moments $\mu_{n,S}$, and cumulants $k_{n,S}$ of the initial-flavor deposition shape function $S_\rho(Z)$, for renormalization scale choices (4.12) and (4.15). There are no NLO entries for $\langle Z\rangle$ because $\langle Z\rangle = 1$ and $\langle Z\rangle_{\rm LO} = 1$ by definition of $Z \equiv z/\langle z\rangle$. The last row gives $(-k_{4,S})^{1/4}$ instead of $k_{4,S}^{1/4}$ because the leading-order 4th cumulant $k_{4,S}^{\rm LO}$ turns out to be negative in this case.

distribution $\rho(z)$, defined by rescaling $\rho(z)$ to units where the stopping length and the area under the curve are both one. That is

$$S_\rho(Z) \equiv \ell_{\rm stop}^{(\rho)}\,\rho(Z\ell_{\rm stop}^{(\rho)}) \tag{5.5}$$

where Z is position in units of $\ell_{\rm stop}^{(\rho)} \equiv \langle z\rangle_\rho$. The shape and all of its moments are $\hat{q}$-insensitive and so good tests of the size of overlap corrections that cannot be absorbed into $\hat{q}$. The numerical values in table 4 can be used to compute the moments of S_ρ expanded to first order in NLO corrections. Results are tabulated in table 5 for moments $\langle Z^n\rangle$, reduced moments $\mu_{n,S} \equiv \big\langle (Z - \langle Z\rangle)^n\big\rangle$ and cumulants $k_{n,S}$ of the shape S_ρ. However, for the sake of comparing apples to apples, we have followed refs. [14, 17] by first converting all of these quantities into corresponding lengths: $\langle Z^n\rangle^{1/n}$, $\mu_{n,S}^{1/n}$, and $k_{n,S}^{1/n}$. For each such quantity Q, the table gives the LO value $Q_{\rm LO}$, the NLO correction δQ when expanded to first order, and the relative size of overlap corrections

$$\chi\alpha_{\rm s} \equiv \frac{\delta Q}{Q_{\rm LO}}\,. \tag{5.6}$$

The row for $\mu_2^{1/2}$, which is the width σ_S of the shape function, is the ratio $\sigma/\ell_{\rm stop}$ previewed in the introduction, where the "overlap correction" quoted there for $N_{\rm f}{\gg}N_{\rm c}{\gg}1$ QCD corresponds to the value of $\chi\alpha_{\rm s}$ here for $\mu \propto (\hat{q}E)^{1/4}$.

We put the factor of $C_{\rm F}$ into the definition (5.4), and wrote the δQ entries of the tables in terms of $t_{\rm F}N_{\rm f}\alpha_{\rm s}$ instead of just $N_{\rm f}\alpha_{\rm s}$, so that the simple overall color factors are made explicit.

This means that the only difference between the explicit numbers in the table here and those in the corresponding table of ref. [17] for large-N_f QED is the difference in 3-body and 4-body frequencies Ω and normal modes, arising from the different nature of interactions with the medium and their correlations for $N_f \gg N_c \gg 1$ QCD vs. large-N_f QED.[25] That difference arises because (i) gluons have color and (ii) the correlations of medium interactions were forced to be "planar" in large-N_c QCD, in the sense of figs. 10 and 11.

The conclusion to take away from the $\chi\alpha_s$ columns of table 5 is that the overlap corrections reported for σ/ℓ_{stop} in table 1 are not merely isolated examples of very small overlap corrections for a $\hat{q}$-insensitive quantity in $N_f \gg N_c \gg 1$ QCD. All of the moments in table 5 have small overlap corrections for reasonable values of $N_f\alpha_s$.

We content ourselves with having tested the size of overlap corrections to various moments of $S_\rho(Z)$. At the cost of significantly more numerical effort, one could more generally compute the overlap corrections to the full functional form of $S_\rho(Z)$, as was done by refs. [13, 14] for the energy deposition distribution in N_f=0, large-N_c QCD. For now, we think that checking the moments is an adequate test.

5.2 Energy deposition

Ref. [17] derived recursion relations for moments of large-N_f energy deposition distributions,[26] which we also simply quote here after translating electrons and photons to quarks and gluons. Let $\epsilon_i(z)$ be the energy deposition distribution for a shower initiated by a particle of type $i = q$ or g, and let $\langle z^n \rangle_{\epsilon,i}$ represent the moments of that distribution. Then the large-N_f recursion relations are

$$\langle z^n \rangle_{\epsilon,q} = \frac{n M_{(n),gg}}{\det M_{(n)}} \langle z^{n-1} \rangle_{\epsilon,q} \tag{5.7a}$$

for quark-initiated showers and a dependent result

$$\langle z^n \rangle_{\epsilon,g} = -\frac{M_{(n),gq}}{M_{(n),gg}} \langle z^n \rangle_{\epsilon,q} \tag{5.7b}$$

for moments of gluon-initiated showers. Above, the constants $M_{(n)}$ are defined by

$$\begin{aligned} M_{(n)} &\equiv \begin{pmatrix} M_{(n),qq} & M_{(n),qg} \\ M_{(n),gq} & M_{(n),gg} \end{pmatrix} \\ &= \mathrm{Avg}_{q\to q \text{ or } \bar{q}} \begin{pmatrix} x - x^{1+\frac{n}{2}} & 0 \\ 0 & 0 \end{pmatrix} + \mathrm{Avg}_{\underline{q\to g}} \begin{pmatrix} x & -x^{1+\frac{n}{2}} \\ 0 & 0 \end{pmatrix} + \mathrm{Avg}_{g\to q \text{ or } \bar{q}} \begin{pmatrix} 0 & 0 \\ -x^{1+\frac{n}{2}} & x \end{pmatrix}, \end{aligned} \tag{5.8}$$

[25] There is also another way to put this. Imagine that the quarks all had the same electric charge, were splitting via gluon bremsstrahlung and quark pair production, but were getting their kicks from a QED medium instead of a QCD medium. The results for $\chi\alpha_s$ would be identical to the large-N_f QED tables of ref. [17] except for replacing $N_f\alpha$ there by $t_F N_f \alpha_s$ and ℓ_0 there by the definition (5.4) of ℓ_0 here.

[26] Specifically, see section 6.3 of ref. [17].

z^n	$\langle z^n\rangle^{\rm LO}_{\epsilon,i}$	$\delta\langle z^n\rangle_{\epsilon,i}$	
		$\mu = (\hat{q}_{\rm F}E)^{1/4}$	$\mu = \big(x(1{-}x)\hat{q}_{\rm F}E\big)^{1/4}$
		in units of ℓ_0^n	
quark initiated ($i = q$)**:**			
$\langle z\rangle$	1.3703	0.0029 $t_{\rm F}N_{\rm f}\alpha_{\rm s}$	-0.2232 $t_{\rm F}N_{\rm f}\alpha_{\rm s}$
$\langle z^2\rangle$	2.4734	-0.0021 $t_{\rm F}N_{\rm f}\alpha_{\rm s}$	-0.8066 $t_{\rm F}N_{\rm f}\alpha_{\rm s}$
$\langle z^3\rangle$	5.3271	-0.0201 $t_{\rm F}N_{\rm f}\alpha_{\rm s}$	-2.6085 $t_{\rm F}N_{\rm f}\alpha_{\rm s}$
$\langle z^4\rangle$	13.033	-0.0676 $t_{\rm F}N_{\rm f}\alpha_{\rm s}$	-8.5177 $t_{\rm F}N_{\rm f}\alpha_{\rm s}$
gluon initiated ($i = g$)**:**			
$\langle z\rangle$	1.2118	-0.0041 $t_{\rm F}N_{\rm f}\alpha_{\rm s}$	-0.1931 $t_{\rm F}N_{\rm f}\alpha_{\rm s}$
$\langle z^2\rangle$	2.0059	-0.0224 $t_{\rm F}N_{\rm f}\alpha_{\rm s}$	-0.6415 $t_{\rm F}N_{\rm f}\alpha_{\rm s}$
$\langle z^3\rangle$	4.0377	-0.0726 $t_{\rm F}N_{\rm f}\alpha_{\rm s}$	-1.9424 $t_{\rm F}N_{\rm f}\alpha_{\rm s}$
$\langle z^4\rangle$	9.3382	-0.2115 $t_{\rm F}N_{\rm f}\alpha_{\rm s}$	-6.0032 $t_{\rm F}N_{\rm f}\alpha_{\rm s}$

Table 6. Like table 4 but showing moments $\langle z^n\rangle$ for energy deposition instead of quark-initiated initial-flavor deposition. The unit ℓ_0 is defined by (5.4), and $t_{\rm F} = \frac{1}{2}$ as in (2.11).

where

$$\left[\frac{d\Gamma}{dx}\right]^{\rm net}_{q\to q\,\text{or}\,\bar{q}} \equiv \left[\frac{d\Gamma}{dx}\right]^{\rm net}_{\underline{q\to q}} + \left[\frac{d\Gamma}{dx}\right]^{\rm net}_{\underline{q\to \rm Q}} + \left[\frac{d\Gamma}{dx}\right]^{\rm net}_{\underline{q\to \bar{\rm Q}}}\,, \tag{5.9a}$$

$$\left[\frac{d\Gamma}{dx}\right]^{\rm net}_{g\to q\,\text{or}\,\bar{q}} \equiv \left[\frac{d\Gamma}{dx}\right]^{\rm net}_{\underline{g\to \rm Q}} + \left[\frac{d\Gamma}{dx}\right]^{\rm net}_{\underline{g\to \bar{\rm Q}}} \tag{5.9b}$$

are defined as the sum of net rates to produce *any* type of quark or anti-quark daughter from the specified type of parent. One then expands the net rates $[d\Gamma/dx]^{\rm net}_{\underline{i\to j}}$ and moments $\langle z^n\rangle_{\epsilon,i}$ as LO+NLO, similar to (5.2) and (5.3), and then correspondingly expands the recursion relations (5.7).

Our results for moments of $\epsilon_i(z)$ are given in table 6. Using those, we then extract the various types of moments, shown in table 7, of the corresponding $\hat{q}$-insensitive shape functions

$$S_{\epsilon,i}(Z) \equiv \frac{\ell^{(\epsilon,i)}_{\rm stop}}{E_0}\,\epsilon_i(Z\ell^{(\epsilon,i)}_{\rm stop}), \tag{5.10}$$

where $\ell^{(\epsilon,i)}_{\rm stop} \equiv \langle z\rangle_{\epsilon,i}$ and E_0 is the energy of the particle that initiated the shower. Once again, all of the moments in table 7 have small overlap corrections for reasonable values of $N_{\rm f}\alpha_{\rm s}$.

quantity Q	$Q^{\rm LO}_{\epsilon,i}$	$\delta Q_{\epsilon,i}$	$\chi\alpha_{\rm s}$	$\delta Q_{\epsilon,i}$	$\chi\alpha_{\rm s}$
		$\mu \propto (\hat{q}E)^{1/4}$		$\mu \propto \big(x(1{-}x)\hat{q}E\big)^{1/4}$	
quark initiated ($i = q$)**:**					
$\langle Z\rangle$	1				
$\langle Z^2\rangle^{1/2}$	1.1477	$-0.0029\,t_{\rm F}N_{\rm f}\alpha_{\rm s}$	$-0.0026\,t_{\rm F}N_{\rm f}\alpha_{\rm s}$	$-0.0002\,t_{\rm F}N_{\rm f}\alpha_{\rm s}$	$-0.0002\,t_{\rm F}N_{\rm f}\alpha_{\rm s}$
$\langle Z^3\rangle^{1/3}$	1.2746	$-0.0043\,t_{\rm F}N_{\rm f}\alpha_{\rm s}$	$-0.0034\,t_{\rm F}N_{\rm f}\alpha_{\rm s}$	$-0.0004\,t_{\rm F}N_{\rm f}\alpha_{\rm s}$	$-0.0003\,t_{\rm F}N_{\rm f}\alpha_{\rm s}$
$\langle Z^4\rangle^{1/4}$	1.3866	$-0.0048\,t_{\rm F}N_{\rm f}\alpha_{\rm s}$	$-0.0034\,t_{\rm F}N_{\rm f}\alpha_{\rm s}$	$-0.0007\,t_{\rm F}N_{\rm f}\alpha_{\rm s}$	$-0.0005\,t_{\rm F}N_{\rm f}\alpha_{\rm s}$
$\mu_{2,S}^{1/2}{=}k_{2,\rm S}^{1/2}{=}\sigma_S$	0.5633	$-0.0060\,t_{\rm F}N_{\rm f}\alpha_{\rm s}$	$-0.0106\,t_{\rm F}N_{\rm f}\alpha_{\rm s}$	$-0.0004\,t_{\rm F}N_{\rm f}\alpha_{\rm s}$	$-0.0007\,t_{\rm F}N_{\rm f}\alpha_{\rm s}$
$\mu_{3,S}^{1/3}{=}k_{3,\rm S}^{1/3}$	0.4913	$-0.0011\,t_{\rm F}N_{\rm f}\alpha_{\rm s}$	$-0.0023\,t_{\rm F}N_{\rm f}\alpha_{\rm s}$	$-0.0010\,t_{\rm F}N_{\rm f}\alpha_{\rm s}$	$-0.0021\,t_{\rm F}N_{\rm f}\alpha_{\rm s}$
$\mu_{4,S}^{1/4}$	0.7513	$-0.0041\,t_{\rm F}N_{\rm f}\alpha_{\rm s}$	$-0.0055\,t_{\rm F}N_{\rm f}\alpha_{\rm s}$	$-0.0010\,t_{\rm F}N_{\rm f}\alpha_{\rm s}$	$-0.0013\,t_{\rm F}N_{\rm f}\alpha_{\rm s}$
$k_{4,S}^{1/4}$	0.3584	$0.0320\,t_{\rm F}N_{\rm f}\alpha_{\rm s}$	$0.0892\,t_{\rm F}N_{\rm f}\alpha_{\rm s}$	$-0.0048\,t_{\rm F}N_{\rm f}\alpha_{\rm s}$	$-0.0135\,t_{\rm F}N_{\rm f}\alpha_{\rm s}$
gluon initiated ($i = g$)**:**					
$\langle Z\rangle$	1				
$\langle Z^2\rangle^{1/2}$	1.1687	$-0.0025\,t_{\rm F}N_{\rm f}\alpha_{\rm s}$	$-0.0022\,t_{\rm F}N_{\rm f}\alpha_{\rm s}$	$-0.0007\,t_{\rm F}N_{\rm f}\alpha_{\rm s}$	$-0.0006\,t_{\rm F}N_{\rm f}\alpha_{\rm s}$
$\langle Z^3\rangle^{1/3}$	1.3140	$-0.0034\,t_{\rm F}N_{\rm f}\alpha_{\rm s}$	$-0.0026\,t_{\rm F}N_{\rm f}\alpha_{\rm s}$	$-0.0013\,t_{\rm F}N_{\rm f}\alpha_{\rm s}$	$-0.0010\,t_{\rm F}N_{\rm f}\alpha_{\rm s}$
$\langle Z^4\rangle^{1/4}$	1.4425	$-0.0033\,t_{\rm F}N_{\rm f}\alpha_{\rm s}$	$-0.0023\,t_{\rm F}N_{\rm f}\alpha_{\rm s}$	$-0.0020\,t_{\rm F}N_{\rm f}\alpha_{\rm s}$	$-0.0014\,t_{\rm F}N_{\rm f}\alpha_{\rm s}$
$\mu_{2,S}^{1/2}{=}k_{2,\rm S}^{1/2}{=}\sigma_S$	0.6049	$-0.0049\,t_{\rm F}N_{\rm f}\alpha_{\rm s}$	$-0.0081\,t_{\rm F}N_{\rm f}\alpha_{\rm s}$	$-0.0013\,t_{\rm F}N_{\rm f}\alpha_{\rm s}$	$-0.0021\,t_{\rm F}N_{\rm f}\alpha_{\rm s}$
$\mu_{3,S}^{1/3}{=}k_{3,\rm S}^{1/3}$	0.5550	$0.0001\,t_{\rm F}N_{\rm f}\alpha_{\rm s}$	$0.0003\,t_{\rm F}N_{\rm f}\alpha_{\rm s}$	$-0.0024\,t_{\rm F}N_{\rm f}\alpha_{\rm s}$	$-0.0043\,t_{\rm F}N_{\rm f}\alpha_{\rm s}$
$\mu_{4,S}^{1/4}$	0.8192	$-0.0019\,t_{\rm F}N_{\rm f}\alpha_{\rm s}$	$-0.0023\,t_{\rm F}N_{\rm f}\alpha_{\rm s}$	$-0.0025\,t_{\rm F}N_{\rm f}\alpha_{\rm s}$	$-0.0031\,t_{\rm F}N_{\rm f}\alpha_{\rm s}$
$k_{4,S}^{1/4}$	0.4697	$0.0213\,t_{\rm F}N_{\rm f}\alpha_{\rm s}$	$0.0454\,t_{\rm F}N_{\rm f}\alpha_{\rm s}$	$-0.0052\,t_{\rm F}N_{\rm f}\alpha_{\rm s}$	$-0.0110\,t_{\rm F}N_{\rm f}\alpha_{\rm s}$

Table 7. Expansions of moments $\langle Z^n\rangle$, reduced moments $\mu_{n,S}$, and cumulants $k_{n,S}$ of the energy deposition shape functions $S_{\epsilon,q}(Z)$ and $S_{\epsilon,g}(Z)$ for quark-initiated and gluon-initiated showers, respectively. Like table 5 but for energy deposition instead of quark-initiated initial-flavor deposition. (Unlike table 5, the leading-order 4th cumulant $k_{4,S}^{\rm LO}$ is positive here.)

6 IR sensitivity of QCD fermion number deposition

We will now explore what goes wrong if we try to use the same formalism to explore quark-number stopping instead of initial-flavor or energy stopping. The same issue would also arise for electric charge stopping in QCD. (Indeed, if all quarks had the same electric charge, then electric charge would simply be directly proportional to quark number.)

6.1 Recursion equation for moments

In large-N_f QED, the contribution to electron-number (or charge) deposition from pair-produced electrons and positrons canceled. Because $[d\Gamma/dx]_{\underline{q\to \mathrm{Q}}} \neq [d\Gamma/dx]_{\underline{q\to \bar{\mathrm{Q}}}}$ in large-N_f QCD, the analysis of quark-number stopping cannot just follow the fate of the initiating quark using $[d\Gamma/dx]_{\underline{q\to q}}$ but must also account for how pair-produced quarks and anti-quarks deposit *their* quark number. The derivation needed is similar but slightly different from those made in ref. [17] that resulted in the recursion relations quoted in our (5.1a) and (5.7). So we will take time here to explain the differences.

Let $\phi_q(E_0, z)$ represent the quark-number deposition distribution from a shower initiated by a quark with energy E_0. By charge conjugation, the corresponding distribution for an anti-quark initiated shower would be

$$\phi_{\bar{q}}(E_0, z) = -\phi_q(E_0, z). \tag{6.1}$$

Also by charge conjugation, $\phi_g(E_0, z) = 0$. Following the logic of refs. [15, 17],[27] our starting equation is

$$\begin{aligned}\phi_q(E, z+\Delta z) = [1 - \Gamma_q(E)\,\Delta z]\,\phi_q(E,z) + \int_0^1 dx\,\left[\frac{d\Gamma}{dx}(E,x)\right]^{\mathrm{net}}_{\underline{q\to q}} \Delta z\,\phi_q(xE,z) \\ + \int_0^1 dx\,\left[\frac{d\Gamma}{dx}(E,x)\right]^{\mathrm{net}}_{\underline{q\to \mathrm{Q}}} \Delta z\,\phi_q(xE,z) + \int_0^1 dx\,\left[\frac{d\Gamma}{dx}(E,x)\right]^{\mathrm{net}}_{\underline{q\to \bar{\mathrm{Q}}}} \Delta z\,\phi_{\bar{q}}(xE,z)\end{aligned} \tag{6.2}$$

in the limit of small Δz. The first term accounts for the chance that the quark does not split in the first Δz of distance, and the remaining terms sum up the contributions from each daughter if the original quark did split in the first Δz of distance. Rearranging terms, taking the limit $\Delta z \to 0$, and using (6.1) gives an integro-differential equation for ϕ_q,

$$\begin{aligned}\frac{\partial \phi_q(E,z)}{\partial z} = -\Gamma_q(E)\,\phi_q(E,z) + \int_0^1 dx\,\left[\frac{d\Gamma}{dx}(E,x)\right]^{\mathrm{net}}_{\underline{q\to q}} \phi_q(xE,z) \\ + \int_0^1 dx\,\left[\frac{d\Gamma}{dx}(E,x)\right]^{\mathrm{net}}_{\underline{q\to \mathrm{Q}}} \phi_q(xE,z) - \int_0^1 dx\,\left[\frac{d\Gamma}{dx}(E,x)\right]^{\mathrm{net}}_{\underline{q\to \bar{\mathrm{Q}}}} \phi_q(xE,z).\end{aligned} \tag{6.3}$$

Now rewrite the total quark splitting rate (including NLO corrections) as[28]

$$\Gamma_q = \int_0^1 dx\,\left[\frac{d\Gamma}{dx}\right]^{\mathrm{net}}_{\underline{q\to q}} \tag{6.4}$$

[27] See in particular sections 5.1–5.3 and 6.1 of ref. [17].

[28] The validity of eq. (6.4) depends subtly on the fact that all the daughters of our LO+NLO quark splitting processes $q\to qg$ and $q\to q\mathrm{Q}\bar{\mathrm{Q}}$ are distinguishable in the large-N_f limit. Otherwise the relations would be complicated by identical-particle final state factors such as those appearing in the analysis of $g\to gg$ and $g\to ggg$ in refs. [13, 14].

to put (6.3) into the form

$$\frac{\partial\phi_q(E,z)}{\partial z} = \int_0^1 dx \left[\frac{d\Gamma}{dx}(E,x)\right]^{\text{net}}_{\underline{q\to q}} \left[\phi_q(xE,z) - \phi_q(E,z)\right] + \int_0^1 dx \left(\left[\frac{d\Gamma}{dx}(E,x)\right]^{\text{net}}_{\underline{q\to \mathrm{Q}}} - \left[\frac{d\Gamma}{dx}(E,x)\right]^{\text{net}}_{\underline{q\to \bar{\mathrm{Q}}}}\right)\phi_q(xE,z). \quad (6.5)$$

Following arguments similar to ref. [17], we may use the fact that the LO and NLO rates scale with energy as $\sqrt{\hat{q}/E}$ to introduce rescaled variables $d\tilde{\Gamma}$, $\tilde{z}$, and $\tilde{\rho}$ by[29]

$$\left[\frac{d\Gamma}{dx}(E,x)\right]^{\text{net}}_{\underline{i\to j}} = E^{-1/2}\left[\frac{d\tilde{\Gamma}}{dx}(x)\right]^{\text{net}}_{\underline{i\to j}}, \qquad z = E^{1/2}\tilde{z}, \qquad \phi_q(E,z) = E^{-1/2}\,\tilde{\phi}_q(\tilde{z}) \quad (6.6)$$

to get

$$\frac{\partial\tilde{\phi}_q(\tilde{z})}{\partial\tilde{z}} = \int_0^1 dx \left[\frac{d\tilde{\Gamma}}{dx}(x)\right]^{\text{net}}_{\underline{q\to q}} \left[x^{-1/2}\tilde{\phi}_q(x^{-1/2}\tilde{z}) - \tilde{\phi}_q(\tilde{z})\right] + \int_0^1 dx \left(\left[\frac{d\tilde{\Gamma}}{dx}(x)\right]^{\text{net}}_{\underline{q\to \mathrm{Q}}} - \left[\frac{d\tilde{\Gamma}}{dx}(x)\right]^{\text{net}}_{\underline{q\to \bar{\mathrm{Q}}}}\right) x^{-1/2}\tilde{\phi}_q(x^{-1/2}\tilde{z}). \quad (6.7)$$

Then we may convert the scaled variables back to the original unscaled variables to get a simple equation for the desired quark-number deposition distribution $\phi_q(z) \equiv \phi_q(E_0,z)$ of the shower:

$$\frac{\partial\phi_q(z)}{\partial z} = \int_0^1 dx \left[\frac{d\Gamma}{dx}(E_0,x)\right]^{\text{net}}_{\underline{q\to q}} \left[x^{-1/2}\phi_q(x^{-1/2}z) - \phi_q(z)\right] + \int_0^1 dx \left(\left[\frac{d\Gamma}{dx}(E_0,x)\right]^{\text{net}}_{\underline{q\to \mathrm{Q}}} - \left[\frac{d\Gamma}{dx}(E_0,x)\right]^{\text{net}}_{\underline{q\to \bar{\mathrm{Q}}}}\right) x^{-1/2}\phi_q(x^{-1/2}z). \quad (6.8)$$

To get a recursion relation for the moments, multiply both sides of (6.8) by z^n and integrate over z to get

$$-n\langle z^{n-1}\rangle_\phi = \int_0^1 dx \left[\frac{d\Gamma}{dx}(E_0,x)\right]^{\text{net}}_{\underline{q\to q}} \left[x^{n/2}\langle z^n\rangle_\phi - \langle z^n\rangle_\phi\right] + \int_0^1 dx \left(\left[\frac{d\Gamma}{dx}(E_0,x)\right]^{\text{net}}_{\underline{q\to \mathrm{Q}}} - \left[\frac{d\Gamma}{dx}(E_0,x)\right]^{\text{net}}_{\underline{q\to \bar{\mathrm{Q}}}}\right) x^{n/2}\langle z^n\rangle_\phi\,, \quad (6.9)$$

which may be reorganized algebraically into

$$\langle z^n\rangle_\phi = \frac{n\langle z^{n-1}\rangle_\phi}{\mathcal{M}_n} \quad (6.10a)$$

[29] This is the same rescaling as eq. (5.4) of ref. [17].

where the constants $\mathcal{M}_n$ are given by

$$\mathcal{M}_n = \mathrm{Avg}_{\underline{q\to q}}[1-x^{n/2}] + \big\{\mathrm{Avg}_{\underline{q\to\bar{\mathrm{Q}}}}[x^{n/2}] - \mathrm{Avg}_{\underline{q\to\mathrm{Q}}}[x^{n/2}]\big\}. \tag{6.10b}$$

Note that if $[d\Gamma/dx]^{\mathrm{net}}_{\underline{q\to\mathrm{Q}}}$ and $[d\Gamma/dx]^{\mathrm{net}}_{\underline{q\to\bar{\mathrm{Q}}}}$ were equal, this would reduce to exactly the same recursion relation (5.1a) as for the initial-flavor distribution $\rho(z)$.

6.2 IR logarithm

6.2.1 Divergence in $\hat{q}$ approximation

Both the LO and NLO contributions to the net rate $[d\Gamma/dx_q]^{\mathrm{net}}_{\underline{q\to q}}$ have power-law dependence $x^{-1/2}$ as $x\to 0$ and $(1-x)^{-3/2}$ as $x\to 1$. [See eqs. (2.9a) and (4.1a) for the LO rate and eqs. (4.3), (4.4a), (4.5a) and (4.7a) for the NLO correction.] This behavior is mild enough that the integral over x in the first term of (6.10b) converges, which is why we had no issues with our numerical evaluations of moments of initial-flavor deposition in section 5.1. Parametrically, the size of the first term of (6.10b) is

$$\mathrm{Avg}_{\underline{q\to q}}[1-x^{n/2}] \sim \frac{1}{\ell_0}, \tag{6.11}$$

where ℓ_0 is the parametric scale for the length of the shower given by (5.4).

But now look at the remaining terms of (6.10b). The $q\to\mathrm{Q}$ and $q\to\bar{\mathrm{Q}}$ net rates do not have any LO contribution, and so these rates are given by $[d\Gamma/dx]^{\mathrm{NLO}}_{\underline{q\to\mathrm{Q}}}$ and $[d\Gamma/dx]^{\mathrm{NLO}}_{\underline{q\to\bar{\mathrm{Q}}}}$. Everything is okay for $x\to 1$ because neither rate diverges in that limit. [See eq. (4.4b) in particular.] But there is a problem for $x\to 0$. In that limit, eqs. (4.7b) and (4.7c) give

$$f_{\underline{q\to\mathrm{Q}}}(x) \to 0.6725, \qquad f_{\underline{q\to\bar{\mathrm{Q}}}}(x) \to 0.6774, \tag{6.12}$$

and so the difference $f_{\underline{q\to\bar{\mathrm{Q}}}}(x) - f_{\underline{q\to\mathrm{Q}}}(x) \to 0.0049$ is small but non-zero as $x\to 0$. Eqs. (4.3) and (4.4b) then give that the corresponding difference in net rates scales as

$$\left[\frac{d\Gamma}{dx}\right]^{\mathrm{NLO}}_{\underline{q\to\bar{\mathrm{Q}}}} - \left[\frac{d\Gamma}{dx}\right]^{\mathrm{NLO}}_{\underline{q\to\mathrm{Q}}} \sim x^{-3/2}. \tag{6.13}$$

That means that the

$$\big\{\mathrm{Avg}_{\underline{q\to\bar{\mathrm{Q}}}}[x^{n/2}] - \mathrm{Avg}_{\underline{q\to\mathrm{Q}}}[x^{n/2}]\big\} = \int_0^1 dx \left(\left[\frac{d\Gamma}{dx}\right]^{\mathrm{NLO}}_{\underline{q\to\bar{\mathrm{Q}}}} - \left[\frac{d\Gamma}{dx}\right]^{\mathrm{NLO}}_{\underline{q\to\mathrm{Q}}}\right) x^{n/2} \tag{6.14}$$

contribution to (6.10b) is convergent for $n > 1$ but logarithmically IR divergent for $n = 1$. Parametrically,

$$\big\{\mathrm{Avg}_{\underline{q\to\bar{\mathrm{Q}}}}[x^{n/2}] - \mathrm{Avg}_{\underline{q\to\mathrm{Q}}}[x^{n/2}]\big\} \sim \frac{1}{\ell_0} \times \begin{cases} N_{\mathrm{f}}\alpha_{\mathrm{s}} \times (\text{IR log divergence}), & n{=}1; \\ N_{\mathrm{f}}\alpha_{\mathrm{s}}, & n{>}1, \end{cases} \tag{6.15}$$

where the factor of $N_f\alpha_s$ appears because the effect only arises from *overlapping* $q \to qg \to q\mathrm{Q}\bar{\mathrm{Q}}$, which is NLO.[30] Compare to (6.11).

6.2.2 IR scale

The logarithmic IR divergence is a consequence of the non-canceling $x^{-3/2}$ small-x behavior of the net rates for $q{\to}\mathrm{Q}$ and $q{\to}\bar{\mathrm{Q}}$. This $x^{-3/2}$ behavior also has the consequence that the total rate for overlapping $q \to qg \to q\mathrm{Q}\bar{\mathrm{Q}}$, which may be written as

$$\Gamma_{q\to q\mathrm{Q}\bar{\mathrm{Q}}} = \int_0^1 dx_{\mathrm{Q}} \left[\frac{d\Gamma}{dx_{\mathrm{Q}}}\right]^{\mathrm{net}}_{\underline{q\to\mathrm{Q}}} , \tag{6.16}$$

is *power-law* infrared divergent. That's a common situation in the context of the LPM effect for QCD in the $\hat{q}$ approximation. As an example, consider the total LO rate for bremsstrahlung,

$$\Gamma^{\mathrm{LO}}_{q\to qg} = \int_0^1 dx_g \left[\frac{d\Gamma}{dx_g}\right]^{\mathrm{LO}}_{q\to qg} , \tag{6.17}$$

The integrand behaves like $x_g^{-3/2} = (1{-}x_q)^{-3/2}$, and so integration gives a power-law soft-gluon divergence for the total LO rate as opposed to the more familiar logarithmic infrared divergences in the absence of the LPM effect. That power-law divergence is closely related to the one for (6.16) since a soft gluon in $q \to qg \to q\mathrm{Q}\bar{\mathrm{Q}}$ produces a soft Q and soft $\bar{\mathrm{Q}}$. The $x_g^{-3/2}$ behavior of $q \to qg$ arises because in QCD the formation time (4.14) for a bremsstrahlung gluon shrinks as the gluon becomes softer, and so there is less LPM suppression of softer gluon bremsstrahlung. This trend continues until the gluon is so soft that the formation time becomes less than the mean free time τ_0 between collisions with the medium, at which point the multiple-scattering ($\hat{q}$) approximation used throughout this paper breaks down, and the $x_g^{-3/2}$ softens. Parametrically, this takes place at x_g of order what we will call[31]

$$x_{\mathrm{IR}} \sim \frac{\hat{q}\tau_0^2}{E} , \tag{6.18a}$$

which in the specific case of a quark-gluon plasma would be[32]

$$x_{\mathrm{IR}} \sim \frac{T}{E} . \tag{6.18b}$$

The softening of the IR divergence for $x \ll x_{\mathrm{IR}}$ will cut-off the logarithmic divergence of (6.14) for $n = 1$, resolving (6.15) as

$$\left\{\mathrm{Avg}_{\underline{q\to\bar{\mathrm{Q}}}}[x^{n/2}] - \mathrm{Avg}_{\underline{q\to\mathrm{Q}}}[x^{n/2}]\right\} \sim \frac{1}{\ell_0} \times \begin{cases} N_f\alpha_s \ln(1/x_{\mathrm{IR}}), & n{=}1; \\ N_f\alpha_s, & n{>}1. \end{cases} \tag{6.18c}$$

[30] If $q \to qg$ is instead followed by *non*-overlapping $g \to \mathrm{Q}\bar{\mathrm{Q}}$, then *that* contribution of pair-produced quarks to quark-number deposition will average to zero because, as explained earlier, $\phi_g(E,z) = 0$ by charge conjugation.

[31] The IR cut-off on x was called δ in ref. [24].

[32] Medium-induced masses of quarks and gluons also become important at roughly the same scale, and they also cut off divergences in splitting rates.

Infrared sensitivity means that, with our $\hat{q}$-based NLO rates, we cannot compute the NLO correction to quark-number deposition to better than leading-log order, which is why we summarized the case of quark-number deposition as IR-unsafe in table 1. But also, for large enough energy, $N_{\rm f}\alpha_{\rm s}\ln(1/x_{\rm IR})$ may no longer be small even for small $N_{\rm f}\alpha_{\rm s}$. In that case, the NLO effect (6.18c) will no longer be small compared to the LO result (6.11) for $\mathcal{M}_1$. Then one may wonder about the uncalculated NNLO correction and so forth, which is another complication of IR-unsafe quantities.

Ultimately, the difference between quark-number deposition and energy deposition is that softer particles carry less energy and so contribute less to determining where the shower's energy stops. In contrast, softer quarks carry just as much quark number as harder ones, and so the details of how even arbitrarily soft quarks stop may significantly affect where (on average) overall quark number is deposited. We give a qualitative picture of why this happens in appendix C. The reason that QCD initial-flavor deposition avoided this problem is special to the large-$N_{\rm f}$ limit because pair-produced quarks (soft or otherwise) do not carry the flavor of the initial quark.

6.3 What is responsible for $[d\Gamma/dx]^{\rm net}_{q\to \rm Q} \neq [d\Gamma/dx]^{\rm net}_{q\to\bar{\rm Q}}$ as $x\to 0$?

The IR sensitivity of quark number stopping arose from the difference of $[d\Gamma/dx]_{q\to\rm Q}$ and $[d\Gamma/dx]_{q\to\bar{\rm Q}}$ and from its persistence as $x\to 0$. In contrast, in ref. [17] we found that $[d\Gamma/dx]_{\underline{e\to \rm E}} = [d\Gamma/dx]_{\underline{e\to\bar{\rm E}}}$, which was a consequence of invariance of the unintegrated rate

$$\left[\Delta\,\frac{d\Gamma}{dx_e\,dx_{\rm E}}\right]_{e\to e{\rm E}\bar{\rm E}} \tag{6.19}$$

under exchange of the values

$$x_{\rm E} \leftrightarrow x_{\bar{\rm E}} = 1-x_e-x_{\rm E}. \tag{6.20}$$

We were unable to articulate a simple symmetry or other high-level explanation expressible in a few sentences, but we did give a more involved, lower-level analysis of how invariance under (6.20) arose in the calculation of the $e\to e{\rm E}\bar{\rm E}$ rate.[33] For the $N_{\rm f}\gg N_{\rm c}\gg 1$ QCD case, we may similarly examine the behavior of the unintegrated rate $[\Delta\,d\Gamma/dx_q\,dx_{\rm Q}]_{q\to q{\rm Q}\bar{\rm Q}}$ under

$$x_{\rm Q} \leftrightarrow x_{\bar{\rm Q}} = 1-x_q-x_{\rm Q}. \tag{6.21}$$

There is no invariance, else the net rates would have been equal. But the lack of IR-safety for quark number deposition depends specifically on divergences in the limits where $x_{\rm Q}$ or $x_{\bar{\rm Q}}$ are small. And when $x_{\rm Q}$ is small, the IR divergence of the net rate $[d\Gamma/dx]^{\rm net}_{\underline{q\to\rm Q}}$ comes from the limit of soft gluon emission in overlapping $q\to qg\to q{\rm Q}\bar{\rm Q}$, in which case $x_{\bar{\rm Q}}$ is also comparably small. In that limit where

$$x_{\rm Q}\sim x_{\bar{\rm Q}}\to 0, \tag{6.22}$$

[33] See Appendix A of ref. [17].

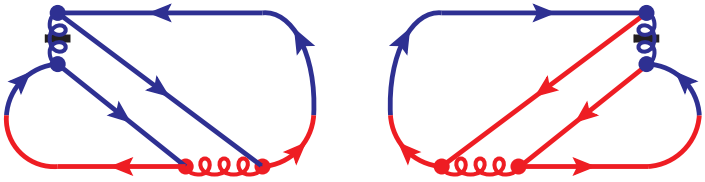

Figure 13. The complete set of diagrams responsible for the IR sensitivity of quark number deposition in $N_{\rm f} \gg N_{\rm c} \gg 1$ QCD.

we find numerically that each interference diagram that contributes to $[\Delta\, d\Gamma/dx_q\, dx_{\rm Q}]_{q\to q{\rm Q}\bar{\rm Q}}$ is individually either symmetric or anti-symmetric under (6.21). If they were all symmetric, then the dominant small-x behavior of the rates $[d\Gamma/dx]^{\rm net}_{q\to {\rm Q}}$ and $[d\Gamma/dx]^{\rm net}_{q\to \bar{\rm Q}}$ would have been equal, and so quark-number deposition would have been infrared safe. The IR sensitivity of quark-number deposition therefore arises exclusively from the diagrams that are anti-symmetric in this soft limit. Interestingly, those diagrams have a simple characterization: they are the $q \to q{\rm Q}\bar{\rm Q}$ diagrams with a single instantaneous longitudinal gluon exchange. The complete set of such diagrams (excluding one that vanishes) is shown in fig. 13.

Unfortunately, we do not know any simple, short, high-level explanation of why these particular diagrams are anti-symmetric in the soft limit. We instead provide a lower-level explanation in appendix D. There also exist diagrams similar to fig. 13 in large-$N_{\rm f}$ QED, but in the QED case *all* diagrams are symmetric under (6.20).

7 Process independence

Our previous results for charge and energy stopping lengths can be used for a first exploration of an important issue, which is whether the effects that must be absorbed into the value of $\hat{q}$ are process independent.

Recall that $\epsilon_{\rm LO}(E_0, z; \hat{q})$ refers to a leading-order LO calculation of energy deposition, based solely on BDMPS-Z splitting rates (expressed in terms of $\hat{q}$) that completely ignore the possibility of overlapping formation times. In our problem, $\hat{q}_{\rm A}$ and $\hat{q}_{\rm F}$ are related by $\hat{q}_{\rm A} = 2\hat{q}_{\rm F}$ in the large-$N_{\rm c}$ limit and more generally by Casimir scaling;[34] so pick one (e.g. $\hat{q}_{\rm F}$) to be the "$\hat{q}$" of this discussion. Imagine (as a thought experiment!) that we (i) could somehow measure the *actual* energy deposition $\epsilon(z)$ of an in-medium gluon-initiated shower in an infinite medium and extract its first moment $\ell_{\rm stop} = \langle z \rangle_\epsilon$, and then (ii) equate that measurement of $\ell_{\rm stop}$ to the formula for the first moment of $\epsilon_{\rm LO}(E_0, \hat{q}, z)$ to extract a "measured" effective $\hat{q}$. The results from table 1 (combined with similar results presented in this paper and in ref. [14] for $\hat{q}$-insensitive ratios involving higher moments) indicate that, with *that* $\hat{q}$ extracted from measurement, everything *else* about the overlap-ignoring distribution $\epsilon_{\rm LO}(E_0, \hat{q}, z)$ should also be in good agreement with measurement.

[34] See footnote 11 for caveats.

$N_f \gg N_c \gg 1$ QCD		
ratio	overlap correction	
	$\mu \propto (\hat{q}E)^{1/4}$	$\mu \propto \big(x(1-x)\hat{q}E\big)^{1/4}$
$\ell_{\rm stop}(g, \text{energy})/\ell_{\rm stop}(q, \text{energy})$	$-0.3\% \times N_f\alpha_s$	$0.2\% \times N_f\alpha_s$
$\ell_{\rm stop}(q, \text{init flavor})/\ell_{\rm stop}(q, \text{energy})$	$-1.2\% \times N_f\alpha_s$	$-0.8\% \times N_f\alpha_s$

Table 8. The relative size of overlap corrections to ratios of different types of stopping distances in large-N_f QCD.

But what if we had instead extracted the value of $\hat{q}$ from the first moment of the energy deposition of a *quark*-initiated shower instead of from a gluon-initiated shower? Would we get almost the same value of effective $\hat{q}$, or would we need a very different value in order to accurately describe energy deposition in the quark-initiated case?

A program of ignoring overlap effects by extracting the value of $\hat{q}$ from one measurement, and then using it to predict other measurements, will hold together only if there is little sensitivity (besides the known sensitivity to energy scale) to what type of measurement one uses (within reason) to extract $\hat{q}$. We can turn this around to say it another way. A necessary condition for success would be that *overlap corrections* to a LO calculation of the ratio

$$\frac{\ell_{\rm stop}(q, \text{energy}; \hat{q}, E_0)}{\ell_{\rm stop}(g, \text{energy}; \hat{q}, E_0)} \tag{7.1}$$

must be small. Above, $\ell_{\rm stop}(i, \text{energy})$ means the first moment of the energy deposition $\epsilon_i(z)$ of a shower initiated by a particle of type i. The numerator and denominator of the ratio (7.1) should be calculated using the same value of $\hat{q}$, in which case the ratio itself is $\hat{q}$-insensitive, just like the $\sigma/\ell_{\rm stop}$ ratios of table 1.

Numerical results for the size of overlap corrections to ratios like (7.1) are given in table 8 for $N_f \gg N_c \gg 1$ QCD. The corrections are small for any reasonable value of $N_f\alpha_s$, which means that extracting an effective value of $\hat{q}$ from one type of measurement would make LO analysis work very well for all types of (IR-safe) measurements considered here.

Small overlap corrections to the $\ell_{\rm stop}$ ratio (7.1) would not be surprising or interesting if the overlap corrections to the individual stopping distances $\ell_{\rm stop}$ were already small to being with. For the purely gluonic showers (N_f=0) studied in refs. [13, 14], NLO corrections to the energy stopping distance were $O(100\%) \times N_c\alpha_s$ and were extremely sensitive to the exact choice of IR factorization scale $\Lambda_{\rm fac}$. The fact that NLO corrections to $\hat{q}$-insensitive ratios like $\sigma/\ell_{\rm stop}$ were found to be extremely small was therefore very significant. The ratios of table 8 can only be examined once we add quarks to the theory, which in this paper has only been done in the large-N_f limit. In that case, the corrections to stopping distances are more moderate, as shown in table 9. Judging only from the $\mu = (\hat{q}_F E)^{1/4}$ column, the NLO corrections to individual stopping distances might appear very small. But this is an accident of that choice of μ, as can be seen from the much larger NLO corrections in the $\mu = \big(x(1-x)\hat{q}_F E\big)^{1/4}$ column,

	$\delta\langle z\rangle/\langle z\rangle^{\rm LO}$	
	$\mu=(\hat{q}_{\rm F}E)^{1/4}$	$\mu=\big(x(1-x)\hat{q}_{\rm F}E\big)^{1/4}$
energy, g	$-0.2\%\times N_{\rm f}\alpha_{\rm s}$	$-8.0\%\times N_{\rm f}\alpha_{\rm s}$
energy, q	$0.1\%\times N_{\rm f}\alpha_{\rm s}$	$-8.1\%\times N_{\rm f}\alpha_{\rm s}$
initial-flavor, q	$-0.1\%\times N_{\rm f}\alpha_{\rm s}$	$-9.0\%\times N_{\rm f}\alpha_{\rm s}$

Table 9. Relative size of overlap corrections to $\ell_{\rm stop}\equiv\langle z\rangle$, given by the ratio of $\delta\langle z\rangle$ and $\langle z\rangle^{\rm LO}$ from tables 4 and 6.

which are roughly 8%. So, the much reduced sensitivity to renormalization scale exhibited by the $\ell_{\rm stop}$ ratios in table 8, and the uniformly small NLO corrections there, is still a significant effect.

Also, it's not just a matter of whether one includes some sort of x dependence in μ. Unlike $\hat{q}$-insensitive quantities like $\sigma/\ell_{\rm stop}$, and $\ell_{\rm stop}$ ratios (7.1), the NLO corrections to $\ell_{\rm stop}$ itself are sensitive to the overall scale of μ. For example, we find that $\mu=\frac{1}{2}(\hat{q}E)^{1/4}$ gives NLO corrections to $\ell_{\rm stop}$ that are comparable to those for $\mu=\big(x(1-x)E\big)^{1/4}$ in table 9 while still giving exactly the same small numbers for corrections to the $\ell_{\rm stop}$ ratios in the $\mu\propto(\hat{q}E)^{1/4}$ column of table 8.

We should note that the second ratio of table 8 is probably not a sensible test of process independence outside of the large-$N_{\rm f}$ approximation. Remember that we have found fermion-number deposition to be IR unsafe in large-$N_{\rm f}$ QCD, and our argument for IR-safety of initial-flavor deposition depended on the large-$N_{\rm f}$ approximation. But the ratio (7.1) of energy stopping distances should always be a good test, even outside of the large-$N_{\rm f}$ limit.

8 Why is QED overlap $\gg$ QCD overlap for comparable $N\alpha$?

In this section, we propose a qualitative explanation for why the relative size of QED overlap effects are so much larger than for QCD overlap effects for comparable values of $N\alpha$. For the sake of simplicity, we will focus our attention on initial-flavor stopping, which involves only the $e\to e$ net rate in QED versus the $q\to q$ net rate in QCD. The size of overlap effects that cannot be absorbed into $\hat{q}$ depends on the x dependence of the ratio of the NLO to LO contributions to that rate. If the ratio

$$\text{Ratio}(x)\equiv\frac{[d\Gamma/dx]^{\rm NLO}_{\underline{e\to e}}}{[d\Gamma/dx]^{\rm LO}_{\underline{e\to e}}} \tag{8.1}$$

and/or its QCD analog were independent of x, the NLO contribution $[d\Gamma/dx]^{\rm NLO}_{\underline{e\to e}}\propto\sqrt{\hat{q}}$ to the rate could be completely absorbed into the leading-order rate $[d\Gamma/dx]^{\rm LO}_{\underline{e\to e}}\propto\sqrt{\hat{q}}$ by replacing $\hat{q}$ by $\hat{q}_{\rm eff}=(1+\text{Ratio})^2\hat{q}$ in the leading-order rate. The actual variation with x is shown in fig.

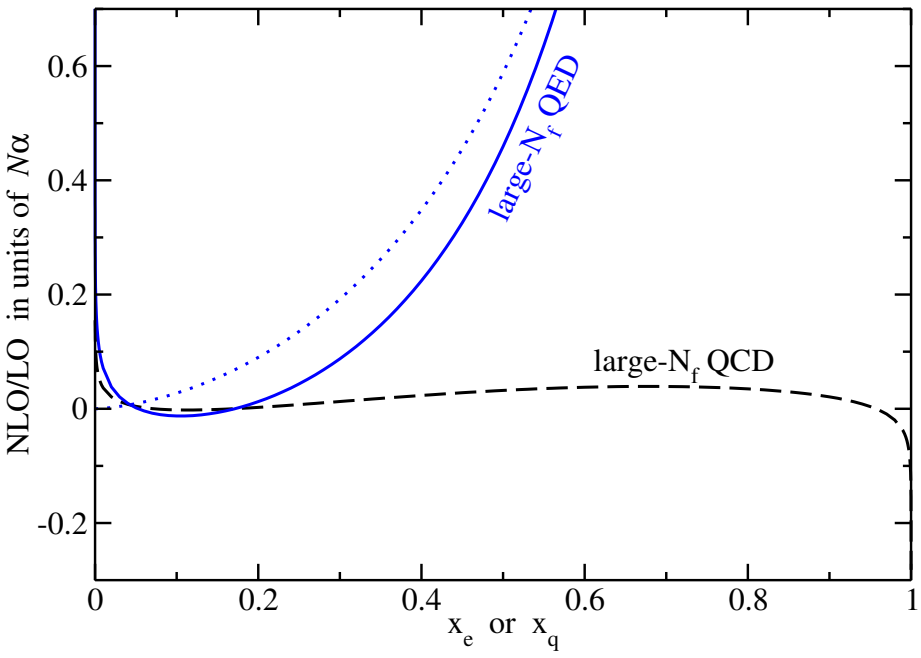

Figure 14. The ratio (8.1) of NLO to LO contributions to the net rates for $e\to e$ (solid blue curve) and $q\to q$ (dashed black curve), in units of $N\alpha$ for $\mu = (\hat{q}_{\rm F}E)^{1/4}$. The dotted blue curve will be explained later in the main text.

14 for QED vs. QCD. The QED curve varies drastically more than the QCD curve; so much so that we can't even fit much of the QED curve into the figure while showing variation of the QCD curve. For reasons to be discussed, the QED ratio has a power-law divergence in the soft photon limit ($1-x_e \to 0$), whereas the QCD ratio has only a mild logarithmic divergence.[35]

To understand the different behaviors in fig. 14 of the NLO/LO ratio for $e\to e$ vs. $q\to q$ in the soft photon or gluon limit, we need to (i) review that limit for the LO bremsstrahlung rate and (ii) understand it for the overlap (NLO) correction.

8.1 Soft bremsstrahlung limit: LO review

The LPM effect depends on the near-collinearity of high-energy bremsstrahlung in the high-energy limit. (The same is true of pair production, but the ensuing discussion here will focus on bremsstrahlung.) The near-collinearity allows for phase coherence in single bremsstrahlung of (i) emission at some time (call it t=0) with (ii) emission at a time $t_{\rm form} \gg \lambda_{\rm rad}$ later, where $\lambda_{\rm rad} \sim 1/\omega_{\rm rad}$ is the wavelength of the bremsstrahlung radiation. There are two competing effects when considering how the formation time behaves for soft bremsstrahlung. First, softer radiation means larger $\lambda_{\rm rad}$, which by itself would make coherence over larger times

[35] The logarithmic divergence of the QCD ratio as $x_q\to 1$ comes solely from the logarithm $L_{\underline{q\to q}}(x_q,\mu)$ of (4.5a), and in detail depends on the x_q dependence of one's choice of renormalization scale μ. (See various alternatives discussed in section 4.3.)

easier and so might be expected to increase $t_{\rm form}$. On the other hand, longer $t_{\rm form}$ allows more opportunity for high-energy particles to pick up more $p_\perp$ kick from the medium over the duration of the bremsstrahlung process and so be driven to be less collinear, which would work toward reducing rather than increasing the time over which the process is coherent. The actual behavior of $t_{\rm form}$ in the soft limit is a balance between these effects. For QED,[36]

$$t_{\rm form}(x_\gamma) \sim \sqrt{\frac{E^2}{\omega_{\rm rad}\hat{q}}} \sim \sqrt{\frac{E}{x_\gamma \hat{q}}} \qquad (x_\gamma \ll 1), \tag{8.2}$$

where E is the energy of the parent. Overall, the QED formation time for bremsstrahlung grows, and so LPM suppression becomes even more significant, in the soft limit.

The situation is very different in QCD because gluons, unlike photons, scatter easily from the medium. The softer the bremsstrahlung gluon, the more a small kick from the medium will change its direction, and so the less collinear the bremsstrahlung process will become. So the effect of scattering from the medium toward reducing formation times is much stronger in the soft limit of QCD bremsstrahlung than QED bremsstrahlung. The result is[37]

$$t_{\rm form}(x_g) \sim \sqrt{\frac{\omega_{\rm rad}}{\hat{q}}} \sim \sqrt{\frac{x_g E}{\hat{q}}} \qquad (x_g \ll 1). \tag{8.3}$$

In QCD, the formation time for bremsstrahlung shrinks, so that there is *less* LPM suppression, in the soft limit (until the formation time becomes as small as the mean free path for scattering from the medium, at which point the $\hat{q}$ approximation breaks down). This difference between soft-gluon vs. soft-photon bremsstrahlung is the most significant qualitative difference between the LPM effect in QCD and QED.

Parametrically, the rate for soft bremsstrahlung is then

$$\left[\frac{d\Gamma}{dx_\gamma}\right]^{\rm LO}_{e\to e\gamma} \sim \frac{\alpha\, P_{e\to e}(x_\gamma)}{t_{\rm form}(x_\gamma)} \sim \frac{\alpha}{x_\gamma^{1/2}}\sqrt{\frac{\hat{q}}{E}} = \frac{\alpha}{(1-x_e)^{1/2}}\sqrt{\frac{\hat{q}}{E}} \qquad (\text{QED},\ x_\gamma \ll 1), \tag{8.4a}$$

$$\left[\frac{d\Gamma}{dx_g}\right]^{\rm LO}_{q\to qg} \sim \frac{\alpha_{\rm s}\, P_{q\to q}(x_g)}{t_{\rm form}(x_g)} \sim \frac{C_{\rm F}\alpha_{\rm s}}{x_g^{3/2}}\sqrt{\frac{\hat{q}}{E}} = \frac{C_{\rm F}\alpha_{\rm s}}{(1-x_q)^{3/2}}\sqrt{\frac{\hat{q}}{E}} \qquad (\text{QCD},\ x_g \ll 1). \tag{8.4b}$$

Note the different power-law behavior in the soft limit, which arises because of the different power-law behavior of the formation time, which in turn arose because gluons interact much more directly with a QCD medium than photons do with a QED medium. Written in the

[36] In terms of more-general formulas, the scale of the QED bremsstrahlung formation time is $t_{\rm form} \sim 1/|\Omega_0|$ with Ω_0 given by (2.4b) with $(x_1, x_2, x_3) = (-1, x_e, x_\gamma)$ and $(\hat{q}_1, \hat{q}_2, \hat{q}_3) = (\hat{q}, \hat{q}, 0)$, since the high-energy photon does not interact directly with the medium. Eq. (8.2) corresponds to the $x_\gamma \ll 1$ limit.

[37] Eq. (8.3) is just the soft limit of the formula (4.14) presented previously.

language of net rates, (8.4) is

$$\left[\frac{d\Gamma}{dx_e}\right]^{\text{LO}}_{\underline{e\to e}} \sim \frac{\alpha}{(1-x_e)^{1/2}}\sqrt{\frac{\hat{q}}{E}} \qquad \text{(QED, } 1-x_e \ll 1\text{)}, \tag{8.5a}$$

$$\left[\frac{d\Gamma}{dx_q}\right]^{\text{LO}}_{\underline{q\to q}} \sim \frac{N_{\text{c}}\alpha_{\text{s}}}{(1-x_q)^{3/2}}\sqrt{\frac{\hat{q}}{E}} \qquad \text{(QCD, } 1-x_q \ll 1\text{)}. \tag{8.5b}$$

8.2 Soft bremsstrahlung limit: overlap corrections

It's now easy to get a first idea of why overlap (NLO) corrections can behave very differently from the LO bremsstrahlung rate in QED. The overlap corrections to the $e\to e$ net rate come from the overlap of bremsstrahlung followed by either real or virtual pair production, as depicted schematically in fig. 15 for real production in the soft-photon limit. As soon as the soft photon converts to a soft electron-positron pair, however, the electron and positron can interact directly with the QED plasma and so—like soft gluons—they can receive and be easily deflected by kicks from the plasma, reducing the collinearity of the entire $e\to e\gamma\to e\text{E}\bar{\text{E}}$ process. When the two splittings overlap, the production of the soft $\text{E}\bar{\text{E}}$ pair therefore significantly disrupts the collinearity needed for the LPM effect in the production of the original $e\to e\gamma$ bremsstrahlung. Based purely on the analogy with LO soft gluon bremsstrahlung (8.5b), one might then guess that this conversion of a soft photon to an $\text{E}\bar{\text{E}}$ pair could produce an overlap correction of size

$$\left[\frac{d\Gamma}{dx_e}\right]^{\text{NLO}}_{\underline{e\to e}} \sim N_{\text{f}}\alpha \times \frac{\alpha}{(1-x_e)^{3/2}}\sqrt{\frac{\hat{q}}{E}} \qquad \text{(QED, } 1-x_e \ll 1\text{)}, \tag{8.6}$$

where the extra factor of $N_{\text{f}}\alpha$ compared to (8.5b) comes from the vertex needed to make the $\text{E}\bar{\text{E}}$ pair. The NLO/LO ratio (8.1) of (8.6) to (8.5a) would then behave like

$$\text{Ratio}(x_e) \sim \frac{N_{\text{f}}\alpha}{1-x_e} \qquad \text{(QED, } 1-x_e \ll 1\text{)} \tag{8.7}$$

and would blow up as $x_e \to 1$. In contrast, QCD overlap effects, where the overlapping pair production does not make the same qualitative change to LO bremsstrahlung, would be

$$\left[\frac{d\Gamma}{dx_q}\right]^{\text{NLO}}_{\underline{q\to q}} \sim N_{\text{f}}\alpha \times \frac{N_{\text{c}}\alpha_{\text{s}}}{(1-x_q)^{3/2}}\sqrt{\frac{\hat{q}}{E}} \qquad \text{(QCD, } 1-x_q \ll 1\text{)}, \tag{8.8}$$

with

$$\text{Ratio}(x_q) \sim N_{\text{f}}\alpha_{\text{s}} \qquad \text{(QCD, } 1-x_q \ll 1\text{)}. \tag{8.9}$$

The above parametric estimates are correct, neglecting logarithms.[38] But it is desirable to better understand the origin of (8.6) by giving a qualitative argument rather than just a qualitative guess.

[38] For the QCD case, see eqs. (4.3), (4.4a) and (4.7a). For the QED case, see the analogous eqs. (3.5a), (3.6) and (3.10a) of ref. [17].

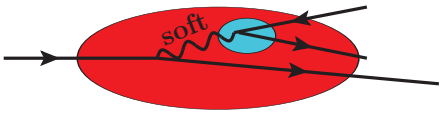

Figure 15. A qualitative depiction of QED bremsstrahlung overlapping with typical pair production in the soft photon limit. The red oval represents the long LO formation time for soft bremsstrahlung, which will be disrupted because of the pair production.

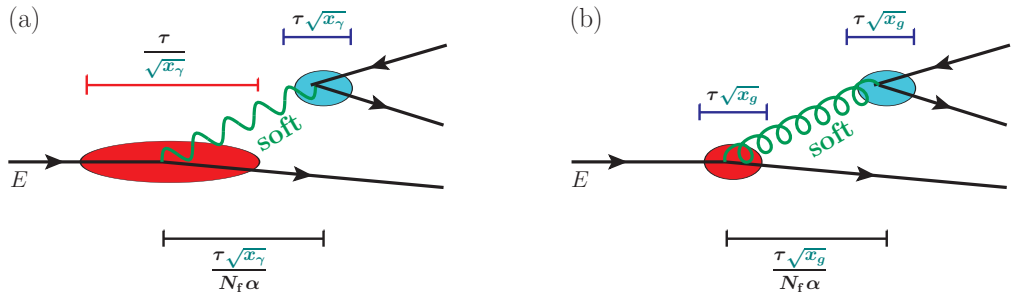

Figure 16. (a) Parametric summary of the relative size of typical formation lengths and distances between a soft QED bremsstrahlung and subsequent democratic pair production, contrasted with (b) the same for QCD. Above, τ represents the parametric scale $\tau \sim \sqrt{E/\hat{q}}$ for a democratic splitting of energy E. These figures may be contrasted with the first part of fig. 4, where all splittings were democratic and the scale of the "formation time" there corresponds to "τ" here.

8.2.1 $N_f\alpha \ll x_\gamma \ll 1$

In our analysis of overlap effects, we treat $N\alpha$ as small and picture overlapping formation times (or at least those that cannot be absorbed into $\hat{q}$) as rare events. We only check those assumptions *a posteriori* when we numerically check the size of final results, such as in table 1. In the spirit of this picture, fig. 16a depicts the typical QED scales involved for soft bremsstrahlung, with formation time (8.2), subsequently followed by democratic pair production. (For comparison, fig. 16b shows the QCD version.) Whether in QED or QCD, democratic splittings from a parent of energy E have formation times of order $\sqrt{E/\hat{q}}$, but the immediate parent of the pair production in the fig. 16a is the photon, whose energy is $x_\gamma E$, so that $t_{\text{form}}^{\text{pair}} \sim \sqrt{x_\gamma E/\hat{q}}$ in the notation of the figure. The probability of pair production is parametrically $N_f\alpha$ per formation time, and so the typical distance the photon travels before pair producing is of order $t_{\text{form}}^{\text{pair}}/N_f\alpha$.

The qualitative features to take away from fig. 16a are that, in the soft photon limit, (i) the bremsstrahlung formation time is parametrically large compared to the subsequent pair production formation time, and (ii) overlap will be common unless the distance between the bremsstrahlung and pair production is parametrically large compared to the bremsstrahlung formation time, which requires $\tau\sqrt{x_\gamma}/N_f\alpha \gg \tau/\sqrt{x_\gamma}$ and so $x_\gamma \gg N_f\alpha$. So, overall, fig. 16a

depicts the situation

$$N_{\rm f}\alpha \ll x_\gamma \ll 1. \tag{8.10}$$

The probability of overlap is parametrically

$$\text{Prob(overlap)} \sim \frac{\text{longer formation time}}{\text{typical separation}} \sim \frac{N_{\rm f}\alpha}{x_\gamma} = \frac{N_{\rm f}\alpha}{1-x_q}\,. \tag{8.11}$$

In the rare occasions that they *do* overlap for (8.10), we should expect the separation between $e \to e\gamma$ and $\gamma \to {\rm E}\bar{\rm E}$ to be of order the $e \to e\gamma$ formation length, because it would be even more unlikely for the pair production to have occurred much earlier than that. The disruption to the formation of the soft bremsstrahlung due to the creation of the more-easily scattered ${\rm E}\bar{\rm E}$ can therefore be expected to have an $O(100\%)$ effect (but not larger) on the $e \to e\gamma$ splitting for the events where they overlap. So we are led to estimate

$$\left[\frac{d\Gamma}{dx_e}\right]^{\rm NLO}_{\underline{e\to e}} \sim \left[\frac{d\Gamma}{dx_e}\right]^{\rm LO}_{\underline{e\to e}} \times \text{Prob(overlap)} \times O(100\%) \sim \left[\frac{d\Gamma}{dx_e}\right]^{\rm LO}_{\underline{e\to e}} \times \frac{N_{\rm f}\alpha}{1-x_q}\,, \tag{8.12}$$

which is the same as the earlier guess (8.6).

8.2.2 $x_\gamma \ll N_{\rm f}\alpha$

Nothing special about the scale $x_\gamma \sim N_{\rm f}\alpha_{\rm s}$ was built into the calculation in ref. [16] of rates such as $[\Delta\, d\Gamma/dx_e x_{\rm E}]^{\rm NLO}_{e\to e{\rm E}\bar{\rm E}}$ for overlapping splitting. So, as far as those calculations are concerned, there's no reason not to qualitatively discuss $x_\gamma \ll N_{\rm f}\alpha_{\rm s}$ as well. In that limit, the separation between the soft bremsstrahlung and the pair production is short compared to the soft bremsstrahlung formation time, and so the probability of overlap is

$$\text{Prob(overlap)} \simeq 100\% \tag{8.13}$$

instead of (8.11). But, once produced, the creation of the more-easily scattered soft E and $\bar{\rm E}$ will quickly terminate the coherence of the original bremsstrahlung process after a time of order the pair-production formation time. This will effectively shorten the soft QED bremsstrahlung formation time from the leading-order result (8.2) to

$$(t_{\rm form})_{\rm eff} \sim \text{(typical separation)} + \text{(pair formation time)} \tag{8.14}$$

$$\sim \text{(typical separation)} \sim \frac{x_\gamma^{1/2}}{N_{\rm f}\alpha}\sqrt{\frac{E}{\hat q}}. \tag{8.15}$$

Correspondingly, the rate (8.4a) for soft QED bremsstrahlung will then be changed to

$$\left[\frac{d\Gamma}{dx_e}\right]^{\rm NLO}_{\underline{e\to e}} \sim \frac{\alpha\, P_{e\to e}(x_\gamma)}{(t_{\rm form})_{\rm eff}} \sim \frac{N_{\rm f}\alpha^2}{x_\gamma^{3/2}}\sqrt{\frac{\hat q}{E}}, \tag{8.16}$$

which also matches the earlier guess (8.6).

A precise calculation of the rate for $x_\gamma \lesssim N_{\rm f}\alpha$ in QED would likely require resumming higher-order effects. But the analyses here for this case and the $N_{\rm f}\alpha \ll x_\gamma \ll 1$ case provide a qualitative explanation for (8.7) and so for the QED behavior found in fig. 14.

8.3 Logarithms and a more quantitative comparison

In ref. [17], it was found that the power-law behavior (8.6) of $[d\Gamma/dx_e]^{\rm NLO}_{\underline{e\to e}}$ in the soft-photon limit was supplemented by a logarithm $\ln(1-x_e)$. Moreover, the overlap rate could be calculated relatively simply to leading order in this logarithm without invoking any of the long and complicated formalism for computing overlapping splitting rates. Specifically, whenever one splitting has a parametrically small LO formation time compared to the other, then one can compute the overlap correction to leading-log order by treating the splitting with the longer formation time as a vacuum-like DGLAP initial radiation (or final-state fragmentation correction) to the leading-order LPM formula for the other splitting. Ref. [17] found that[39]

$$\left[\frac{d\Gamma}{dx_e}\right]^{\rm NLO}_{\underline{e\to e}} \approx -\frac{3N_{\rm f}\alpha^2}{8\pi}\,\frac{\ln(1-x_e)}{(1-x_e)^{3/2}}\sqrt{\frac{\hat{q}}{E}} \qquad \text{(QED, } 1-x_e \ll 1\text{)}, \tag{8.17}$$

where we use $\approx$ to indicate a leading-log approximation. This approximation to the NLO net rate corresponds to the dotted blue curve in the plot of the NLO/LO ratio in fig. 14. As can be seen, it roughly captures the large variation of that ratio with x_e and so one might expect it to capture a large part of the overlap effects in QED that cannot be absorbed into $\hat{q}$. If we use the recursion relations [17] for moments of the QED charge deposition distribution, analogous to the initial-flavor discussion of section 5.1, but use the approximation (8.17) to the NLO net rate, we find that the size of overlap corrections to $\sigma/\ell_{\rm stop}$ for charge or initial-flavor deposition would be $-78\% \times N_{\rm f}\alpha$.[40] By itself, the leading-log soft-photon approximation (8.17) explains most of the $-85\% \times N_{\rm f}\alpha$ result quoted in table 1. This gives support to our explanation that the dramatically larger size of overlap effects in QED compared to QCD (at comparable values of $N\alpha$) arises from the qualitative mismatch between the behavior of soft photon emission at leading order vs. NLO.

9 Conclusion

Our focus has been on the size of overlap effects for in-medium shower development that cannot be absorbed into an effective value of $\hat{q}$. Our result here that such effects are small for $N_{\rm f}\gg N_{\rm c}\gg 1$ QCD suggests that the small size found for purely gluonic ($N_{\rm f}=0$) showers was not simply a numerical accident peculiar to that particular calculation. Equally important for confidence in the QCD results, we believe we now understand why similar results for QED are drastically larger for comparable values of $N\alpha$. Overlap allows soft bremsstrahlung photons

[39] See eq. (B.7) of ref. [17] and the discussion leading up to it, which invokes an earlier argument made in appendix B.1 of ref. [21].

[40] Useless but fun fact: Using the full LO rate for $e\to e$ but taking the approximation (8.17) for the NLO rate, it is possible to perform all of the QED integrals analytically for this particular calculation. (See appendix E of ref. [17] for the relevant integrals involving LO quantities.) The result is

$$\chi\alpha = -\left[\frac{8}{3\pi} + \frac{360(\pi - \pi\ln 2 - 1)}{(525\pi - 1472)}\right] N_{\rm f}\alpha,$$

which, when rounded, equals the $-78\% \times N_{\rm f}\alpha$ number quoted above.

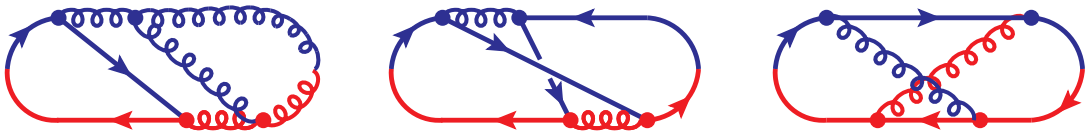

Figure 17. A few examples of additional interference diagrams that would have to be computed to generalize existing large-N_f and N_f=0 results to any N_f.

to convert to a soft electron/positron pair while the bremsstrahlung is still in progress, and a soft electron/positron pair is easily scattered by the QED medium, significantly modifying the LPM effect for the original soft bremsstrahlung. In contrast, soft gluons already interact easily with the QCD medium and so overlap does not make the same qualitative change.

It would be interesting to check our qualitative conclusions for $N_f \sim N_c$ as well, to make sure that nothing changes dramatically. This would require computing several new interference diagrams, some examples of which are shown in fig. 17. In the $N_f \gg N_c$ limit of this paper, we were able to ignore the soft double logarithms that complicated the calculation of $\hat{q}$-insensitive overlap effects for purely gluonic (N_f=0) showers. In the purely gluonic case, those soft double logarithms had to be factorized and carefully absorbed into $\hat{q}$. In the future, studying $N_f \sim N_c$ could test whether that factorization might somehow introduce larger overlap effects in showers equally composed of quarks and gluons.

Acknowledgments

The work of Arnold and Elgedawy (while at U. Virginia) was supported, in part, by the U.S. Department of Energy under Grant No. DE-SC0007974. Elgedawy's work at South China Normal University was supported by Guangdong Major Project of Basic and Applied Basic Research No. 2020B0301030008 and by the National Natural Science Foundation of China under Grant No. 12035007. Arnold is grateful for the hospitality of the EIC Theory Institute at Brookhaven National Lab for one of the months during which he was working on this paper. Iqbal thanks the CERN Theoretical Physics Department for their hospitality and support during the time that this work was being completed. We also thank John Collins for sharing his scripts that convert jaxodraw files into encapsulated postscript files with transparent backgrounds, which were used in the creation of fig. 10.

A Summary of Basic Rate Formulas

In this appendix, we gather our results for the basic rates of eq. (2.19), adapted as described in section 3 from the large-N_f QED results of ref. [16]. We present the formulas in notation appropriate for large-N_f QCD, where

$$C_A = N_c, \qquad C_F = \tfrac{N_c}{2}, \qquad t_F = \tfrac{1}{2}, \qquad d_A = N_c^2, \qquad d_F = N_c \qquad (N_c \gg 1 \text{ QCD}). \tag{A.1}$$

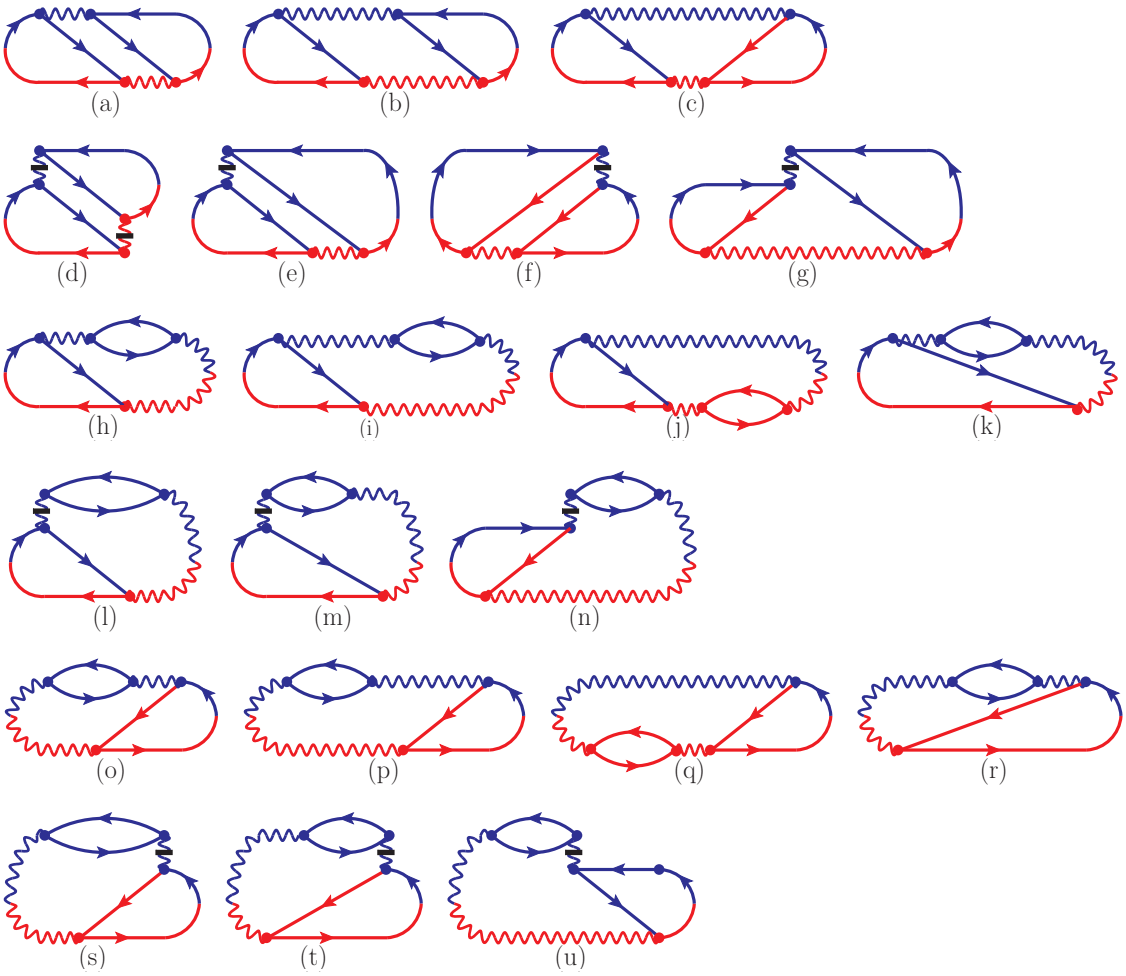

Figure 18. The complete set of NLO time-ordered diagrams needed to compute overlap effects in large-N_f QED, taken from ref. [16], with the caveat that $2\,\mathrm{Re}[\cdots]$ should be applied to add in the diagrams' complex conjugates. Reinterpreting the photon lines as gluon lines gives large-N_f QCD.

But the results for large-N_f QED can be recovered by instead using

$$C_A = 0, \qquad C_F = 1, \qquad t_F = 1, \qquad d_A = 1, \qquad d_F = 1 \qquad \text{(QED)}, \tag{A.2}$$

replacing α_s by electromagnetic α_{EM}, and using the few explicitly designated QED versions of formulas below.

Many of the formulas below will refer to the contribution of specific diagrams, as originally labeled in ref. [16]. For reference, we reproduce the complete set of diagrams and labels in fig. 18.

In what follows, we will rewrite the x_Q of the main text as

$$y_Q \equiv x_Q \tag{A.3}$$

just for the sake of (i) making it a little easier to avoid confusion of x_q and $x_{\rm Q}$ and (ii) compatibility with the notation of ref. [16].

In addition to generalization to QCD, this appendix incorporates some corrections to the formulas presented in ref. [16] that, as of this writing, have not yet appeared in a published erratum.[41]

A.1 Leading-order single-splitting rates

A.1.1 $q \to qg$

In our notation, the leading-order $q\to qg$ rate is

$$\left[\frac{d\Gamma}{dx_q}\right]^{\rm LO}_{q\to qg} = \frac{\alpha_{\rm s}}{\pi}\,P_{q\to q}(x_q)\,\mathrm{Re}(i\Omega_0) = \frac{\alpha_{\rm s}}{\pi}\,P_{q\to g}(x_g)\,\mathrm{Re}(i\Omega_0) \tag{A.4}$$

with $x_g = 1 - x_q$,

$$\Omega_0 = \sqrt{\frac{-i\hat{q}_{\rm F}}{2E}\left(\frac{1}{x_q} + \frac{C_{\rm A}}{C_{\rm F}(1-x_q)} - 1\right)}\,, \tag{A.5}$$

and the relevant DGLAP splitting function

$$P_{q\to q}(x_q) = P_{q\to g}(x_g) = C_{\rm F}\frac{1+x_q^2}{1-x_q} = C_{\rm F}\frac{1+(1-x_g)^2}{x_g}. \tag{A.6}$$

A.1.2 $g \to \mathrm{Q}\bar{\mathrm{Q}}$

$$\left[\frac{d\Gamma}{dy_{\rm Q}}\right]^{\rm LO}_{g\to \mathrm{Q}\bar{\mathrm{Q}}} = \frac{N_{\rm f}\alpha_{\rm s}}{\pi}\,P_{g\to q}(y_{\rm Q})\,\mathrm{Re}(i\Omega_0^{g\to \mathrm{Q}\bar{\mathrm{Q}}}) \tag{A.7}$$

with

$$\Omega_0^{g\to \mathrm{Q}\bar{\mathrm{Q}}} = \sqrt{\frac{-i\hat{q}_{\rm F}}{2E}\left(\frac{1}{y_{\rm Q}} + \frac{1}{1-y_{\rm Q}} - \frac{C_{\rm A}}{C_{\rm F}}\right)} \tag{A.8}$$

and

$$P_{g\to q}(y_{\rm Q}) = t_{\rm F}[y_{\rm Q}^2 + (1-y_{\rm Q})^2]. \tag{A.9}$$

A.2 Overlap corrections to real double splitting

The total result for the overlap correction to real double splitting decomposes as

$$\left[\frac{\Delta\, d\Gamma}{dx_q\, dy_{\rm Q}}\right]_{q\to q\mathrm{Q}\bar{\mathrm{Q}}} = \left[\frac{\Delta\, d\Gamma}{dx_q\, dy_{\rm Q}}\right]_{\rm seq} + \left[\frac{d\Gamma}{dx_q\, dy_{\rm Q}}\right]_{(I)} + \left[\frac{d\Gamma}{dx_q\, dy_{\rm Q}}\right]_{(II)}, \tag{A.10}$$

where the pieces are given below and "I" indicates a contribution involving an instantaneous 4-fermion interaction (arising from longitudinally-polarized gluon exchange).

[41] Specifically, eqs. (A.29c) and (A.27) of the original publication of ref. [16] have been corrected here so that they work properly with front-end transformations. The works of [15, 17] based on ref. [16] were not affected because ref. [15] did not depend on those formulas and our numerical work for ref. [17] implemented them in a way that avoided the errors.

A.2.1 Sequential diagrams

The "seq" piece above is our result for diagrams (a–c) of fig. 18, which are of a type referred to as "sequential" diagrams in earlier papers.

$$\left[\frac{\Delta\, d\Gamma}{dx_q\, dy_{\rm Q}}\right]_{\rm seq} = 2N_{\rm f}\mathcal{A}_{\rm seq}(x_q, y_{\rm Q}) \tag{A.11}$$

with[42]

$$\mathcal{A}_{\rm seq}(x_q, y_{\rm Q}) = \mathcal{A}^{\rm pole}_{\rm seq}(x_q, y_{\rm Q}) + \int_0^{+\infty} d(\Delta t)\left[2\,{\rm Re}\big(B_{\rm seq}(x_q, y_{\rm Q}, \Delta t)\big) + F_{\rm seq}(x_q, y_{\rm Q}, \Delta t)\right], \tag{A.12}$$

$$\begin{aligned} B_{\rm seq}(x_q, y_{\rm Q}, \Delta t) &= C_{\rm seq}(\hat{x}_1, \hat{x}_2, \hat{x}_3, \hat{x}_4, \bar{\alpha}, \bar{\beta}, \bar{\gamma}, \Delta t) \\ &= C_{\rm seq}(-1, y_{\rm Q}, 1{-}x_q{-}y_{\rm Q}, x_q, \bar{\alpha}, \bar{\beta}, \bar{\gamma}, \Delta t), \end{aligned} \tag{A.13}$$

$$C_{\rm seq} = D_{\rm seq} - \lim_{\hat{q}\to 0} D_{\rm seq}, \tag{A.14}$$

$$\begin{aligned} &D_{\rm seq}(x_1{,}x_2, x_3, x_4, \bar{\alpha}, \bar{\beta}, \bar{\gamma}, \Delta t) = \\ &\quad t_{\rm F}C_{\rm F}\frac{\alpha_{\rm s}^2 M_{\rm i} M_{\rm f}^{\rm seq}}{32\pi^4 E^2}\,(-x_1x_2x_3x_4)\,\Omega_+\csc(\Omega_+\Delta t)\,\Omega_-\csc(\Omega_-\Delta t) \\ &\quad\times\Big\{(\bar{\beta}Y_{\rm y}^{\rm seq}Y_{\bar{\rm x}}^{\rm seq} + \bar{\alpha}\overline{Y}_{{\rm y}\bar{\rm x}}^{\rm seq}Y_{{\rm y}\bar{\rm x}}^{\rm seq})I_0^{\rm seq} + (\bar{\alpha}+\bar{\beta}+2\bar{\gamma})Z_{{\rm y}\bar{\rm x}}^{\rm seq}I_1^{\rm seq} \\ &\qquad + \big[(\bar{\alpha}+\bar{\gamma})Y_{\rm y}^{\rm seq}Y_{\bar{\rm x}}^{\rm seq} + (\bar{\beta}+\bar{\gamma})\overline{Y}_{{\rm y}\bar{\rm x}}^{\rm seq}Y_{{\rm y}\bar{\rm x}}^{\rm seq}\big]I_2^{\rm seq} \\ &\qquad - (\bar{\alpha}+\bar{\beta}+\bar{\gamma})(\overline{Y}_{{\rm y}\bar{\rm x}}^{\rm seq}Y_{\bar{\rm x}}^{\rm seq}I_3^{\rm seq} + Y_{\rm y}^{\rm seq}Y_{{\rm y}\bar{\rm x}}^{\rm seq}I_4^{\rm seq})\Big\}, \end{aligned} \tag{A.15}$$

$$\begin{aligned} F_{\rm seq}(x_q, y_{\rm Q}, \Delta t) = &\frac{\alpha_{\rm s}^2 P_{q\to q}(x_q) P_{g\to q}(\frac{y_{\rm Q}}{1-x_q})}{4\pi^2(1-x_q)}\Big[{\rm Re}\big(i(\Omega\,{\rm sgn}\,M)_{\rm i}\big)\ {\rm Re}\big(\Delta t\,(\Omega_{\rm f}^{\rm seq})^2\csc^2(\Omega_{\rm f}^{\rm seq}\,\Delta t)\big) \\ &+ {\rm Re}\big(i(\Omega\,{\rm sgn}\,M)_{\rm f}^{\rm seq}\big)\ {\rm Re}\big(\Delta t\,\Omega_{\rm i}^2\csc^2(\Omega_{\rm i}\,\Delta t)\big)\Big], \end{aligned} \tag{A.16}$$

$$\begin{aligned} \mathcal{A}^{\rm pole}_{\rm seq}(x_q, y_{\rm Q}) = -\frac{\alpha_{\rm s}^2\, P_{q\to q}(x_q)\, P_{g\to q}(\frac{y_{\rm Q}}{1-x_q})}{4\pi^2(1-x_q)}\,{\rm Re}\Big[&i(\Omega\,{\rm sgn}\,M)_{\rm i}\,(1+\tfrac{i\pi}{2}\,{\rm sgn}\,M_{\rm f}^{\rm seq}) \\ &+ i(\Omega\,{\rm sgn}\,M)_{\rm f}^{\rm seq}\,(1+\tfrac{i\pi}{2}\,{\rm sgn}\,M_{\rm i})\Big] \end{aligned} \tag{A.17a}$$

or equivalently

$$\begin{aligned} \mathcal{A}^{\rm pole}_{\rm seq}(x_q, y_{\rm Q}) = -\frac{\alpha_{\rm s}^2\, P_{q\to q}(x_q)\, P_{g\to q}(\frac{y_{\rm Q}}{1-x_q})}{4\pi^2(1-x_q)}\,{\rm Re}\big[&i(\Omega\,{\rm sgn}\,M)_{\rm i} + i(\Omega\,{\rm sgn}\,M)_{\rm f}^{\rm seq}\big] \\ &\times\big(1-\tfrac{\pi}{2}\,{\rm sgn}\,M_{\rm i}\,{\rm sgn}\,M_{\rm f}^{\rm seq}\big), \end{aligned} \tag{A.17b}$$

[42] Note the factors of $t_{\rm F}C_{\rm F}$ needed for (A.16) and (A.17) come from the formulas for $P_{q\to q}$ and $P_{g\to q}$.

and

$$M_{\rm i} = x_1 x_4 (x_1 + x_4) E, \qquad M_{\rm f}^{\rm seq} = x_2 x_3 (x_2 + x_3) E. \tag{A.18}$$

The $I_n^{\rm seq}$ above represent

$$I_0^{\rm seq} = \frac{4\pi^2}{[X_{\rm y}^{\rm seq} X_{\bar{\rm x}}^{\rm seq} - (X_{\rm y\bar{x}}^{\rm seq})^2]}\,, \tag{A.19a}$$

$$I_1^{\rm seq} = -\frac{2\pi^2}{X_{\rm y\bar{x}}^{\rm seq}} \ln\left(1 - \frac{(X_{\rm y\bar{x}}^{\rm seq})^2}{X_{\rm y}^{\rm seq} X_{\bar{\rm x}}^{\rm seq}}\right)\,, \tag{A.19b}$$

$$I_2^{\rm seq} = \frac{2\pi^2}{(X_{\rm y\bar{x}}^{\rm seq})^2} \ln\left(1 - \frac{(X_{\rm y\bar{x}}^{\rm seq})^2}{X_{\rm y}^{\rm seq} X_{\bar{\rm x}}^{\rm seq}}\right) + \frac{4\pi^2}{[X_{\rm y}^{\rm seq} X_{\bar{\rm x}}^{\rm seq} - (X_{\rm y\bar{x}}^{\rm seq})^2]}\,, \tag{A.19c}$$

$$I_3^{\rm seq} = \frac{4\pi^2 X_{\rm y\bar{x}}^{\rm seq}}{X_{\bar{\rm x}}^{\rm seq}[X_{\rm y}^{\rm seq} X_{\bar{\rm x}}^{\rm seq} - (X_{\rm y\bar{x}}^{\rm seq})^2]}\,, \tag{A.19d}$$

$$I_4^{\rm seq} = \frac{4\pi^2 X_{\rm y\bar{x}}^{\rm seq}}{X_{\rm y}^{\rm seq}[X_{\rm y}^{\rm seq} X_{\bar{\rm x}}^{\rm seq} - (X_{\rm y\bar{x}}^{\rm seq})^2]}\,. \tag{A.19e}$$

Here and in (A.15), the $(X, Y, Z)^{\rm seq}$ are defined by

$$\begin{pmatrix} X_{\rm y}^{\rm seq} & Y_{\rm y}^{\rm seq} \\ Y_{\rm y}^{\rm seq} & Z_{\rm y}^{\rm seq} \end{pmatrix} \equiv \begin{pmatrix} |M_{\rm i}|\Omega_{\rm i} & 0 \\ 0 & 0 \end{pmatrix} - i a_{\rm y}^{-1\top} \begin{pmatrix} \Omega_+ \cot(\Omega_+ \Delta t) & 0 \\ 0 & \Omega_- \cot(\Omega_- \Delta t) \end{pmatrix} a_{\rm y}^{-1}, \tag{A.20a}$$

$$\begin{pmatrix} X_{\bar{\rm x}}^{\rm seq} & Y_{\bar{\rm x}}^{\rm seq} \\ Y_{\bar{\rm x}}^{\rm seq} & Z_{\bar{\rm x}}^{\rm seq} \end{pmatrix} \equiv \begin{pmatrix} |M_{\rm f}^{\rm seq}|\Omega_{\rm f}^{\rm seq} & 0 \\ 0 & 0 \end{pmatrix} - i (a_{\bar{\rm x}}^{\rm seq})^{-1\top} \begin{pmatrix} \Omega_+ \cot(\Omega_+ \Delta t) & 0 \\ 0 & \Omega_- \cot(\Omega_- \Delta t) \end{pmatrix} (a_{\bar{\rm x}}^{\rm seq})^{-1}, \tag{A.20b}$$

$$\begin{pmatrix} X_{\rm y\bar{x}}^{\rm seq} & Y_{\rm y\bar{x}}^{\rm seq} \\ \overline{Y}_{\rm y\bar{x}}^{\rm seq} & Z_{\rm y\bar{x}}^{\rm seq} \end{pmatrix} \equiv -i a_{\rm y}^{-1\top} \begin{pmatrix} \Omega_+ \csc(\Omega_+ \Delta t) & 0 \\ 0 & \Omega_- \csc(\Omega_- \Delta t) \end{pmatrix} (a_{\bar{\rm x}}^{\rm seq})^{-1}, \tag{A.20c}$$

where the a's and Ω's will be given below. The quantities $(\bar\alpha, \bar\beta, \bar\gamma)$ in (A.13) represent various combinations of helicity-dependent DGLAP splitting functions and are

$$\begin{pmatrix} \bar\alpha \\ \bar\beta \\ \bar\gamma \end{pmatrix}_{q\to q{\rm Q}\bar{\rm Q}} = \frac{1}{(1-x_q)^6} \left\{ \begin{pmatrix} - \\ + \\ + \end{pmatrix} \frac{4}{|x_q y_{\rm Q} z_{\bar{\rm Q}}|} + \begin{pmatrix} + \\ + \\ - \end{pmatrix} \left[\left(1 + \frac{1}{x_q^2}\right)\left(\frac{1}{y_{\rm Q}^2} + \frac{1}{z_{\bar{\rm Q}}^2}\right) \right] \right\}, \tag{A.21}$$

where

$$z_{\bar{\rm Q}} \equiv 1 - x_q - y_{\rm Q}. \tag{A.22}$$

The 3-body frequencies needed in the above formulas are

$$\Omega_{\rm i}(x_1, x_2, x_3, x_4) = \sqrt{\frac{-i\hat{q}_{\rm F}}{2E}\left(\frac{1}{x_1} + \frac{1}{x_4} - \frac{C_{\rm A}}{C_{\rm F}(x_1 + x_4)}\right)}\,, \tag{A.23}$$

$$\Omega_{\rm f}^{\rm seq}(x_1, x_2, x_3, x_4) = \sqrt{\frac{-i\hat{q}_{\rm F}}{2E}\left(\frac{1}{x_2} + \frac{1}{x_3} - \frac{C_{\rm A}}{C_{\rm F}(x_2 + x_3)}\right)}. \tag{A.24}$$

We don't have neat packaging of the formulas for 4-body normal mode frequencies $\Omega_\pm$ and matrices a of normal modes that covers both QCD and QED, so we present them as separate cases. Because of branch cut issues when later using these formulas with front-end transformations, where variables such as x_4 may be negative, it is important to avoid making algebraic simplifications like $x_4/\sqrt{x_4} = \sqrt{x_4}$ in (A.25b) and (A.26b) below.[43]

$N_\mathrm{f} \gg N_\mathrm{c} \gg 1$ *QCD*:

$$\Omega_+ = \sqrt{-\frac{i\hat{q}_\mathrm{F}}{2E}\left(\frac{1}{x_3}+\frac{1}{x_4}\right)}, \qquad \Omega_- = \sqrt{-\frac{i\hat{q}_\mathrm{F}}{2E}\left(\frac{1}{x_1}+\frac{1}{x_2}\right)}, \tag{A.25a}$$

$$a_y = \frac{1}{(x_1+x_4)}\begin{pmatrix} -x_3 & -x_2 \\ x_4 & x_1 \end{pmatrix}\begin{pmatrix} \frac{1}{\sqrt{x_3x_4(x_3+x_4)E}} & 0 \\ 0 & \frac{1}{\sqrt{x_1x_2(x_1+x_2)E}} \end{pmatrix}. \tag{A.25b}$$

large-N_f QED:

$$\Omega_+ = \sqrt{-\frac{i\hat{q}_\mathrm{F}}{2E}\Big(\frac{1}{x_1}+\frac{1}{x_2}+\frac{1}{x_3}+\frac{1}{x_4}\Big)}, \qquad \Omega_- = 0, \tag{A.26a}$$

$$a_\mathrm{y} = \Big[(-x_1x_2x_3x_4)\big(\frac{1}{x_1}+\frac{1}{x_2}+\frac{1}{x_3}+\frac{1}{x_4}\big)E\Big]^{-1/2}\begin{pmatrix} \frac{x_2x_3}{(-x_1x_2x_3x_4)^{1/2}} & 1 \\ \frac{x_1x_4}{(-x_1x_2x_3x_4)^{1/2}} & 1 \end{pmatrix}, \tag{A.26b}$$

with the understanding that every $\Omega_- \cot(\Omega_- \Delta t)$ or $\Omega_- \csc(\Omega_- \Delta t)$ should be interpreted as $1/\Delta t$ when $\Omega_- = 0$.

In both cases,

$$a^\mathrm{seq}_{\bar{\mathrm{x}}} = \begin{pmatrix} 0 & 1 \\ 1 & 0 \end{pmatrix} a_\mathrm{y}. \tag{A.27}$$

A.2.2 Diagrams with one instantaneous vertex

The "(I)" piece of our result (A.10) is the contribution from diagrams (e–g) of fig. 18.

$$\left[\frac{d\Gamma}{dx_q\, dy_\mathrm{Q}}\right]_{(I)} = 2N_\mathrm{f}\, \mathcal{A}_I(x_q, y_\mathrm{Q}), \tag{A.28a}$$

$$\mathcal{A}_I(x_q, y_\mathrm{Q}) \equiv \int_0^\infty d(\Delta t)\, 2\,\mathrm{Re}\big(B_I(x_q, y_\mathrm{Q}, \Delta t)\big), \tag{A.28b}$$

[43] As long as one uses a consistent convention for the square roots of negative numbers, e.g. they are always positive imaginary, the columns of a_y resulting from eqs. (A.25b) and (A.26b) will correctly give normal modes even in the case of front-end transformations. Consistently choosing the square roots of negative numbers to be negative imaginary would also work, since the overall sign of normal modes is a matter of convention and does not affect the combinations (A.20) that depend directly or indirectly on a_y. However, changes like $x_4/\sqrt{x_4} \to \sqrt{x_4}$ can incorrectly alter relative signs within a normal mode rather than just its overall sign.

$$B_I(x_q, y_{\bar{\rm Q}}, \Delta t) = \frac{4\big|x_q y_{\bar{\rm Q}}(1{-}x_q{-}y_{\bar{\rm Q}})\big|^{1/2}}{(1-x_q)^2}\Big[D_I(\hat{x}_1, \hat{x}_2, \hat{x}_3, \hat{x}_4, \zeta, \Delta t) + D_I(-\hat{x}_3, -\hat{x}_4, -\hat{x}_1, -\hat{x}_2, \zeta, \Delta t)\Big]$$
$$= \frac{4\big|x_q y_{\bar{\rm Q}}(1{-}x_q{-}y_{\bar{\rm Q}})\big|^{1/2}}{(1-x_q)^2}\Big[D_I(-1, y_{\bar{\rm Q}}, 1{-}x_q{-}y_{\bar{\rm Q}}, x_q, \zeta, \Delta t) + D_I(-(1{-}x_q{-}y_{\bar{\rm Q}}), -x_q, 1, -y_{\bar{\rm Q}}, \zeta, \Delta t)\Big], \tag{A.28c}$$

$$D_I(x_1, x_2, x_3, x_4, \zeta, \Delta t) = -\,t_{\rm F} C_{\rm F} \frac{\alpha_{\rm s}^2 M_{\rm f}^{\rm seq}}{16\pi^2 E}\,(-x_1 x_2 x_3 x_4)\zeta\,\Omega_+\csc(\Omega_+\,\Delta t)\,\Omega_-\csc(\Omega_-\,\Delta t)\,\frac{Y_{\bar{\rm x}}^{\rm seq}}{X_{\bar{\rm x}}^{\rm seq}}\,, \tag{A.28d}$$

where

$$\zeta = \frac{(1{+}|x_q|)\,(|y_{\bar{\rm Q}}|{+}|z_{\bar{\rm Q}}|)}{(1-x_q)^3|x_q y_{\bar{\rm Q}} z_{\bar{\rm Q}}|^{3/2}}\,. \tag{A.29}$$

$M_{\rm f}^{\rm seq}$, $\Omega_{\rm f}^{\rm seq}$, and $\Omega_\pm$ are given here by the previous general formulas (A.18), (A.24), and (A.25a) or (A.26a), for use in (A.20b) for $X_{\bar{\rm x}}^{\rm seq}$ and $Y_{\bar{\rm x}}^{\rm seq}$.

Later, we will need to refer separately to the contributions of the three diagrams (e–g). The above formula for $[d\Gamma/dx_q\,dy_{\bar{\rm Q}}]_{(I)}$ can be decomposed as

$$\left[\frac{d\Gamma}{dx_q\,dy_{\bar{\rm Q}}}\right]_{(I)} = 2\,{\rm Re}\left[\frac{d\Gamma}{dx_q\,dy_{\bar{\rm Q}}}\right]_{\rm (e)} + 2\,{\rm Re}\left[\frac{d\Gamma}{dx_q\,dy_{\bar{\rm Q}}}\right]_{\rm (f)} + 2\,{\rm Re}\left[\frac{d\Gamma}{dx_q\,dy_{\bar{\rm Q}}}\right]_{\rm (g)} \tag{A.30}$$

where

$$2\,{\rm Re}\left[\frac{d\Gamma}{dx_q\,dy_{\bar{\rm Q}}}\right]_{\rm (e)} = \text{Eqs. (A.28) using only the } \textit{first } D_I \text{ term in (A.28c)}; \tag{A.31}$$

$$2\,{\rm Re}\left[\frac{d\Gamma}{dx_q\,dy_{\bar{\rm Q}}}\right]_{\rm (f)} = \text{Eqs. (A.28) using only the } \textit{second } D_I \text{ term in (A.28c)}; \tag{A.32}$$

$$2\,{\rm Re}\left[\frac{d\Gamma}{dx_q\,dy_{\bar{\rm Q}}}\right]_{\rm (g)} = 0. \tag{A.33}$$

A.2.3 Diagrams with two instantaneous vertices

The "(II)" piece of our result (A.10) is the contribution from diagram (d) of fig. 18, which gives[44]

$$\left[\frac{d\Gamma}{dx_q\,dy_{\bar{\rm Q}}}\right]_{(II)} = 2\,{\rm Re}\left[\frac{d\Gamma}{dx_q\,dy_{\bar{\rm Q}}}\right]_{\rm (d)}$$
$$= -t_{\rm F} C_{\rm F}\frac{2N_{\rm f}\alpha_{\rm s}^2}{\pi^2}\,\frac{x_q y_{\bar{\rm Q}} z_{\bar{\rm Q}}}{(1-x_q)^4}\int_0^\infty d(\Delta t)\,2\,{\rm Re}\left[\Omega_+\csc(\Omega_+\,\Delta t)\,\Omega_-\csc(\Omega_-\,\Delta t) - \frac{1}{(\Delta t)^2}\right]. \tag{A.34}$$

This completes the set of formulas needed to numerically evaluate $\Delta[d\Gamma/dx_q\,dy_{\bar{\rm Q}}]_{q\to q{\rm Q}\bar{\rm Q}}$.

[44] Eq. (A.34) above is $2\,{\rm Re}[\cdots]$ of the large-$N_{\rm f}$ QED to $N_{\rm f}{\gg}N_{\rm c}{\gg}1$ QCD generalization of the first line of eq. (E.21) of ref. [16]. Unlike the QED case shown there and in eq. (A.35) of ref. [16], we do not know how to do the integral analytically for the QCD case.

A.3 NLO corrections to single splitting $q \to qg$

We will decompose the contributions of figs. 18(h–n) to single splitting $q \to qg$ as

$$\left[\frac{\Delta\, d\Gamma}{dx_q}\right]^{\text{NLO}}_{q\to qg} = 2\,\text{Re}\Big\{\left[\frac{\Delta\, d\Gamma}{dx_q}\right]_{(\text{h+i+j})} + \left[\frac{d\Gamma}{dx_q}\right]_{(\text{k})} + \left[\frac{d\Gamma}{dx_q}\right]_{(\text{l})} + \left[\frac{d\Gamma}{dx_q}\right]_{(\text{m})} + \left[\frac{d\Gamma}{dx_q}\right]_{(\text{n})}\Big\}. \quad \text{(A.35)}$$

By back-end transformation [16],

$$2\,\text{Re}\left[\frac{\Delta\, d\Gamma}{dx_q}\right]_{(\text{h+i+j})} = -\int_0^{1-x_q} dy_{\text{Q}}\, \left[\frac{\Delta\, d\Gamma}{dx_q\, dy_{\text{Q}}}\right]_{\text{seq}}, \quad \text{(A.36)}$$

$$2\,\text{Re}\left[\frac{d\Gamma}{dx_q}\right]_{(\text{l})} = -\int_0^{1-x_q} dy_{\text{Q}}\, 2\,\text{Re}\left[\frac{d\Gamma}{dx_q\, dy_{\text{Q}}}\right]_{(\text{e})}, \quad \text{(A.37)}$$

$$2\,\text{Re}\left[\frac{d\Gamma}{dx_q}\right]_{(\text{n})} = 0, \quad \text{(A.38)}$$

where the integrands on the right-hand side are specified in (A.11), (A.31) and implicitly (A.33). By combined front- and back-end transformation [16],

$$2\,\text{Re}\left[\frac{d\Gamma}{dx_q}\right]_{(\text{m})} = +\int_0^{1-x_q} dy_{\text{Q}}\, \left\{2\,\text{Re}\left[\frac{d\Gamma}{dx_q\, dy_{\text{Q}}}\right]_{(\text{e})} \text{with } (x_q, y_{\text{Q}}, E) \to \left(\frac{-y_{\text{Q}}}{z_{\bar{\text{Q}}}}\,,\, \frac{-x_q}{z_{\bar{\text{Q}}}}\,,\, z_{\bar{\text{Q}}}E\right)\right\} \quad \text{(A.39)}$$

with $2\,\text{Re}[d\Gamma/dx_q\, dy_{\text{Q}}]_{(\text{e})}$ again given by (A.31).

Finally, diagram (k) gives

$$2\,\text{Re}\left[\frac{d\Gamma}{dx_q}\right]_{(\text{k})} = 2\,\text{Re}\Big\{-\frac{\beta_0\alpha_{\text{s}}}{2}\left[\frac{d\Gamma}{dx_q}\right]_{x\bar{x}}\left(\ln\Big(\frac{\mu^2}{(1-x_q)E\Omega_{\text{i}}\,\text{sgn}\,M_{\text{i}}}\Big) + \gamma_{\text{E}} - 2\ln 2 + \tfrac{5}{3}\right)\Big\}$$
$$+ \int_0^{1-x_q} dy_{\text{Q}}\, 2\,\text{Re}\left[\frac{d\Gamma}{dx_q\, dy_{\text{Q}}}\right]^{(\text{subtracted})}_{xyy\bar{x}}, \quad \text{(A.40)}$$

where the coefficient of the 1-loop renormalization group β-function for α_{s} is (in the large-N_{f} limit)

$$\beta_0 = \frac{2t_{\text{F}}N_{\text{f}}}{3\pi} \quad \text{(A.41)}$$

and

$$\left[\frac{d\Gamma}{dx_q}\right]_{x\bar{x}} = \frac{\alpha_{\text{s}}}{2\pi}\, P_{q\to q}(x_q)\, i\Omega_{\text{i}}\,\text{sgn}\,M_{\text{i}}. \quad \text{(A.42)}$$

is the $x\bar{x}$ diagram[45] from which $2\,\text{Re}[\cdots]$ gives the leading-order bremsstrahlung rate (A.4).

[45] $x\bar{x}$ refers to the naming convention for individual rate diagrams in fig. 31 of ref. [16].

The "subtracted" rate above is

$$\left[\frac{d\Gamma}{dx_q\,dy_{\bar{\mathrm{Q}}}}\right]^{(\text{subtracted})}_{xyy\bar{x}} = -t_{\mathrm{F}}C_{\mathrm{F}}\frac{N_{\mathrm{f}}\alpha_{\mathrm{s}}^2M_{\mathrm{i}}^2}{16\pi^4E^2}\,(-\hat{x}_1\hat{x}_2\hat{x}_3\hat{x}_4)\int_0^\infty d(\Delta t)\Bigg[\Omega_+\csc(\Omega_+\Delta t)\,\Omega_-\csc(\Omega_-\Delta t) \times\Big\{(\bar\beta Y_{\mathrm{y}}^2+\bar\gamma\overline{Y}_{\mathrm{yy}'}Y_{\mathrm{yy}'})I_0^{\mathrm{new}}+(2\bar\alpha+\bar\beta+\bar\gamma)Z_{\mathrm{yy}'}I_1^{\mathrm{new}} +\big[(\bar\alpha+\bar\gamma)Y_{\mathrm{y}}^2+(\bar\alpha+\bar\beta)\overline{Y}_{\mathrm{yy}'}Y_{\mathrm{yy}'}\big]I_2^{\mathrm{new}} -(\bar\alpha+\bar\beta+\bar\gamma)(\overline{Y}_{\mathrm{yy}'}Y_{\mathrm{y}}I_3^{\mathrm{new}}+Y_{\mathrm{y}}Y_{\mathrm{yy}'}I_4^{\mathrm{new}})\Big\} -(2\bar\alpha+\bar\beta+\bar\gamma)\frac{\hat{x}_2\hat{x}_3}{\hat{x}_1\hat{x}_4}\,\mathcal{D}_2^{(\mathbb{I})}\Bigg] \tag{A.43}$$

and

$$\mathcal{D}_2^{(\mathbb{I})}(\Delta t) = 2\pi^2\left[\frac{\ln(2i\Omega_{\mathrm{i}}\,\Delta t\,\mathrm{sgn}\,M_{\mathrm{i}})}{(\Delta t)^2}-i\Omega_{\mathrm{i}}^3\,\Delta t\csc^2(\Omega_{\mathrm{i}}\,\Delta t)\,\mathrm{sgn}\,M_{\mathrm{i}}\right]. \tag{A.44}$$

Here the I_n^{new} are the same as the I_n^{seq} of (A.19) except that the $(X,Y,Z)^{\mathrm{seq}}$ there are replaced by

$$\begin{pmatrix}X_{\mathrm{y}}^{\mathrm{new}} & Y_{\mathrm{y}}^{\mathrm{new}}\\ Y_{\mathrm{y}}^{\mathrm{new}} & Z_{\mathrm{y}}^{\mathrm{new}}\end{pmatrix}\equiv\begin{pmatrix}|M_{\mathrm{i}}|\Omega_{\mathrm{i}} & 0\\ 0 & 0\end{pmatrix}-ia_{\mathrm{y}}^{-1\top}\begin{pmatrix}\Omega_+\cot(\Omega_+\,\Delta t) & 0\\ 0 & \Omega_-\cot(\Omega_-\,\Delta t)\end{pmatrix}a_{\mathrm{y}}^{-1}, \tag{A.45a}$$

$$\begin{pmatrix}X_{\mathrm{y}'}^{\mathrm{new}} & Y_{\mathrm{y}'}^{\mathrm{new}}\\ Y_{\mathrm{y}'}^{\mathrm{new}} & Z_{\mathrm{y}'}^{\mathrm{new}}\end{pmatrix}\equiv\begin{pmatrix}X_{\mathrm{y}}^{\mathrm{new}} & Y_{\mathrm{y}}^{\mathrm{new}}\\ Y_{\mathrm{y}}^{\mathrm{new}} & Z_{\mathrm{y}}^{\mathrm{new}}\end{pmatrix}, \tag{A.45b}$$

$$\begin{pmatrix}X_{\mathrm{yy}'}^{\mathrm{new}} & Y_{\mathrm{yy}'}^{\mathrm{new}}\\ \overline{Y}_{\mathrm{yy}'}^{\mathrm{new}} & Z_{\mathrm{yy}'}^{\mathrm{new}}\end{pmatrix}\equiv-ia_{\mathrm{y}}^{-1\top}\begin{pmatrix}\Omega_+\csc(\Omega_+\,\Delta t) & 0\\ 0 & \Omega_-\csc(\Omega_-\,\Delta t)\end{pmatrix}a_{\mathrm{y}}^{-1}. \tag{A.45c}$$

The M's, Ω's and a's are as in section A.2.1 with (x_1,x_2,x_3,x_4) set to $(\hat{x}_1,\hat{x}_2,\hat{x}_3,\hat{x}_4)=(-1,y_{\bar{\mathrm{Q}}},1-x_q-y_{\bar{\mathrm{Q}}},x_q)$. The only reason that the factors of $\mathrm{sgn}\,M_{\mathrm{i}}$ in (A.40–A.44) are necessary is to accommodate the transformation of diagram (k) that will later be used to evaluate diagram (r).

The specific additive constants shown in (A.40) assume that the coupling α_{s} used in the leading-order calculation (A.4) of single splitting is $\alpha_{\mathrm{s}}(\mu)$ in the modified minimal subtraction ($\overline{\mathrm{MS}}$) scheme. To use a different renormalization scheme, one should convert (A.40) accordingly, but nothing else would change.

A.4 NLO corrections to single splitting $g\to\mathrm{Q}\bar{\mathrm{Q}}$

We decompose the contributions of figs. 18(o–u) to single splitting $g\to\mathrm{Q}\bar{\mathrm{Q}}$ as

$$\left[\frac{\Delta\,d\Gamma}{dy_{\bar{\mathrm{Q}}}}\right]^{\mathrm{NLO}}_{g\to\mathrm{Q}\bar{\mathrm{Q}}} = 2\,\mathrm{Re}\left\{\left[\frac{\Delta\,d\Gamma}{dy_{\bar{\mathrm{Q}}}}\right]_{(\mathrm{o+p+q})}+\left[\frac{d\Gamma}{dy_{\bar{\mathrm{Q}}}}\right]_{(\mathrm{r})}+\left[\frac{d\Gamma}{dy_{\bar{\mathrm{Q}}}}\right]_{(\mathrm{s})}+\left[\frac{d\Gamma}{dy_{\bar{\mathrm{Q}}}}\right]_{(\mathrm{t})}+\left[\frac{d\Gamma}{dy_{\bar{\mathrm{Q}}}}\right]_{(\mathrm{u})}\right\}. \tag{A.46}$$

By front-end transformation [16], modified as in section 3.1.2 of the current paper,

$$2\,\mathrm{Re}\left[\frac{\Delta\, d\Gamma}{dy_{\mathrm{Q}}}\right]_{(\mathrm{o+p+q})} = -\frac{d_{\mathrm{F}}}{d_{\mathrm{A}}}N_{\mathrm{f}}\int_0^1 dx_q \left\{\left[\frac{\Delta\, d\Gamma}{dx_q\, dy_{\mathrm{Q}}}\right]_{\mathrm{seq}} \text{ with (A.50) below}\right\}, \tag{A.47}$$

$$2\,\mathrm{Re}\left[\frac{d\Gamma}{dy_{\mathrm{Q}}}\right]_{(\mathrm{s})} = -\frac{d_{\mathrm{F}}}{d_{\mathrm{A}}}N_{\mathrm{f}}\int_0^1 dx_q \left\{2\,\mathrm{Re}\left[\frac{d\Gamma}{dx_q\, dy_{\mathrm{Q}}}\right]_{(\mathrm{f})} \text{ with (A.50) below}\right\}, \tag{A.48}$$

$$2\,\mathrm{Re}\left[\frac{d\Gamma}{dy_{\mathrm{Q}}}\right]_{(\mathrm{u})} = 0, \tag{A.49}$$

where

$$(x_q, y_{\mathrm{Q}}, E) \to \Big(\frac{-x_q}{1-x_q}\,,\ \frac{y_{\mathrm{Q}}}{1-x_q}\,,\ (1{-}x_q)E\Big). \tag{A.50}$$

By front- and back-end transformation [16],

$$2\,\mathrm{Re}\left[\frac{d\Gamma}{dy_{\mathrm{Q}}}\right]_{(\mathrm{t})} = \frac{d_{\mathrm{F}}}{d_{\mathrm{A}}}N_{\mathrm{f}}\int_0^1 dx_q \left\{2\,\mathrm{Re}\left[\frac{d\Gamma}{dx_q\, dy_{\mathrm{Q}}}\right]_{(\mathrm{f})} \text{with } (x_q, y_{\mathrm{Q}}, E) \to \Big(\frac{-(1{-}y_{\mathrm{Q}})}{y_{\mathrm{Q}}}, \frac{x_q}{y_{\mathrm{Q}}}, y_{\mathrm{Q}}E\Big)\right\}. \tag{A.51}$$

Finally, the result (A.40) for diagram (k) can be transformed to[46]

$$\begin{aligned}2\,\mathrm{Re}\left[\frac{d\Gamma}{dy_{\mathrm{Q}}}\right]_{(\mathrm{r})} &= 2\,\mathrm{Re}\Big\{-\frac{\beta_0\alpha_{\mathrm{s}}}{2}\left[\frac{d\Gamma}{dy_{\mathrm{Q}}}\right]_{y\bar{y}}^{g\to\mathrm{Q}\bar{\mathrm{Q}}}\Big(\ln\Big(\frac{\mu^2}{E\Omega_0^{g\to\mathrm{Q}\bar{\mathrm{Q}}}}\Big) - i\pi + \gamma_{\mathrm{E}} - 2\ln 2 + \tfrac{5}{3}\Big)\Big\}\\ &+ \frac{d_{\mathrm{F}}}{d_{\mathrm{A}}}N_{\mathrm{f}}\int_0^1 dx_q \left\{2\,\mathrm{Re}\left[\frac{d\Gamma}{dx_q\, dy_{\mathrm{Q}}}\right]_{xyy\bar{x}}^{(\text{subtracted})} \text{with } (x_q, y_{\mathrm{Q}}, E) \to \Big(\frac{-y_{\mathrm{Q}}}{1-y_{\mathrm{Q}}}, \frac{x_q}{1-y_{\mathrm{Q}}}, (1{-}y_{\mathrm{Q}})E\Big)\right\},\end{aligned} \tag{A.52}$$

where

$$\left[\frac{d\Gamma}{dy_{\mathrm{Q}}}\right]_{y\bar{y}} = \frac{N_{\mathrm{f}}\alpha_{\mathrm{s}}}{2\pi}\,P_{g\to q}(y_{\mathrm{Q}})\,i\Omega_0^{g\to\mathrm{Q}\bar{\mathrm{Q}}} \tag{A.53}$$

is the $y\bar{y}$ diagram from which $2\,\mathrm{Re}[\cdots]$ gives the leading-order pair production rate (A.7).

B $\ln x$ or $\ln(1{-}x)$ behavior in eqs. (4.7) for $f_{i\to j}(x)$

This appendix follows appendix B of ref. [17], which should be read first. That appendix discussed $\ln x$ and $\ln(1{-}x)$ behavior of the functions $f_{i\to j}(x)$ in the case of large-N_{f} QED. Here, we merely add to that discussion to explain where large-N_{f} QCD is different from large-N_{f} QED.

[46] See eq. (4.40) of ref. [16]. Also see appendix H of ref. [16] for technicalities on getting the first term in (A.52) from the transformation of (A.40). Also, we have not bothered to write any general $\mathrm{sgn}\,M$ factors in (A.52–A.53) that would allow this result to in turn be transformed back again to diagram (k). Instead, here we have just specialized to the specific values of $\mathrm{sgn}\,M$ of diagram (r).

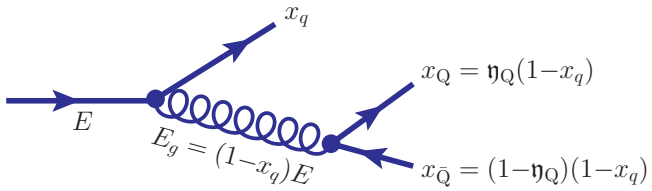

Figure 19. $q \to q\mathrm{Q}\bar{\mathrm{Q}}$ process

B.1 $q \to q\mathrm{Q}\bar{\mathrm{Q}}$

We start by looking at $f^{\text{real}}_{q\to q}(x)$ (4.11a) for real, overlapping splitting $q \to q\mathrm{Q}\bar{\mathrm{Q}}$. The notation we use is shown in fig. 19, where $E_g = (1-x_q)E$ and $\mathfrak{y}_{\mathrm{Q}} \equiv x_{\mathrm{Q}}/x_g = x_{\mathrm{Q}}/(1-x_q)$. The formation times for LO splittings $q \to qg$ and $g \to \mathrm{Q}\bar{\mathrm{Q}}$ with these energies are parametrically

$$t^{q\to qg}_{\text{form}} \sim \sqrt{\frac{x_q x_g E}{\hat{q}}} = \sqrt{\frac{x_q(1-x_q)E}{\hat{q}}}\,, \tag{B.1a}$$

$$t^{g\to \mathrm{Q}\bar{\mathrm{Q}}}_{\text{form}} \sim \sqrt{\frac{\mathfrak{y}_{\mathrm{Q}}\mathfrak{y}_{\bar{\mathrm{Q}}}E_g}{\hat{q}}} = \sqrt{\frac{\mathfrak{y}_{\mathrm{Q}}(1-\mathfrak{y}_{\mathrm{Q}})(1-x_q)E}{\hat{q}}}\,. \tag{B.1b}$$

B.1.1 $x_q \to 1$

In the limit $x_q \to 1$, (B.1) gives

$$t^{g\to \mathrm{Q}\bar{\mathrm{Q}}}_{\text{form}} \sim t^{q\to qg}_{\text{form}} \tag{B.2}$$

for democratic pair production (neither $\mathfrak{y}_{\mathrm{Q}}$ nor $1-\mathfrak{y}_{\mathrm{Q}}$ small). This is in stark contrast to the QED case where $t^{\gamma\to \mathrm{E}\bar{\mathrm{E}}}_{\text{form}} \ll t^{e\to e\gamma}_{\text{form}}$ in the same limit. It was this hierarchy that was responsible for the $\ln(1-x_e)$ behavior of $f^{\text{real}}_{e\to e}(x_e)$. Without a hierarchy, we do not expect such logarithms. (Formation time hierarchies generated when $\mathfrak{y}_{\mathrm{Q}} \to 0$ or $\mathfrak{y}_{\mathrm{Q}} \to 1$ do not matter because $\mathfrak{y}_{\mathrm{Q}}$ is integrated in the calculation of $f^{\text{real}}_{q\to q}(x_q)$, just as in the calculation of the $\ln(1-x_e)$ behavior in appendix B.1.1 of ref. [17].) We verify the absence of logarithmic behavior numerically in the log-linear plot of fig. 20b, which compares our numerical results for $f^{\text{real}}_{q\to q}(x_q)$ to a constant as $x\to 1$. The constant used in the plot is the value of our earlier fit (4.11a) evaluated at $x=1$.

B.1.2 $x_q \to 0$

In the limit $x_q \to 0$ with $\mathfrak{y}_{\mathrm{Q}}$ held fixed, (B.1) gives

$$t^{g\to \mathrm{Q}\bar{\mathrm{Q}}}_{\text{form}} \gg t^{q\to qg}_{\text{form}}, \tag{B.3}$$

which is the same hierarchy that was found for QED. Following the exact same analysis as in appendix B.1.2 of ref. [17] leads to exactly the same $\ln x_q$ term for QCD, shown in our eq. (4.11a) here. We check the logarithmic behavior by verifying that the slope of numerical

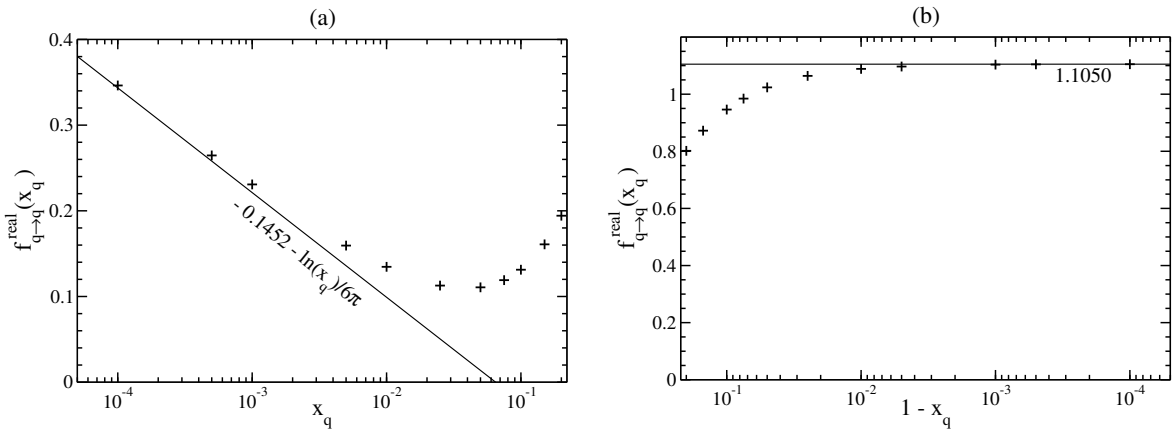

Figure 20. Log-linear plots of numerical results for $f^{\text{real}}_{q\to q}(x_q)$ vs. (a) x_q and (b) $1-x_q$. The numerical data points (+) are taken from table 2. The points are compared to (a) lines whose slopes on these plots correspond to the leading-log analytic results $-\frac{1}{6\pi}\ln x_q$ and (b) a constant (signifying no logarithmic behavior). Note that the horizontal axis in both plots is oriented so that $x_q \to 0$ is toward the left and $x_q \to 1$ is toward the right.

results in the log-linear plot of fig. 20a approaches the coefficient predicted for the logarithm in the limit $x_q \to 0$. Specifically, the line drawn for comparison shows the limiting $x_q{\to}0$ behavior of (4.11a),

$$f^{\text{real}}_{q\to q}(x) = -\tfrac{1}{6\pi}\ln x + \text{constant} \qquad \text{for } x \to 0. \tag{B.4}$$

B.1.3 $x_{\mathrm{Q}} \to 0$

The limit $x_{\mathrm{Q}} \to 0$ is dominated by $x_g \to 0$ with $x_{\mathrm{Q}} \sim x_{\bar{\mathrm{Q}}}$ as in (6.22). We then get no hierarchy of scales, as in (B.2), and so expect no $\ln x_{\mathrm{Q}}$ term in $f_{\underline{q\to \mathrm{Q}}}(x_{\mathrm{Q}})$. This is different than the behavior for QED. The absence of a logarithm is verified numerically in fig. 21a. Similarly, we expect no $\ln x_{\bar{\mathrm{Q}}}$ term in $f_{\underline{q\to \bar{\mathrm{Q}}}}(x_{\bar{\mathrm{Q}}})$.

B.1.4 $x_{\mathrm{Q}} \to 1$

This limit did not generate any $\ln(1{-}x_{\mathrm{E}})$ for $f_{\underline{e\to \mathrm{E}}}(x_{\mathrm{E}})$ in QED. The discussion of that case in ref. [17] is unaltered for QCD, which we've checked numerically in fig. 21b.

B.2 Virtual diagrams

Like ref. [17], we do not have a method for deducing *ab initio* the logarithmic behavior of $f_{\underline{i\to j}}$'s that contain virtual diagrams, and we rely on numerics to identify which limits lack any logarithmic terms $\ln x$ or $\ln(1{-}x)$. These are shown for various cases of $f_{\underline{q\to q}}$, $f_{\underline{q\to g}}$ and $f_{\underline{g\to \mathrm{Q}}}$ in fig. 21.

The one limit of an $f_{\underline{i\to j}}$ that is not shown in the figure is the $x{\to}1$ limit of $f_{\underline{q\to g}}(x)$. But this limit is already determined by using the relations (4.10) to rewrite the $x{\to}1$ limit of $f_{\underline{q\to g}}$

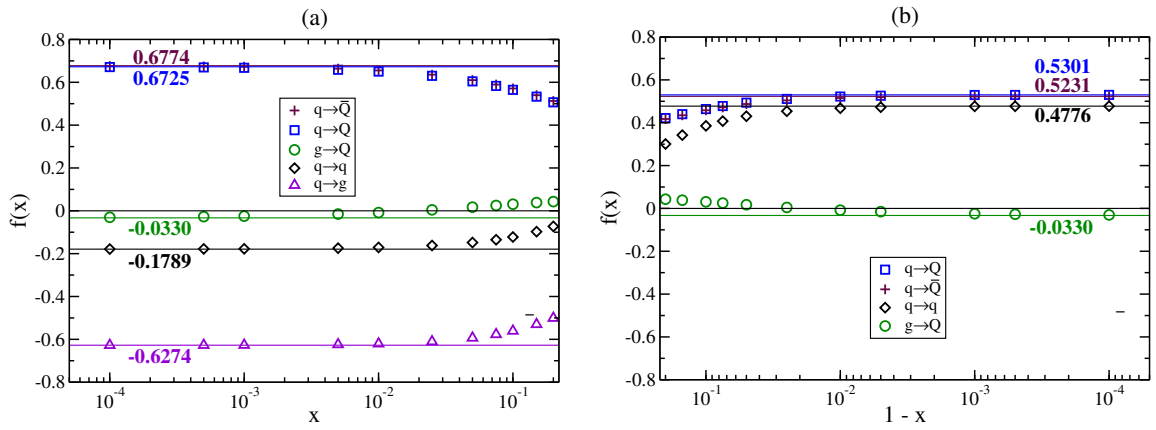

Figure 21. Like fig. 20 but here for a variety of $f_{\underline{i\to j}}(x)$ that show no log behavior for (a) $x \to 0$ or (b) $x \to 1$. Note that $g\to$Q data (which corresponds to NLO $g \to \mathrm{Q}\bar{\mathrm{Q}}$) are mirror reflections of each other in the two plots because of charge conjugation symmetry.

in terms of the $x\to 0$ limit of $f^{\rm virt}_{q\to q} = f_{\underline{q\to q}} - f^{\rm real}_{q\to q}$. Our previous results for the limits of $f_{\underline{q\to q}}$ and $f^{\rm real}_{q\to q}$ then give

$$f_{\underline{q\to g}}(x) \simeq \tfrac{1}{6\pi}\ln(1-x) + \text{constant} \qquad \text{for } x \to 1, \tag{B.5}$$

as in (4.7d).

C Qualitative picture for IR sensitivity of quark number deposition

In this appendix, we give a very qualitative argument about why the fermion-number deposition distribution $\phi_q(z)$ is IR sensitive in large-$N_{\rm f}$ QCD.

C.1 The picture

The staring point is the fact, apparent in table 2, that

$$\left[\frac{d\Gamma}{dx}\right]^{\rm net}_{\underline{q\to \mathrm{Q}}} \neq \left[\frac{d\Gamma}{dx}\right]^{\rm net}_{\underline{q\to \bar{\mathrm{Q}}}} \tag{C.1}$$

even in the small x limit. As discussed in section 6, these rates arise solely from overlapping $q\to qg\to q\mathrm{Q}\bar{\mathrm{Q}}$, and both rates scale like $x^{-3/2}$ for small x in the $\hat{q}$ approximation. A qualitative picture of the situation for $x \ll 1$ is shown by the solid curves in fig. 22. The blue solid curve for $q\to\bar{\mathrm{Q}}$ is drawn slightly above the red solid curve for $q\to\mathrm{Q}$ because table 2 shows that $q\to\bar{\mathrm{Q}}$ is the slightly larger rate at small x.

The $x^{-3/2}$ small-x behavior of the rates no longer applies when the $\hat{q}$ approximation breaks down for $x \lesssim x_{\rm IR}$ given by (6.18). The total integrated rate

$$\Gamma_{\underline{q\to \mathrm{Q}}} \equiv \int_0^1 dx \, \left[\frac{d\Gamma}{dx}\right]^{\rm net}_{\underline{q\to \mathrm{Q}}}, \tag{C.2}$$

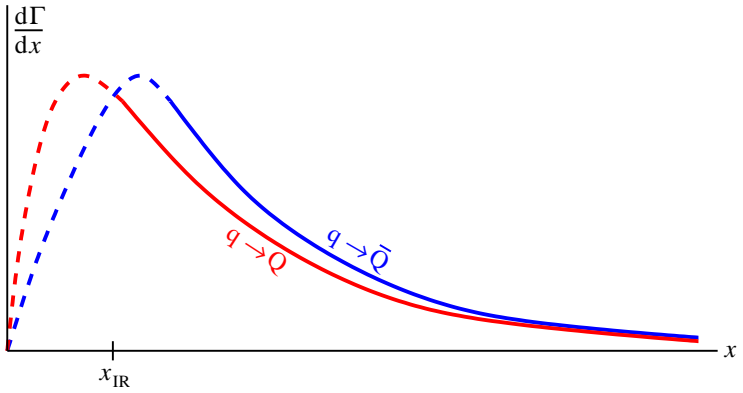

Figure 22. A schematic picture qualitatively comparing the behavior of $[d\Gamma/dx]^{\rm net}_{\underline{q\to \rm Q}}$ and $[d\Gamma/dx]^{\rm net}_{\underline{q\to \bar{\rm Q}}}$ in the small-x limit. The tails fall like $x^{-3/2}$. Details of this figure should not be taken seriously except for the takeaway that $\bar{\rm Q}$'s are statistically produced with a little more energy than Q's in overlapping $q{\to}qg{\to}q{\rm Q}\bar{\rm Q}$.

corresponding to the area beneath the red curve, would diverge in the $\hat{q}$ approximation because of the $x^{-3/2}$ behavior, but will be finite once IR physics is properly accounted for, as *schematically* depicted by the dashed red line in the figure. (We have made no attempt to think through the details of the shape of the $x \ll x_{\rm IR}$ behavior.) The total integrated rate $\Gamma_{\underline{q\to \rm Q}}$ for making a Q in overlapping $q{\to}qg{\to}q{\rm Q}\bar{\rm Q}$ must be the same as that for making a $\bar{\rm Q}$ (since one can't be made without the other), and so the areas under the red and blue curves in fig. 22 must be equal. This means that the red curve lies consistently to the left of the blue curve (as in the figure), and so, on average, the Q produced in overlapping $q{\to}qg{\to}q{\rm Q}\bar{\rm Q}$ will carry a bit less energy that then $\bar{\rm Q}$ that is produced with it.

Having slightly more energy, the $\bar{\rm Q}$ will travel slightly further through the medium than the Q before depositing its fermion number. A ${\rm Q}\bar{\rm Q}$ pair has no net fermion number and so, on net, will deposit none. But the fact that (statistically) the $\bar{\rm Q}$ goes a little further means that, as a function of time, the ${\rm Q}\bar{\rm Q}$ pair will (statistically) first deposit positive fermion number, with the canceling deposition of negative fermion number by $\bar{\rm Q}$ slightly later. Fig. 23 shows a schematic picture of the fermion number deposited by a soft ${\rm Q}\bar{\rm Q}$ pair that was produced at some position $z{=}z_0$ by overlapping $q{\to}qg{\to}q{\rm Q}\bar{\rm Q}$. The most common ${\rm Q}\bar{\rm Q}$ energies will be the softest ones ($x \sim x_{\rm IR}$). Quarks with energies of order $x_{\rm IR}E$ (where E is the energy of the original parent q) will stop in a distance of order

$$\Delta z \sim x_{\rm IR}^{1/2}\ell_0, \tag{C.3}$$

where ℓ_0 is the length scale (5.4) of a shower initiated by a particle of energy E. Crudely, one may think of the tick marks in fig. 23 as counting off intervals with sizes of order Δz.

To provide a simple visualization for the following argument, let's simplify and abstract fig. 23 (at various positions z_0) by the graphs on the left-hand side of fig. 24. In this figure, $z{=}0$

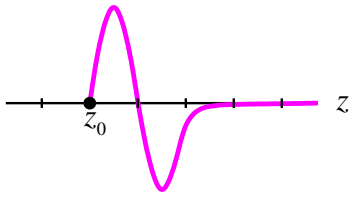

Figure 23. A schematic picture of the deposition of fermion number from a soft $Q\bar{Q}$ created at $z{=}z_0$ by overlapping $q{\to}qg{\to}q Q\bar{Q}$. Details of this picture should not be taken seriously except for the fact that, in this particular situation, $\bar{Q}$ deposition occurs (statistically) a little further away from the pair creation than Q deposition does.

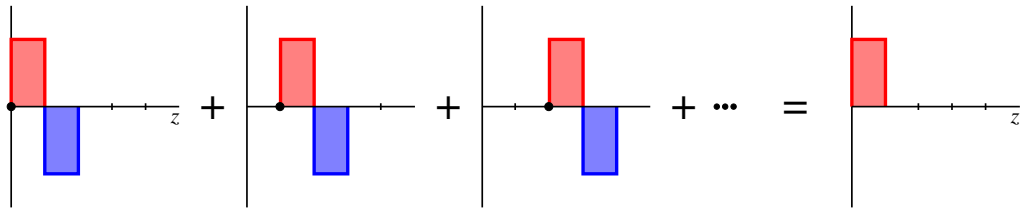

Figure 24. The left-hand side of the above equation schematically represents the possibilities that a single, overlapping $q{\to}qg{\to}q Q\bar{Q}$ (represented by the black dot) might occur at different early times $z_0 \geq 0$, and the right-hand side represents the resulting average fermion-number deposition $\phi_q(z)$ at early times ($0 \leq z \ll \ell_0$).

represents the starting position of the original high-energy q of energy E. Since overlapping $q{\to}qg{\to}q Q\bar{Q}$ is a NLO effect, and since we formally expand to first order in $N_{\rm f}\alpha_{\rm s}$ in our treatment of shower development, there will only be one overlapping splitting in the entire development of the shower, and that one NLO splitting can happen at any random time. We will focus on the case where it happens early in the shower, at some $z \ll \ell_0$. The first three graphs in fig. 24 crudely represent the cases where it happens at $z \simeq 0$, $z \simeq \Delta z$, and $z \simeq 2\Delta z$. These have equal probability, and so we should add them up (imagining that that probability is already included in the normalization of the vertical axis) to get the final, statistically averaged, fermion-number deposition distribution for $z \ll \ell_0$. As can be seen visually in our cartoon (fig. 24), there is a cancellation, in all intervals beyond the first, between the chance that (i) a Q emitted previously deposits its fermion number there and (ii) a $\bar{Q}$ emitted even earlier deposits its fermion number there. The only place where this cancellation cannot happen (for $z \ll \ell_0$) is the first interval of size Δz. So, the average fermion-number distribution deposited by the $Q\bar{Q}$ pairs is peaked at very early positions $z \sim \Delta z \ll \ell_0$.

Of course, the times when the overlapping $q{\to}qg{\to}q Q\bar{Q}$ might have happened are continuous, not discrete, and a curve like fig. 23 is also not the same thing as the square pulse curves shown in fig. 24. But one will get the same qualitative result by averaging any curve like fig. 23 continuously over the location, from $z{=}0$ onward, of its starting point z_0.

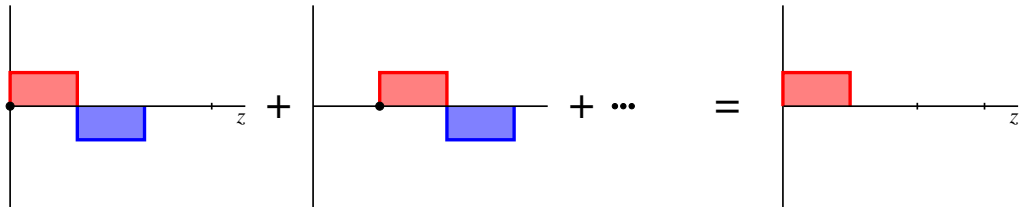

Figure 25. Like fig. 24 but representing the smaller probabilities of overlapping $q{\to}qg{\to}q\mathrm{Q}\bar{\mathrm{Q}}$ when the $\mathrm{Q}\bar{\mathrm{Q}}$ pair has enough energy that the Q's and $\bar{\mathrm{Q}}$'s take twice as long to stop.

Parametrically, how large is the short-time fermion-number deposition represented by the right-hand side of fig. 24? The rate for soft overlapping $q{\to}qg{\to}q\mathrm{Q}\bar{\mathrm{Q}}$ with $x \sim x_{\mathrm{IR}}$ is

$$\mathrm{rate}(x_{\mathrm{IR}}) \sim x_{\mathrm{IR}} \times \left[\frac{d\Gamma}{dx}(x_{\mathrm{IR}})\right]^{\mathrm{NLO}}_{\underline{q\to\mathrm{Q}}} \sim \frac{N_{\mathrm{f}}\alpha_{\mathrm{s}}}{x_{\mathrm{IR}}^{1/2}\ell_0}\,. \tag{C.4a}$$

The chance that it happens in the first interval Δz is

$$\mathrm{Prob}(x_{\mathrm{IR}}) \sim \mathrm{rate}(x_{\mathrm{IR}}) \times \Delta z \sim N_{\mathrm{f}}\alpha_{\mathrm{s}}. \tag{C.4b}$$

When it does happen, the fermion number deposited in the first interval is $O(1)$. So, on average, the far right-hand side of fig. 24 represents very early deposition of fermion number of order $N_{\mathrm{f}}\alpha_{\mathrm{s}} \ll 1$.

This is certainly an IR-sensitive feature of the deposition distribution $\phi_q(z)$ at NLO. However, the story so far does not explain the logarithmic enhancement to NLO corrections that we found in section 6.2. That's because the discussion so far has focused only on the most common case of overlapping $q{\to}qg{\to}q\mathrm{Q}\bar{\mathrm{Q}}$, which is the softest possible pair production ($x \sim x_{\mathrm{IR}}$). But now imagine rarer $q{\to}qg{\to}q\mathrm{Q}\bar{\mathrm{Q}}$ with $x \sim x_1$ where $x_{\mathrm{IR}} \ll x_1 \ll 1$. Though still soft compared to the original q, the Q and $\bar{\mathrm{Q}}$ will now have more energy than before and so will go further than before. The analog of fig. 24 will now look like fig. 25 (where we've made the distances only twice as long so that the figure still fits easily on the page). All of the above estimates (C.4) still go through, but with the scale x_{IR} replaced by the scale x_1. So $x \sim x_1$ contributes an additional $N_{\mathrm{f}}\alpha_{\mathrm{s}}$ to early deposition of fermion number; it's just more spread out than the $x \sim x_{\mathrm{IR}}$ contribution. Roughly speaking, there should be a contribution of $N_{\mathrm{f}}\alpha_{\mathrm{s}}$ for every distinct choice of scale $x \sim x_1$ with $x_{\mathrm{IR}} \ll x_1 \ll 1$, which means a logarithmic enhancement $\approx \ln(1/x_{\mathrm{IR}})$.

Allowing for contributions from all x scales, the early deposition of fermion number from soft, overlapping $q{\to}qg{\to}q\mathrm{Q}\bar{\mathrm{Q}}$ will be

$$\phi_q(z) \sim \frac{N_{\mathrm{f}}\alpha_{\mathrm{s}}}{z} \quad \text{for } \Delta z \ll z \ll \ell_0. \tag{C.5}$$

The integral of $\phi_q(z)$ over early times $z \ll \ell_0$ is parametrically $N_{\mathrm{f}}\alpha_{\mathrm{s}}\ln(1/x_{\mathrm{IR}})$, which is the early-time fermion number deposition. By conservation of fermion number, $O\big(N_{\mathrm{f}}\alpha_{\mathrm{s}}\log\big)$

fermion number deposited early in the shower ($z \ll \ell_0$) means that fermion number $1 - O\big(N_{\rm f}\alpha_{\rm s}\log\big)$ must be deposited at $z \sim \ell_0$. One crude way to picture this is to imagine that we suddenly turned off the production of $\mathrm{Q}\bar{\mathrm{Q}}$ pairs at some large time in figs. 24 and 25. Then there would be a deposition (on average) of negative fermion number by $\bar{\mathrm{Q}}$ at the very end, in addition to the deposition 1 by the original quark q that initiated the shower.

Like the main text, we will not attempt to sort out the case where $N_{\rm f}\alpha_{\rm s}\ln(1/x_{\rm IR}) \gg 1$.

C.2 Relation to moments $\langle z^n\rangle$

In section 6, the infrared logarithm arose when calculating the recursion relation for moments $\langle z^n\rangle$. We now discuss how that is related to the form (C.5) of the early time deposition.

But first, we examine more thoroughly how the infrared logarithm affected the recursion relation for $\langle z^n\rangle$. The logarithm arose in the calculation of $\mathcal{M}_n$ for the specific case n=1 of (6.10b). The recursion relation (6.10a) gives

$$\langle z^n\rangle_\phi = \frac{n!}{\mathcal{M}_n\mathcal{M}_{n-1}\cdots\mathcal{M}_1}\,, \tag{C.6}$$

where all factors are infrared-safe except for $\mathcal{M}_1$. So, the IR sensitivity of all of the $\langle z^n\rangle$ arise from the same common overall factor

$$\frac{1}{\mathcal{M}_1} \propto \frac{1}{1+O\big(N_{\rm f}\alpha_{\rm s}\ln(1/x_{\rm IR})\big)} = 1 - O\big(N_{\rm f}\alpha_{\rm s}\ln(1/x_{\rm IR})\big). \tag{C.7}$$

To help understand this result, we now qualitatively argue for a common factor like (C.7) starting instead from the early-time behavior (C.5) of $\phi_q(z)$. Imagine calculating the moments

$$\langle z^n\rangle = \int_0^\infty dz\; z^n\phi_q(z) \tag{C.8}$$

directly from $\phi_q(z)$ for all $n\geq$1. The early-time behavior (C.5) generates no infrared logarithm from the early-time ($z\ll\ell_0$) portion of the integrals (C.8). The IR-sensitive corrections to moments instead arises indirectly from the fact that early-time deposition (C.5) leaves only total fermion number $1 - O\big(N_{\rm f}\alpha_{\rm s}\log\big)$ remaining to be deposited at late times $z \sim \ell_0$. That means that $\phi_q(z)$ will be proportional to $1 - O\big(N_{\rm f}\alpha_{\rm s}\log\big)$ at late times, which introduces a common IR-sensitive correction to the $z\sim\ell_0$ part of the integrals (C.8) for the moments $\langle z^n\rangle$.

D $x_{\rm Q}\leftrightarrow x_{\bar{\rm Q}}$ behavior of overlapping $q\to qg\to q\mathrm{Q}\bar{\mathrm{Q}}$ in soft gluon limit

In section 6.3, we reported that one can check numerically that the diagrams contributing to the rate $[\Delta\, d\Gamma/dx_q\, x_{\rm Q}]_{q\to q\mathrm{Q}\bar{\mathrm{Q}}}$ are all individually symmetric or anti-symmetric under

$$x_{\rm Q} \leftrightarrow x_{\bar{\rm Q}} = 1 - x_q - x_{\rm Q} \tag{D.1}$$

in the limit

$$x_{\rm Q} \sim x_{\bar{\rm Q}} \ll 1, \tag{D.2}$$

and that the diagrams which are anti-symmetric are the rate diagrams of fig. 13, which are characterized by having a single longitudinal gluon exchange. [In the full set of diagrams shown in fig. 18, the ones that contribute to real double splitting $q{\to}qg{\to}q\mathrm{Q}\bar{\mathrm{Q}}$ are diagrams (a–g), those that have a single longitudinal exchange are (e–g), and diagram (g) evaluates to zero.] The purpose of this appendix is to briefly sketch an explanation of these symmetry properties. We will compare and contrast this situation to the discussion of large-N_f QED.

D.1 4-body Hamiltonian

D.1.1 QED

Let's start with QED. The critical starting point for the symmetry argument in appendix A of ref. [17] was the effective 2-particle Hamiltonian for 4-body $(\bar{e},\mathrm{E},\bar{\mathrm{E}},e)$ evolution, which was

$$\frac{P_{41}^2}{2x_1x_4(x_1{+}x_4)E}+\frac{P_{23}^2}{2x_2x_3(x_2{+}x_3)E}-\frac{i\hat{q}}{4}(x_1{+}x_4)^2\,(\boldsymbol{C}_{41}-\boldsymbol{C}_{23})^2 \qquad \text{(QED)} \tag{D.3}$$

in the basis $(\boldsymbol{C}_{41},\boldsymbol{C}_{23})$ most convenient for the evaluation of large-N_f diagrams. Above, $(x_1,x_2,x_3,x_4)=(-1,x_\mathrm{E},x_{\bar{\mathrm{E}}},x_e)$. This Hamiltonian is exactly symmetric under the exchange of the values of x_2 and x_3, which corresponds to (D.1). From there, ref. [17] argued that all large-N_f QED diagrams were symmetric under exchanging $x_\mathrm{E}\leftrightarrow x_{\bar{\mathrm{E}}}$.

D.1.2 $N_\mathrm{c}{\gg}1$ QCD

For $N_\mathrm{c}{\gg}1$ QCD, we earlier presented the effective 2-particle Hamiltonian for 4-body $(\bar{q},\mathrm{Q},\bar{\mathrm{Q}},q)$ evolution in eqs. (3.14) and (3.15) but so far only in the basis $(\boldsymbol{C}_{34},\boldsymbol{C}_{12})$. We then found the normal modes and only then switched to the $(\boldsymbol{C}_{41},\boldsymbol{C}_{23})$ basis convenient to the evaluation of the large-N_f diagrams. Here, let us instead make this change of basis[47] directly to the Hamiltonian (3.15), which then becomes

$$\mathcal{H}_4=\frac{P_{41}^2}{2x_1x_4(x_1{+}x_4)E}+\frac{P_{23}^2}{2x_2x_3(x_2{+}x_3)E}-V_4(\boldsymbol{C}_{41},\boldsymbol{C}_{23}) \tag{D.4}$$

with

$$V_4(\boldsymbol{C}_{41},\boldsymbol{C}_{23})=-\frac{i\hat{q}_\mathrm{F}}{4}\big[(x_2^2{+}x_3^2)C_{23}^2+2(x_1x_2{+}x_3x_4)\boldsymbol{C}_{23}\cdot\boldsymbol{C}_{41}+(x_1^2{+}x_4^2)C_{41}^2\big]. \tag{D.5}$$

The kinetic terms (which are the same as in the QED case) are symmetric under $x_2\leftrightarrow x_3$, but the potential is not. But now remember that

$$(x_1,x_2,x_3,x_4)=(-1,x_\mathrm{Q},x_{\bar{\mathrm{Q}}},x_q)=(-1,x_\mathrm{Q},x_{\bar{\mathrm{Q}}},1{-}x_\mathrm{Q}{-}x_{\bar{\mathrm{Q}}}). \tag{D.6}$$

[47] By cyclic permutation of the particle numbers (1,2,3,4) to (4,1,2,3), eqs. (3.23) and (3.24a) give $\boldsymbol{C}_{34}=(-x_2\boldsymbol{C}_{23}-x_1\boldsymbol{C}_{41})/(x_3+x_4)$ and $\boldsymbol{C}_{12}=(x_3\boldsymbol{C}_{23}+x_4\boldsymbol{C}_{41})/(x_3+x_4)$. (This is equivalent to, but much quicker than, explicitly computing $\mathcal{S}^{-1}$ and then tediously simplifying using $x_1{+}x_2{+}x_3{+}x_4=0$.)

Then, taking the soft limit (D.2) while avoiding any particular assumption about the relative sizes of C_{23} and C_{41},

$$V_4(\boldsymbol{C}_{41}, \boldsymbol{C}_{23}) \simeq -\frac{i\hat{q}_\mathrm{F}}{4}\big[(x_2^2{+}x_3^2)C_{23}^2 + 2(x_3{-}x_2)\boldsymbol{C}_{23}\cdot\boldsymbol{C}_{41} + 2C_{41}^2\big]. \tag{D.7}$$

This soft limit is still not symmetric under $x_2 \leftrightarrow x_3$ because the $(x_3{-}x_2)\boldsymbol{C}_{23}\cdot\boldsymbol{C}_{41}$ term is anti-symmetric. But we can make the following useful observation regarding the 4-body potential:

> In the soft limit (D.2), exchanging $x_2 \leftrightarrow x_3$ is equivalent to leaving x_2 and x_3 unchanged but replacing $\boldsymbol{C}_{23}$ by $\boldsymbol{C}_{32} = -\boldsymbol{C}_{23}$.

For consistency, the corresponding conjugate momentum $\boldsymbol{P}_{23}$ should then also be replaced by $\boldsymbol{P}_{32} = -\boldsymbol{P}_{23}$, but this has no effect on the Hamiltonian (D.4).

D.1.3 $N_\mathrm{c}\gg 1$ QCD with less algebra

There's an alternate way to arrive at the last conclusion with less algebra but a little more qualitative argument about scales in the soft limit. Start from the original form (3.12) of the 4-body potential in terms of the four transverse positions $\boldsymbol{b}_i$:

$$V_4(\boldsymbol{b}_1, \boldsymbol{b}_2, \boldsymbol{b}_3, \boldsymbol{b}_4) = -\frac{i\hat{q}_\mathrm{F}}{4}\left[(\boldsymbol{b}_2{-}\boldsymbol{b}_1)^2 + (\boldsymbol{b}_4{-}\boldsymbol{b}_3)^2\right]. \tag{D.8}$$

In the soft limit $x_2 \sim x_3 \ll 1$ of (D.2), particles 1 and 4 will have relatively high energy and so collisions with the medium will not deflect them significantly compared to particles 2 and 3. So the sizes of $\boldsymbol{b}_1$ and $\boldsymbol{b}_4$ will be negligible compared to the sizes of $\boldsymbol{b}_2$ and $\boldsymbol{b}_3$. So we may approximate (D.8) as

$$V_4(\boldsymbol{b}_1, \boldsymbol{b}_2, \boldsymbol{b}_3, \boldsymbol{b}_4) \simeq -\frac{i\hat{q}_\mathrm{F}}{4}(b_2^2 + b_3^2). \tag{D.9}$$

The corresponding kinetic terms of the quantum mechanics problem, coming from the $p_\perp^2$ terms in the high-energy expansion of $|\boldsymbol{p}_i| \simeq p_{z,i} + p_{\perp,i}^2/p_{z,i}$, then give a Hamiltonian

$$H_4 \simeq \frac{p_{\perp,2}^2}{2x_2E} + \frac{p_{\perp,3}^2}{2x_3E} - \frac{i\hat{q}_\mathrm{F}}{4}(b_2^2 + b_3^2) \tag{D.10}$$

in this language. For that Hamiltonian, exchanging the values of x_2 and x_3 is equivalent to exchanging $(\boldsymbol{b}_2, \boldsymbol{p}_{\perp,2})$ with $(\boldsymbol{b}_3, \boldsymbol{p}_{\perp,3})$. Because $\boldsymbol{C}_{ij} \equiv (\boldsymbol{b}_i{-}\boldsymbol{b}_j)/(x_i{+}x_j)$ (with conjugate momentum $\boldsymbol{P}_{ij} = x_j\boldsymbol{p}_{\perp,i} - x_i\boldsymbol{p}_{\perp,j}$), that's equivalent to negating $\boldsymbol{C}_{23}$ (and $\boldsymbol{P}_{23}$), as found previously.

D.2 Diagrams

Let's start with (the QCD version of) the diagram of fig. 18a. Following the related analysis of large-N_f QED in appendix A of ref. [17], we note that the formula for this diagram was

originally derived from a formula of the form[48]

$$\begin{aligned}&(\text{splitting amplitude factors from the vertices}) \times \frac{N_{\rm f}\alpha^2}{(x_1{+}x_4)^2}\int_{\rm times}\int_{\boldsymbol{B}',\boldsymbol{B}''}\\ &\quad\times \boldsymbol{\nabla}_{\boldsymbol{B}'''}\langle \boldsymbol{B}''', t'''|\boldsymbol{B}'', t''\rangle\Big|_{\boldsymbol{B}'''=0}\\ &\quad\times \boldsymbol{\nabla}_{\boldsymbol{C}''_{41}}\boldsymbol{\nabla}_{\boldsymbol{C}'_{23}}\langle \boldsymbol{C}''_{41},\boldsymbol{C}''_{23},t''|\boldsymbol{C}'_{41},\boldsymbol{C}'_{23},t'\rangle\Big|_{\boldsymbol{C}''_{41}=0=\boldsymbol{C}'_{23};\ \boldsymbol{C}''_{23}=\boldsymbol{B}'';\ \boldsymbol{C}'_{41}=\boldsymbol{B}'}\\ &\quad\times \boldsymbol{\nabla}_{\boldsymbol{B}}\langle \boldsymbol{B}', t'|\boldsymbol{B}, t\rangle\Big|_{\boldsymbol{B}=0}.\end{aligned} \tag{D.11}$$

Above, the $\langle \boldsymbol{C}''_{41},\boldsymbol{C}''_{23},t''|\boldsymbol{C}'_{41},\boldsymbol{C}'_{23},t'\rangle$ is the propagator associated with the 4-body Hamiltonian $\mathcal{H}_4$. The other two $\langle\cdots\rangle$'s are similar factors for the initial and final 3-particle evolution, with time running from right to left in the formula ($t<t'<t''<t'''$). The derivatives $\boldsymbol{\nabla}$ are position-space versions of transverse momentum factors associated with the vertices. We will not need to discuss the somewhat complicated details of how the splitting-amplitude vertex factors contract those derivatives with each other.

By our previous discussion of $\mathcal{H}_4$, exchanging $x_{\rm Q}\leftrightarrow x_{\bar{\rm Q}}$ in the soft limit (D.2) will be equivalent to replacing $\boldsymbol{C}_{23}$ by $-\boldsymbol{C}_{23}$ in the 4-body propagator:

$$\langle \boldsymbol{C}''_{41},\boldsymbol{C}''_{23},t''|\boldsymbol{C}'_{41},\boldsymbol{C}'_{23},t'\rangle \to \langle \boldsymbol{C}''_{41},-\boldsymbol{C}''_{23},t''|\boldsymbol{C}'_{41},-\boldsymbol{C}'_{23},t'\rangle. \tag{D.12}$$

The Hamiltonian for the initial 3-body evolution is

$$\mathcal{H}_{3,i} = \frac{P_\perp^2}{2M_{\rm i}} + \tfrac{1}{2}M_{\rm i}\Omega_{\rm i}^2 B^2 \tag{D.13}$$

with $M_{\rm i}$ and $\Omega_{\rm i}$ given by (3.8), which only depend on $x_{\rm Q}$ and $x_{\bar{\rm Q}}$ through the symmetric combination $x_g = x_{\rm Q}{+}x_{\bar{\rm Q}} = 1{-}x_q$, and so $\langle \boldsymbol{B}', t'|\boldsymbol{B}, t\rangle$ is unchanged. Similarly, the Hamiltonian for the final 3-body evolution is

$$\mathcal{H}_{3,f} = \frac{P_\perp^2}{2M_{\rm f}^{\rm seq}} + \tfrac{1}{2}M_{\rm f}^{\rm seq}(\Omega_{\rm f}^{\rm seq})^2 B^2 \tag{D.14}$$

with $M_{\rm f}^{\rm seq}$ and $\Omega_{\rm f}^{\rm seq}$ given by (3.27), which again are symmetric in $x_{\rm Q}\leftrightarrow x_{\bar{\rm Q}}$. So $\langle \boldsymbol{B}''', t'''|\boldsymbol{B}'', t''\rangle$ is also unchanged.

Now focus on the first two factors of the integrand in (D.11). The only change is (D.12), and so those two factors becomes

$$\begin{aligned}&\boldsymbol{\nabla}_{\boldsymbol{B}'''}\langle \boldsymbol{B}''', t'''|\boldsymbol{B}'', t''\rangle\Big|_{\boldsymbol{B}'''=0}\\ &\quad\times \boldsymbol{\nabla}_{\boldsymbol{C}''_{41}}\boldsymbol{\nabla}_{\boldsymbol{C}'_{23}}\langle \boldsymbol{C}''_{41},-\boldsymbol{C}''_{23},t''|\boldsymbol{C}'_{41},-\boldsymbol{C}'_{23},t'\rangle\Big|_{\boldsymbol{C}''_{41}=0=\boldsymbol{C}'_{23};\ \boldsymbol{C}''_{23}=\boldsymbol{B}'';\ \boldsymbol{C}'_{41}=\boldsymbol{B}'}\end{aligned} \tag{D.15}$$

[48] Specifically, see eq. (A.3) of ref. [17]. That's taken from eq. (E.1) of ref. [21], with the QED modifications described in appendices E.1 and E.2 of ref. [16], followed here by the QCD modifications described in this paper.

and nothing else changes. Mathematically, $\boldsymbol{C}'_{23}$ and $\boldsymbol{C}''_{23}$ are just dummy variable names in the above expression since at the end they are set to zero and $\boldsymbol{B}''$ respectively, and so we could call them anything. So switch variables by defining new symbols $\boldsymbol{C}'_{23}$ and $\boldsymbol{C}''_{23}$ that are the negative of what they were previously. The factors (D.15) are therefore equal to the expression

$$\begin{aligned}
&-\boldsymbol{\nabla}_{\boldsymbol{B}'''}\langle \boldsymbol{B}''', t'''|\boldsymbol{B}'', t''\rangle\Big|_{\boldsymbol{B}'''=0} \\
&\qquad\times \boldsymbol{\nabla}_{\boldsymbol{C}''_{41}}\boldsymbol{\nabla}_{\boldsymbol{C}'_{23}}\langle \boldsymbol{C}''_{41}, \boldsymbol{C}''_{23}, t''|\boldsymbol{C}'_{41}, \boldsymbol{C}'_{23}, t'\rangle\Big|_{\boldsymbol{C}''_{41}=0=\boldsymbol{C}'_{23};\ \boldsymbol{C}''_{23}=-\boldsymbol{B}'';\ \boldsymbol{C}'_{41}=\boldsymbol{B}'}
\end{aligned} \tag{D.16}$$

where the overall minus sign came from the change of variable on $\boldsymbol{\nabla}_{\boldsymbol{C}'_{23}}$, and $\boldsymbol{C}''_{23}$ is now set to $-\boldsymbol{B}''$ instead of to $\boldsymbol{B}''$. Next, change integration variables $\boldsymbol{B}'' \to -\boldsymbol{B}''$ in (D.11). By parity invariance in the transverse plane, $\langle \boldsymbol{B}''', t'''|\boldsymbol{B}'', t''\rangle$ would be invariant under parity but $\boldsymbol{\nabla}_{\boldsymbol{B}'''}\langle \boldsymbol{B}''', t'''|\boldsymbol{B}'', t''\rangle\Big|_{\boldsymbol{B}'''=0}$ will negate. The factors (D.16) are then equal to what they were in (D.11) before we exchanged x_{Q} and $x_{\bar{\mathrm{Q}}}$. Overall, we picked up one minus sign from the $\boldsymbol{\nabla}_{\boldsymbol{C}'_{23}}$ and a canceling minus sign from the $\boldsymbol{\nabla}_{\boldsymbol{B}'''}$ (because $\boldsymbol{B}'''$ was connected to $\boldsymbol{B}''$ which was connected to $\boldsymbol{C}''_{23}$). The takeaway is that (D.11) is symmetric under $x_{\mathrm{Q}} \leftrightarrow x_{\bar{\mathrm{Q}}}$ in the soft limit.

Now consider instead diagram (e) of fig. 18, which has a single longitudinal gluon exchange. The structure analogous to (D.11) is[49]

$$\begin{aligned}
&(\text{splitting amplitude factors from the vertices}) \times \frac{N_{\mathrm{f}}\alpha^2}{(x_1+x_4)^2}\int_{\text{times}}\int_{\boldsymbol{B}''} \\
&\qquad\times \boldsymbol{\nabla}_{\boldsymbol{B}'''}\langle \boldsymbol{B}''', t'''|\boldsymbol{B}'', t''\rangle\Big|_{\boldsymbol{B}'''=0} \\
&\qquad\times \boldsymbol{\nabla}_{\boldsymbol{C}''_{41}}\langle \boldsymbol{C}''_{41}, \boldsymbol{C}''_{23}, t''|\boldsymbol{C}'_{41}, \boldsymbol{C}'_{23}, t'\rangle\Big|_{\boldsymbol{C}''_{41}=0=\boldsymbol{C}'_{23};\ \boldsymbol{C}''_{23}=\boldsymbol{B}'';\ \boldsymbol{C}'_{41}=0}
\end{aligned} \tag{D.17}$$

with $t' < t'' < t'''$. If we follow the same steps as we did for (D.15), we will only get one minus sign from $x_{\mathrm{Q}} \leftrightarrow x_{\bar{\mathrm{Q}}}$ (in the soft limit) because there is no $\boldsymbol{\nabla}_{\boldsymbol{C}'_{23}}$ in this expression. That's because longitudinal gluon exchange does not come with a factor of transverse momentum.

Similarly, diagram (f) works out to be anti-symmetric. Diagrams (b–c) do not involve any region of 4-body evolution, which is what caused potential difficulties, and so they are symmetric. Diagram (g) evaluates to zero and so is irrelevant. Diagram (d), which has two longitudinal gluon exchanges, has the form[50]

$$\begin{aligned}
&(\text{splitting amplitude factors from the vertices}) \times \frac{N_{\mathrm{f}}\alpha^2}{(x_1+x_4)^2} \\
&\qquad\times \langle \boldsymbol{C}''_{41}, \boldsymbol{C}''_{23}, t''|\boldsymbol{C}'_{41}, \boldsymbol{C}'_{23}, t'\rangle\Big|_{\boldsymbol{C}''_{41}=0=\boldsymbol{C}'_{23};\ \boldsymbol{C}''_{23}=0;\ \boldsymbol{C}'_{41}=0}.
\end{aligned} \tag{D.18}$$

There are no vertices that generate transverse momentum factors and so no transverse position gradients. So this diagram is symmetric.

[49] See eq. (E24) of ref. [16].

[50] See eq. (3.11) of ref. [32], adapted to longitudinal gluon exchange between fermion lines as discussed in appendix E.3.1 of ref. [16].

D.3 More details regarding rate formulas

For any reader wishing to see how the symmetry and anti-symmetry manifest in the final rate formulas given in appendix A.2, we offer an observation here about the symmetry of some of the more complicated elements of those formulas. Refs. [16, 21] define a variety of symbols by writing the harmonic oscillator propagator for the 4-body evolution in the form[51]

$$\begin{aligned}\langle \boldsymbol{C}_{41}^{\bar{\mathrm{x}}}, \boldsymbol{C}_{23}^{\bar{\mathrm{x}}}, t_{\bar{\mathrm{x}}} | \boldsymbol{C}_{41}^{\mathrm{y}}, \boldsymbol{C}_{23}^{\mathrm{y}}, t_{\mathrm{y}} \rangle \propto \\ \exp\left[-\frac{1}{2} \begin{pmatrix} \boldsymbol{C}_{41}^{\mathrm{y}} \\ \boldsymbol{C}_{23}^{\mathrm{y}} \end{pmatrix}^{\top} \begin{pmatrix} \mathcal{X}_{\mathrm{y}}^{\mathrm{seq}} & Y_{\mathrm{y}}^{\mathrm{seq}} \\ Y_{\mathrm{y}}^{\mathrm{seq}} & Z_{\mathrm{y}}^{\mathrm{seq}} \end{pmatrix} \begin{pmatrix} \boldsymbol{C}_{41}^{\mathrm{y}} \\ \boldsymbol{C}_{23}^{\mathrm{y}} \end{pmatrix} - \frac{1}{2} \begin{pmatrix} \boldsymbol{C}_{23}^{\bar{\mathrm{x}}} \\ \boldsymbol{C}_{41}^{\bar{\mathrm{x}}} \end{pmatrix}^{\top} \begin{pmatrix} \mathcal{X}_{\bar{\mathrm{x}}}^{\mathrm{seq}} & Y_{\bar{\mathrm{x}}}^{\mathrm{seq}} \\ Y_{\bar{\mathrm{x}}}^{\mathrm{seq}} & Z_{\bar{\mathrm{x}}}^{\mathrm{seq}} \end{pmatrix} \begin{pmatrix} \boldsymbol{C}_{23}^{\bar{\mathrm{x}}} \\ \boldsymbol{C}_{41}^{\bar{\mathrm{x}}} \end{pmatrix} \\ + \begin{pmatrix} \boldsymbol{C}_{41}^{\mathrm{y}} \\ \boldsymbol{C}_{23}^{\mathrm{y}} \end{pmatrix}^{\top} \begin{pmatrix} X_{\mathrm{y}\bar{\mathrm{x}}}^{\mathrm{seq}} & Y_{\mathrm{y}\bar{\mathrm{x}}}^{\mathrm{seq}} \\ \overline{Y}_{\mathrm{y}\bar{\mathrm{x}}}^{\mathrm{seq}} & Z_{\mathrm{y}\bar{\mathrm{x}}}^{\mathrm{seq}} \end{pmatrix} \begin{pmatrix} \boldsymbol{C}_{23}^{\bar{\mathrm{x}}} \\ \boldsymbol{C}_{41}^{\bar{\mathrm{x}}} \end{pmatrix} \right], \end{aligned} \tag{D.19a}$$

where the $\mathcal{X}$'s are related to the X's of refs. [16, 21] by

$$X_{\mathrm{y}}^{\mathrm{seq}} = |M_{\mathrm{i}}| \Omega_{\mathrm{i}} + \mathcal{X}_{\mathrm{y}}^{\mathrm{seq}}, \tag{D.19b}$$

$$X_{\bar{\mathrm{x}}}^{\mathrm{seq}} = |M_{\mathrm{f}}^{\mathrm{seq}}| \Omega_{\mathrm{f}}^{\mathrm{seq}} + \mathcal{X}_{\bar{\mathrm{x}}}^{\mathrm{seq}}. \tag{D.19c}$$

Combined with (D.19), our previous result that soft $x_{\mathrm{Q}} \leftrightarrow x_{\bar{\mathrm{Q}}}$ is equivalent to $\boldsymbol{C}_{23} \to -\boldsymbol{C}_{23}$ means that

$$\begin{array}{ll} (X_{\mathrm{y}}, Z_{\mathrm{y}};\, X_{\bar{\mathrm{x}}}, Z_{\bar{\mathrm{x}}};\, Y_{\mathrm{y}\bar{\mathrm{x}}}, \overline{Y}_{\mathrm{y}\bar{\mathrm{x}}})^{\mathrm{seq}} & \text{are even under } x_{\mathrm{Q}} \leftrightarrow x_{\bar{\mathrm{Q}}}, \\ (Y_{\mathrm{y}};\, Y_{\bar{\mathrm{x}}};\, X_{\mathrm{y}\bar{\mathrm{x}}}, Z_{\mathrm{y}\bar{\mathrm{x}}})^{\mathrm{seq}} & \text{are } \underline{\text{odd}} \text{ under } x_{\mathrm{Q}} \leftrightarrow x_{\bar{\mathrm{Q}}} \end{array} \tag{D.20}$$

in the soft limit (D.2). These even/odd properties may be used to see the symmetry or anti-symmetry of formulas like (A.15) and (A.28d) without drilling down into the complicated detailed formulas for the $(X, Y, Z)'s$.

References

[1] L. D. Landau and I. Pomeranchuk, "Limits of applicability of the theory of bremsstrahlung electrons and pair production at high-energies," Dokl. Akad. Nauk Ser. Fiz. **92** (1953) 535.

[2] L. D. Landau and I. Pomeranchuk, "Electron cascade process at very high energies," Dokl. Akad. Nauk Ser. Fiz. **92** (1953) 735.

[3] A. B. Migdal, "Bremsstrahlung and pair production in condensed media at high-energies," Phys. Rev. **103**, 1811 (1956);

[4] L. Landau, *The Collected Papers of L.D. Landau* (Pergamon Press, New York, 1965).

[5] R. Baier, Y. L. Dokshitzer, A. H. Mueller, S. Peigne and D. Schiff, "The Landau-Pomeranchuk-Migdal effect in QED," Nucl. Phys. B **478**, 577 (1996) [arXiv:hep-ph/9604327];

[51] Our (D.19a) is not shown explicitly in refs. [16, 21] but the explicit version may be found in eq. (3.25) of ref. [26]. In the earlier paper [21] the argument, appearing in appendix E.2 of that paper, proceeded by analogy with section 5.3 of ref. [20] and skips the explicit formula. The analogous formula is eq. (5.41) of ref. [20].

[6] R. Baier, Y. L. Dokshitzer, A. H. Mueller, S. Peigne and D. Schiff, "Radiative energy loss of high-energy quarks and gluons in a finite volume quark-gluon plasma," Nucl. Phys. B **483**, 291 (1997) [arXiv:hep-ph/9607355].

[7] R. Baier, Y. L. Dokshitzer, A. H. Mueller, S. Peigne and D. Schiff, "Radiative energy loss and $p_\perp$-broadening of high energy partons in nuclei," Nucl. Phys. B **484** (1997) [arXiv:hep-ph/9608322].

[8] B. G. Zakharov, "Fully quantum treatment of the Landau-Pomeranchuk-Migdal effect in QED and QCD," JETP Lett. **63**, 952 (1996) [Pis'ma Zh. Éksp. Teor. Fiz. **63**, 906 (1996)] [arXiv:hep-ph/9607440].

[9] B. G. Zakharov, "Radiative energy loss of high-energy quarks in finite size nuclear matter and quark-gluon plasma," JETP Lett. **65**, 615 (1997) [Pis'ma Zh. Éksp. Teor. Fiz. **65**, 585 (1997)] [arXiv:hep-ph/9704255].

[10] J. P. Blaizot and Y. Mehtar-Tani, "Renormalization of the jet-quenching parameter," Nucl. Phys. A **929**, 202 (2014) [arXiv:1403.2323 [hep-ph]].

[11] E. Iancu, "The non-linear evolution of jet quenching," JHEP **10**, 95 (2014) [arXiv:1403.1996 [hep-ph]].

[12] B. Wu, "Radiative energy loss and radiative $p_\perp$-broadening of high-energy partons in QCD matter," JHEP **12**, 081 (2014) [arXiv:1408.5459 [hep-ph]].

[13] P. Arnold, O. Elgedawy and S. Iqbal, "Are gluon showers inside a quark-gluon plasma strongly coupled? a theorist's test," Phys. Rev. Lett. **131**, no.16, 162302 (2023) [arXiv:2212.08086 [hep-ph]].

[14] P. Arnold, O. Elgedawy and S. Iqbal, "The LPM effect in sequential bremsstrahlung: gluon shower development," Phys. Rev. D **108**, no.7, 074015 (2023) [arXiv:2302.10215 [hep-ph]].

[15] P. Arnold, S. Iqbal and T. Rase, "Strong- vs. weak-coupling pictures of jet quenching: a dry run using QED," JHEP **05**, 004 (2019) [arXiv:1810.06578 [hep-ph]].

[16] P. Arnold and S. Iqbal, "In-medium loop corrections and longitudinally polarized gauge bosons in high-energy showers," JHEP **12**, 120 (2018) [erratum: JHEP **12**, 098 (2023)] [arXiv:1806.08796 [hep-ph]].

[17] P. Arnold, O. Elgedawy and S. Iqbal, "Strong vs. weakly coupled in-medium showers: energy stopping in large-$N_{\rm f}$ QED," arXiv:2404.19008 [hep-ph].

[18] T. Liou, A. H. Mueller and B. Wu, "Radiative $p_\perp$-broadening of high-energy quarks and gluons in QCD matter," Nucl. Phys. A **916**, 102 (2013) [arXiv:1304.7677 [hep-ph]].

[19] P. Arnold, "Universality (beyond leading log) of soft radiative corrections to $\hat{q}$ in $\mathrm{p}_\perp$ broadening and energy loss," JHEP **03**, 134 (2022) [arXiv:2111.05348 [hep-ph]].

[20] P. Arnold and S. Iqbal, "The LPM effect in sequential bremsstrahlung," JHEP **04**, 070 (2015) [*erratum* JHEP **09**, 072 (2016)] [arXiv:1501.04964 [hep-ph]].

[21] P. Arnold, H. C. Chang and S. Iqbal, "The LPM effect in sequential bremsstrahlung 2: factorization," JHEP **09**, 078 (2016) [arXiv:1605.07624 [hep-ph]].

[22] P. Arnold, T. Gorda and S. Iqbal, "The LPM effect in sequential bremsstrahlung: incorporation of "instantaneous" interactions for QCD," JHEP **11**, 130 (2022) [arXiv:2209.03971 [hep-ph]].

[23] P. Arnold, "Multi-particle potentials from light-like Wilson lines in quark-gluon plasmas: a generalized relation of in-medium splitting rates to jet-quenching parameters $\hat{q}$," Phys. Rev. D **99**, no.5, 054017 (2019) [arXiv:1901.05475 [hep-ph]].

[24] P. Arnold, T. Gorda and S. Iqbal, "The LPM effect in sequential bremsstrahlung: nearly complete results for QCD," JHEP **11**, 053 (2020) [*erratum* JHEP **05**, 114 (2022)] [arXiv:2007.15018 [hep-ph]].

[25] P. Arnold, "Landau-Pomeranchuk-Migdal effect in sequential bremsstrahlung: From large-N QCD to N=3 via the SU(N) analog of Wigner 6-j symbols," Phys. Rev. D **100**, no.3, 034030 (2019) [arXiv:1904.04264 [hep-ph]].

[26] P. Arnold and O. Elgedawy, "The LPM effect in sequential bremsstrahlung: $1/\mathrm{N_c^2}$ corrections," JHEP **08**, 194 (2022) [arXiv:2202.04662 [hep-ph]].

[27] N. N. Nikolaev, W. Schafer and B. G. Zakharov, "Nonlinear $k_\perp$ factorization for gluon-gluon dijets produced off nuclear targets," Phys. Rev. D **72**, 114018 (2005) [hep-ph/0508310].

[28] B. G. Zakharov, "Color randomization of fast gluon-gluon pairs in the quark-gluon plasma," J. Exp. Theor. Phys. **128**, no.2, 243-258 (2019) [arXiv:1806.04723 [hep-ph]].

[29] J. H. Isaksen and K. Tywoniuk, "Wilson line correlators beyond the large-N_c," JHEP **11**, 125 (2021) [arXiv:2107.02542 [hep-ph]].

[30] J. H. Isaksen and K. Tywoniuk, "Precise description of medium-induced emissions," JHEP **09**, 049 (2023) [arXiv:2303.12119 [hep-ph]].

[31] G. 't Hooft, "A Planar Diagram Theory for Strong Interactions," Nucl. Phys. B **72**, 461 (1974)

[32] P. Arnold, H. C. Chang and S. Iqbal, "The LPM effect in sequential bremsstrahlung: 4-gluon vertices," JHEP **10**, 124 (2016) [arXiv:1608.05718 [hep-ph]].